BARC
newsletter

BEAM
TECHNOLOGIES

BEAM technologies

In pursuit of self reliance

It gives us immense gratification to bring out this special BARC Newsletter on 'Beam Technology Development and their applications'. Globally, the technologies and the applications of an electron beam, lasers, plasma, and accelerators have been incessantly growing for the benefit of mankind from industrial sector to environment. This issue of Newsletter comprises of articles based on R&D upshot, feature articles, and research synopses, which provide a glimpse of the ongoing activities in beam development and allied technologies in BARC. It also apprises the readers regarding various symposia and workshops organized in BARC to sensitize scientific community at large, and finally about the "Import Substitutes" developed in-house and transferred to industry partners in private sector for commercialization.

This issue has total eleven research articles. The first four articles eloquently elaborate the development of SLM-OPO and its use for the spectroscopic studies for Laser Isotope Separation (LIS), demonstration of the enrichment of isotopes of ytterbium through atomic route of LIS, design and developmental aspects of LIS separator and the analytical approach for the analysis of LIS process as applied to the enrichment of ^{176}Yb. It is a great privilege to mention that the feasibility of significant isotopic enrichment of ^{152}Sm, ^{176}Yb, ^{174}Yb, ^{168}Yb, and ^{176}Lu suitable for the medical and the industrial applications has been successfully demonstrated in BARC at BTDG. The indigenously enriched ^{152}Sm was recently used for the clinical trials at TMC after neutron activation and radiopharmaceutical formulation by RC&IG. The procedure for the pre-clinical and clinical trials using indigenously enriched isotopes of ^{176}Yb and ^{176}Lu is in progress. The next article coherently covers the Density Functional Theory based calculations for the determination of the vibrational isotope shift of the molecule for the molecular-based LIS process. The subsequent article describes the design aspects and progress made in the indigenous development of high power hollow cathode air plasma torch along with its applications. The development of the magnetic pulse welding technique for the joining the dissimilar metals, welding of tube plugs, PFBR fuel clad, and its end plug has been expansively described in the ensuing three articles. Furthermore, the design and successful demonstration of pulsed power systems and capacitor-driven electromagnetic rail gun to attain the desired velocity of the armature for high impact studies as well as the development of a solid-state pulse modulator for biological applications have been expounded in two dedicated articles.

The seven feature articles provide the glimpse and apprise of the advanced status of a spectrum of technologies in BARC, which include applications of e-beam and electron beam accelerators, air plasma torch for the incineration of solid waste, X-Band Linac with its industrial & medical applications, the pre-buncher cavity to enhance beam transmission in RF Linac and the microwave and X-rays. The eight research synopses in this issue provide a quick glance to the recent publications in the leading journals in a wide range of research activities. We are confident that this special issue will enrich the scientific community at large towards Self-Reliant India.
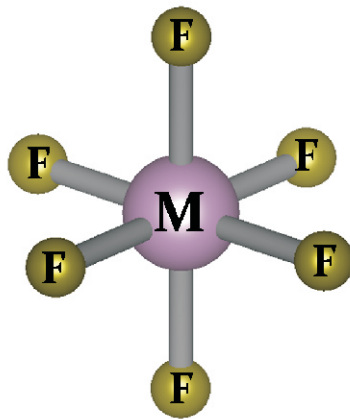
We take this opportunity to congratulate all the authors for their valuable contributions. We earnestly acknowledge the guidance of the editor, sincere and hard work of the editorial team of SIRD for the compilation of the articles, creative work in designing the cover page and for dedicated efforts in bringing out BARC Newsletter in a time bound manner.

Sanjay Sethi
and
Archana Sharma

Table of Contents

LIS Separator **20**

Structure of MF_6O_h Symmetry **27**

MPW Experimental Setup **34**

Assembly of Driving Rollers **44**

Pulse Modulator **50**

DC Accelerator **57**

RESEARCH SYNOPSES

CONNECT - PROCEEDINGS OF SYMPOSIA, WORKSHOPS AND CONFERENCES

LAB TO INDUSTRY - TRANSFER OF TECHNOLOGY

This page is intentionally left blank

RESEARCH
AND
DEVELOPMENT
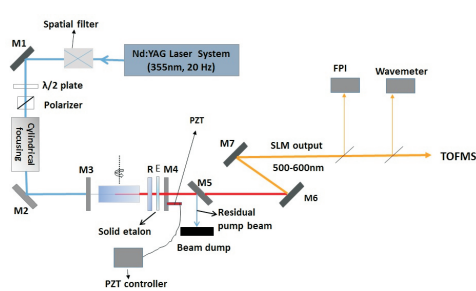
Isotope Enrichment

Development and Application of Single Longitudinal Mode Optical Parametric Oscillator for Selective Photoionization Studies on Lu-176 Isotope

C. S. Rao*, Diptimayee Biswal, Asawari D. Rath* and S. Kundu

Advanced Tunable Laser Application Facility, Beam Technology Development Group
Bhabha Atomic Research Centre, Mumbai-400085, INDIA

Schematic of the SLM OPO
experimental setup

ABSTRACT

We have designed and developed a single longitudinal mode (SLM) OPO (Optical Parametric Oscillator) pumped by the third harmonic of Nd:YAG laser operating at 20Hz repetition rate. The SLM OPO is continuously tunable over a spectral range of 500–600nm and exhibits a spectral linewidth ($\Delta\upsilon$) of ~200MHz over this entire spectral range. The developed SLM OPO has been integrated with the TOFMS (Time-of-flight Mass Spectrometer) setup and used as an alternative first step excitation source to the existing three-step selective photoionization scheme used for selective photoionization studies on Lu-176 with multi-mode dye lasers. The photoionization studies reveal that just by using the SLM OPO in place of multi-mode dye laser ($\Delta\upsilon$~2GHz) as first step excitation source, the degree of enrichment of Lu-176 is enhanced from ~85 % to better than 96 %.

KEYWORDS: *Single Longitudinal Mode (SLM),* Optical Parametric Oscillator (*OPO*), *Selective Resonant Photoionization, Enrichment of Lu-176.*

Introduction

Optical Parametric Oscillators (OPOs) are highly efficient devices for generating tunable coherent radiation in the visible to IR range[1]. They can cover the frequencies which are not directly accessible with existing conventional tunable lasers. The attractive features of these devices include high power, all-solid-state compact design, and the possibility of a very broad wavelength tuning range making them an ideal choice for use in basic and applied research as well as industrial, environmental, and healthcare applications, where laser tunability is essential.

Laser-based selective multi-step photoionization and subsequent collection of the desired isotope is a very lucrative separation technology, particularly for medical isotopes where the typical product requirement is in the range of a few milligrams to a gram. To attain high purity in the product, tunable lasers with narrow linewidths (preferably SLM) are essential, particularly in the case of isotopic systems exhibiting overlapping spectra. Further, tunable SLM lasers are desirable for selectivity studies of such isotopes and precise spectroscopic characterization of their atomic levels and transitions involved in the selective photoionization scheme. However, the commercially available SLM tunable lasers, suitable for high-resolution spectroscopy, are too expensive. Further, the conventional narrowband liquid dye lasers widely used for these applications are limited by their wavelength tunability. The tuning range of these dye lasers is typically 25-30nm for a given dye and thus requiring multiple dyes to cover the broad spectral range in the visible region, which is cumbersome and time-consuming. For example, using a

β-BaB$_2$O$_4$ (BBO) crystal pumped by the third harmonic of an Nd:YAG laser, the output of the singly resonant OPO is continuously tunable from 412nm to 650nm[2]. However, the inherent shortcoming of the OPO is that the nonlinear-optical phase-matching conditions naturally cause relatively broad spectral linewidth.

Recently, we have developed a new design of narrowband OPO and demonstrated narrowband operation down to SLM by employing cylindrical focusing to the pump and intra-cavity pump beam reflector along with an etalon[3]. Here we present our work wherein this cavity design was improved and incorporated with minor modifications to develop an automated SLM OPO module with wavelength and cavity length controls for wavelength tuning and frequency stabilization. The developed SLM OPO module was combined with the existing laser set up and used in proposed three-step selective photoionization ladder for the enrichment of Lu-176 from its natural composition (Lu-175: 97.41% and Lu-176: 2.59%). The three-step photoionization schemes[4,5] can provide high selectivity and degree of enrichment of ~85% with multimode dye lasers ($\Delta\upsilon$ ~2GHz) at high intensities requisite for high ionization. As a next step, the SLM OPO output was used in place of the multimode dye laser tuned to the first step excitation wavelength and studied the performance by evaluating the enhancement in selectivity and degree of enrichment of Lu-176 isotope.

The SLM OPO Design

The optical configuration of the SLM OPO is shown schematically in Fig.1(a) while Fig.1(b) shows a pictorial view of the experimental setup. The SLM OPO consists of a type-II phase matched BBO crystal with dimensions 6 × 12 × 15mm³ (cut: $\theta = 37^0$, $\varphi = 30^0$). The crystal is placed in a plane-plane

*Authors for Correspondence: C. S. Rao and Asawari D. Rath
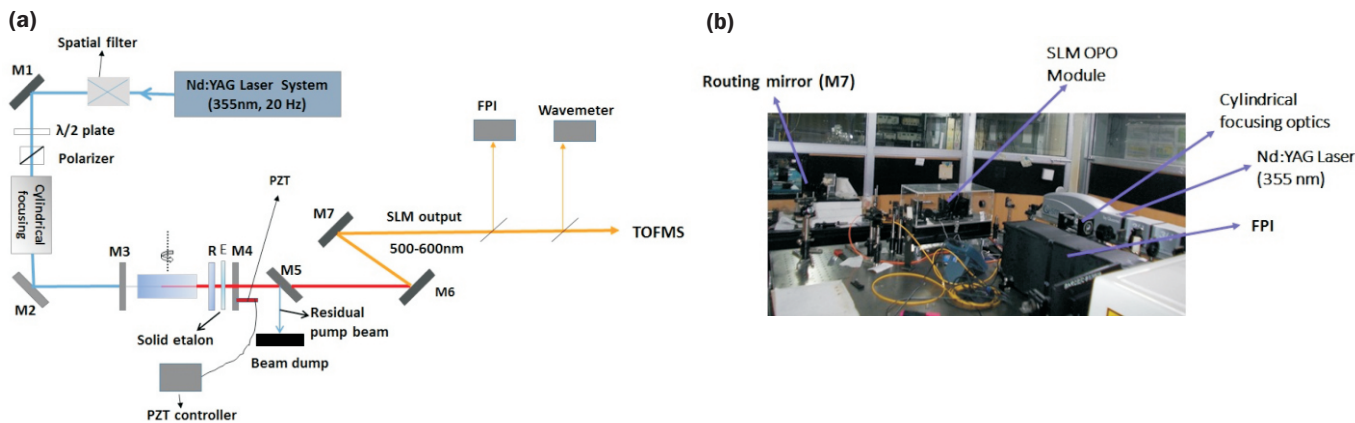*E-mail: somu@barc.gov.in and asawarim@barc.gov.in*

Fig.1: (a) Schematic of the SLM OPO experimental setup
(b) Pictorial view of the experimental setup in the RIMS laser facility.

cavity formed by broadband mirrors labeled as M3 and M4 with reflectivity 99% and 70%, respectively, in the spectral region 490nm to 630nm while at the pump wavelength of 355nm both the mirrors have high transmission (>95%). The BBO crystal was pumped by third harmonic of an Nd:YAG laser (355nm) which delivers a maximum output power of ~400mW with smooth temporal profile at repetition rate of 20Hz and FWHM of ~8ns. A spatial filtering technique has been employed for the pump beam, which removes the spatial intensity variations in the pump beam and generates a near Gaussian intensity profile and a variable attenuator comprising of a half-wave plate and a polarizer to control the pump laser pulse energy. In addition, a cylindrical focusing system[6,7] has been employed for the pump beam to generate an elliptical beam at the center of the type-II BBO. The cylindrical focusing increases the interaction length of the signal with the pump in the nonlinear crystal and reduces the threshold pump pulse energy required for the OPO.

An intra-cavity pump beam reflector, R, whose reflectivity is ~99% at 355nm (high transmission for signal and idler wavelengths) was placed after the BBO crystal, to double pass the pump beam through the BBO crystal. In type-II phase matched OPOs, the spectral linewidth of the resonant signal wave is predominantly due to the divergence bandwidth of the signal wave (divergence bandwidth much greater than the inherent gain bandwidth) because of the asymmetric wavelength change with the noncollinear angle in Type-II phase matching. However, the double-pass configuration of the pump beam helps in reducing the divergence broadening in which, only the collinear rays of the signal propagating in the direction of the pump wave experience gain at the same wavelengths for both forward and backward pass through the nonlinear crystal. The noncollinear rays experience the gain at different wavelengths in the forward and backward passes because of the asymmetric wavelength change with noncollinear angle, leading to a decrease in effective gain[8]. The double passing has facilitated spectral narrowing[3] by reducing the divergence broadening. As a result, the spectral linewidth has been reduced from 500GHz to ~ 90GHz and also has lowered the oscillation threshold from 2mJ/pulse to 1mJ/pulse. To reduce the spectral linewidth further and to achieve SLM operation of the OPO, a solid Fabry Perot (FP) etalon whose FSR is 79GHz, Finesse 22 was chosen to place inside the OPO cavity after the pump beam reflector, shown as 'E' in Fig.1(a). Furthermore, to provide a better longitudinal mode discrimination for stable SLM operation of the OPO, the length of the cavity has been restricted to well within 4.5cm, corresponding to an optical length of 6cm. Both the crystal and

etalon were mounted on computer-controlled stepper motorized stages with an angular resolution of 1μrad. The coarse wavelength tuning of the SLM OPO is achieved through the rotation of the crystal. The angular rotation of the etalon provides the fine adjustment to the etalon transmission peak for matching with the peak of the OPO cavity gain bandwidth. The output coupler (M4) was mounted on a PZT driven translation for active stabilization of the cavity. The residual pump beam was dumped by using a dichroic mirror M5. The routing mirrors M6 and M7 having high reflectivity at the OPO signal wavelengths were used to route the OPO output to the TOFMS. The SLM OPO output was sampled as shown in the Fig.1(a) for wavelength measurement and monitoring the fringe pattern to ensure the single mode operation of the OPO during the experiment. The wavelength was monitored using a high resolution wavemeter having absolute wavelength accuracy of 30MHz. A Fabry Perot etalon (FSR 7.5GHz) based Interferometer (FPI) was constructed to monitor the fringe pattern of the SLM OPO continuously during experiment. The SLM OPO output was delivered up to the TOFMS chamber of the RIMS experimental set up for selective photoionization experiments on natural lutetium.

Performance of the SLM OPO

The developed Type-II BBO based OPO is continuously tunable from 490nm to 630nm. Fig.2 shows the wavelength
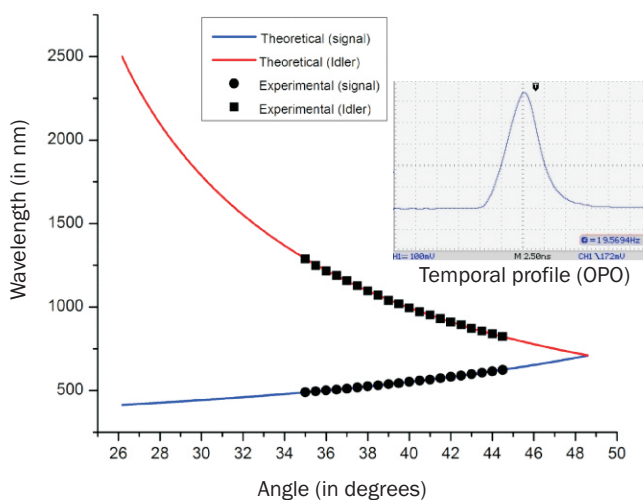

Fig.2: Wavelength tuning curve of the signal wave and the corresponding idler wave with change in internal angle to the optic axis of Type-II BBO OPO. Inset: The oscilloscope trace of the temporal profile of the OPO signal output.
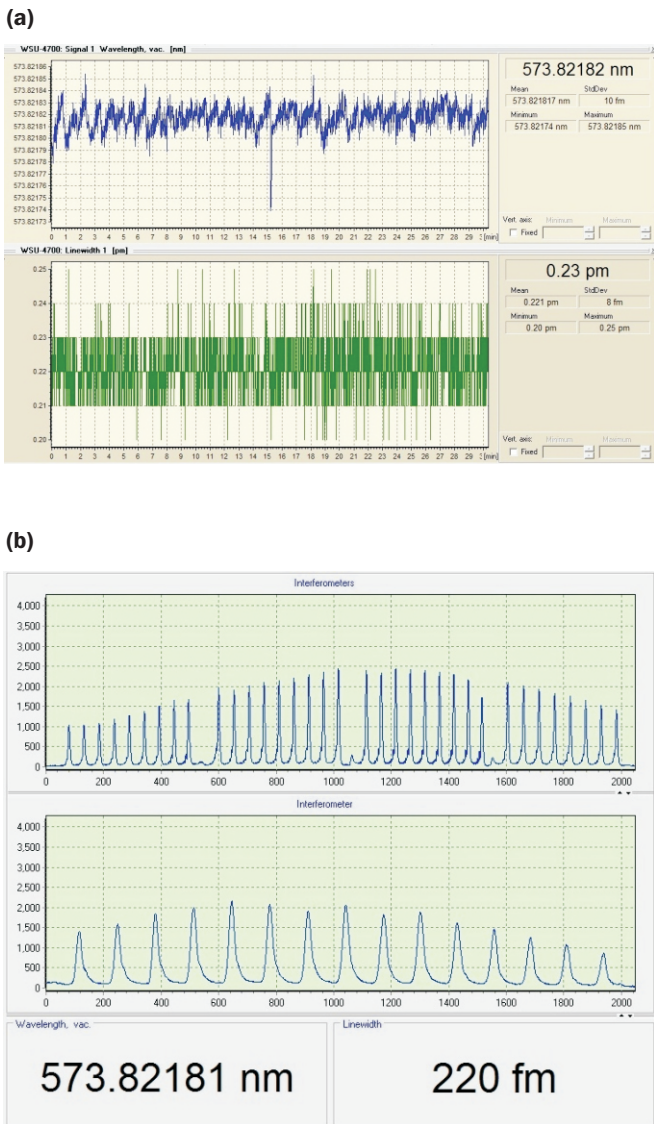
(a)

(b)

Fig.3: Spectral characteristics of SLM OPO (a) Frequency stability (b) Interferometer fringe pattern of the high resolution Wavemeter.

tuning curve of the signal wave and corresponding idler with a change in internal angle to the optic axis of Type-II BBO crystal. However, the insertion of FP solid etalon in the OPO cavity, which is coated for R~88% in the spectral region of 500-600nm, restricted the tuning range to 500-600nm. The temporal pulse width (FWHM) of the SLM OPO was measured to be ~4.5ns. The oscilloscope trace of the SLM OPO signal output is shown in the inset of Fig.2. High spectral purity of ~200MHz and high wavelength stability of the source laser are requisite for the first step excitation for achieving high selectivity and a high degree of enrichment of the Lu-176. Fig.3(a) shows the long term frequency as well as spectral linewidth stability of the SLM OPO at 573.82181nm measured over a duration of 30 min. The spectral linewidth of the SLM OPO operating at 573.82181nm was measured to be ~220fm which corresponds to ~200MHz. The standard deviation of the wavelength and spectral linewidth during the long term operation was measured to be ~±10fm and ±8fm respectively. Fig.3(b) shows the high-resolution wavemeter interferometer fringe pattern of the SLM OPO output. The SLM OPO was set to operate at a power of ~1.5mW at 20Hz repetition rate, sufficient for beam sampling for diagnostics and TOFM.

RIMS Experimental Facility

The RIMS experimental set up for multi-step multi-colour resonance ionization mass spectroscopy[4] comprises of three multi-mode dye lasers DL-1 to DL-3 pumped by second harmonic of Nd:YAG lasers and an indigenously developed Time Of Flight Mass Spectrometer (TOFMS) with mass resolution of ~200amu. The dye laser beams are combined to form a collinear beam with good spatial overlap. Time delay of few nanoseconds can be introduced between the pulses from (DL-1, DL-2) and (DL-2, DL-3), by use of optical delay line or digital delay generator to ensure their sequential arrival at the laser-atom interaction zone of the TOFMS. An atomic beam generator integrated with TOFMS delivers well collimated beam of Lu atoms in the interaction region to spatially overlap with all the three dye laser beams. The photo-ions generated are directed by use of DC electric fields to an MCP detector through the mass analyzer module of TOFMS. Mass spectra thus obtained can be recorded using a digital storage oscilloscope and/or a gated integrator based data acquisition and laser control system. Parts of the lasers are sent to a wavelength meter for wavelength determination.

Selectivity Experiments on Natural Lutetium

We have improved the three-step photoionization scheme for Lu-176 enrichment reported earlier[4] by selecting a stronger albeit broader autoionization resonance at 577nm[5] which reduces the power requirement on ionizing laser. It is depicted schematically in Fig.4, wherein solid arrows indicate the hyperfine pathway chosen for selective photoionization of Lu-176 by virtue of the high selectivity as well as maximum accessibility it offers. Consequently, the selectivity achieved by this scheme with multi-mode lasers DL-1 to DL-3 of line width ~2 GHz tuned to first, second and third step transitions is ~85% at laser powers adequate for enrichment runs.
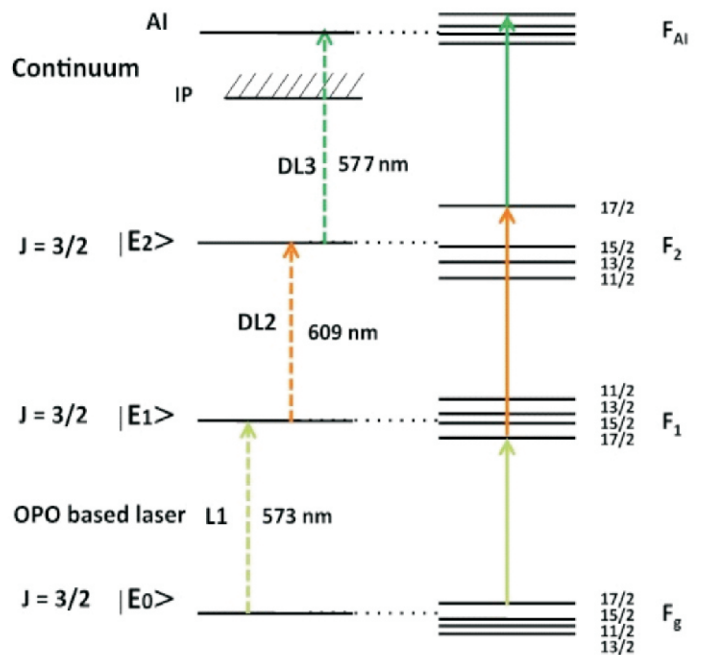

Fig.4: Schematic of three-step three-colour resonance photoionization scheme used for selective ionization of Lu-176. The dotted arrows show the three-step scheme while solid arrows indicate the hyperfine pathway used offering high selectivity and high accessibility.

Effect of SLM OPO on the Isotopic Selectivity of Lu-176

To evaluate the effect of narrow line width on selectivity, the multi-mode laser beam from DL-1 providing first step excitation was replaced by the SLM OPO output beam of comparable power. The SLM OPO was precisely tuned to the $F_g = 17/2 \rightarrow F_1 = 17/2$ hyperfine component of the first step transition of Lu-176 at 573nm exciting its population in lower hyperfine level to upper hyperfine level with F = 17/2. The multimode lasers DL-2 and DL-3 were tuned as before to the second and third step transition wavelengths of Lu-176 at 609nm and 577nm respectively so as to follow the ionization pathway $F_g = 17/2 \rightarrow F_1 = 17/2 \rightarrow F_2 = (17/2) \rightarrow F_{AI}$. The replacement of multi-mode laser beam from DL-1 by SLM OPO laser beam resulted in remarkable enhancement in the selectivity.

Fig.5 shows mass spectra of Lu isotopes recorded using TOFMS where multi-mode laser from DL-1 (spectrum in black colour) and SLM OPO (spectrum in blue colour) was used for first step excitation. The powers of both DL-1 and OPO were adjusted to 0.1mW measured over cross-sectional area of diameter 3mm. Corresponding powers of DL-2 and DL-3 were 0.3mW and 1.5mW, respectively. These values are comparable to powers intended for use in enrichment experiments. With first step excitation by multi-mode laser, degree of enrichment of ~85% was achieved for Lu-176 from its natural abundance of 2.6%. This corresponds to a separation factor of ~213. With SLM OPO beam of identical intensity, the degree of enrichment increased to >96 %, thus,
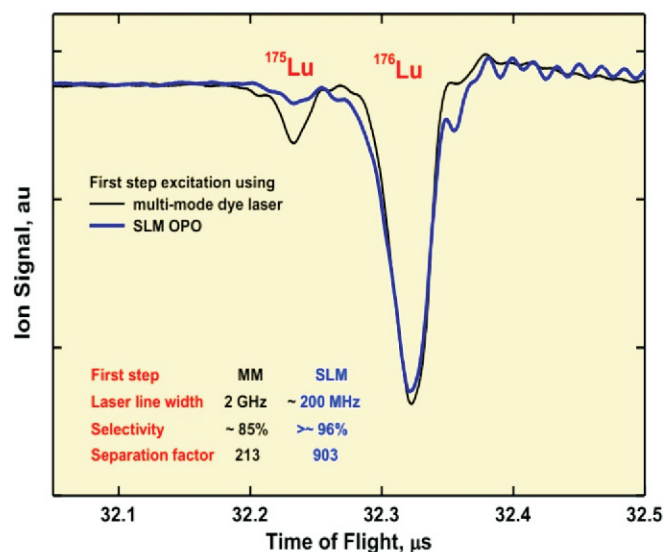
increasing the separation factor to >903. It may be noted that in enrichment experiments, along with first step, when second excitation transition is also provided by SLM lasers, the spectroscopic selectivity at these laser powers is expected to enhance to >99%.

Conclusion and Future Scope

In conclusion, we have developed a single longitudinal mode OPO, which is tunable in the spectral region of 500-600nm. The SLM OPO has been set up in the RIMS laser facility for utilization as a first step excitation source alternative to the existing multimode laser for the selective photoionization studies of Lu-176. The spectral characteristics of the SLM OPO have been studied, and it is found that the time averaged spectral linewidth of the OPO is less than 200MHz in the spectral region of 500-600nm. Employing the SLM OPO as the first step excitation source resulted in substantial enhancement (from 85% to 96%) in the degree of enrichment of Lu-176. Furthermore, considering the fact that the second step selectivity of our photoionization scheme is higher than the first step, these results signify >99% spectroscopic selectivity when single-mode lasers are employed for both the first and second step selective excitation of Lu-176 in the enrichment experiments.

Acknowledgements

References

[1] L. K. Cheng, W. R. Bosenberg, C. L. Tang, Broadly tunable optical parametric oscillation in β-BaB$_2$O$_4$, Appl. Phys. Lett., 1988, **53**, 175.

[2] R. C. Bapna, C. S. Rao, K. Dasgupta, Low-threshold operation of a 355-nm pumped nanosecond β-BaB$_2$O$_4$ optical parametric oscillator, Opt. Laser Technol., 2008, **40**, 832.

[3] C. S. Rao, S. Kundu, A. K. Ray, SLM operation of a high repetition rate BBO Optical Parametric Oscillator pumped by DPSSL at 355nm, Opt. Laser Technol., 2021, **138**, 106878.

[4] Asawari D. Rath, S. Kundu, Novel Highly Selective Photoionization Scheme for Enrichment of Lu-176, BARC Newsletter, 2020, **373**, 1-5.

[5] Asawari D. Rath, Diptimayee Biswal and S. Kundu, Odd Parity Autoionization Levels of Lu I by Three-step Photoionization, J. Quant. Spectrosc. Radiat. Transf., 2021, **270**, 107696.

[6] D. W. Coutts, J. A. Piper, One watt average power by second harmonic and sum frequency generation from a single medium scale copper vapor laser,. IEEE J. Quantum Electron., 1992, **28**, 1761.

[7] C. S. Rao, S. Kundu, A. K. Ray, High repetition rate nanosecond optical parametric oscillator pumped by the third harmonic of a DPSSL, Appl. Phys. B, 2018, **124**, 163.

[8] G. Anstett, G. Göritz, D. Kabs, R. Urschel, R. Wallenstein, A. Borsutzky, Reduction of the spectral width and beam divergence of a BBO-OPO by using collinear type-II phase matching and back reflection of the pump beam, Appl. Phys. B, 2001, **72**, 583.

Fig.5: Mass spectrum of Lu isotopes recorded in TOFMS with L1, L2 and L3 tuned to the photoionization pathway $F_g = 17/2 \rightarrow F_1 = 17/2 \rightarrow F_2 (17/2) \rightarrow F_{AI}$ corresponding to 573nm, 609nm and 577nm transitions, respectively of ^{176}Lu. The black and blue mass spectra are recorded with first step excitation from multi-mode dye laser ($\Delta u \sim 2$ GHz) and SLM OPO laser ($\Delta u \sim 200MHz$), respectively while L2 and L3 are multi-mode ($\Delta u \sim 2GHz$). Comparison of the two spectra shows clear enhancement in selectivity of ^{176}Lu to ~96% when SLM OPO laser is used.

Medical Isotopes

Laser based Isotope Selective Photoionization for Enrichment of ^{176}Yb, ^{174}Yb and ^{168}Yb

Asawari D. Rath*, A. K. Singh, A. Khattar, A. Wahid, Diptimayee Biswal, A. U. Seema, Ayentika Sen, J. S. B. Singh, S. K. Maurya, J. Thomas, T. Garg, S. Baruah, B. Jana, Dev Ranjan Das, Anupama Prabhala, G. K. Sahu, B. Dikshit, Sanjay Sethi and S. Kundu*

Advanced Tunable Laser Application Facility, Beam Technology Development Group,
Bhabha Atomic Research Centre, Mumbai-400085, INDIA

Process dye lasers deployed in Yb enrichment experiment

ABSTRACT

Laser based isotope selective ionization is a suitable technique for selective isotope enrichment via atomic route. It has several advantages over conventional techniques such as high single stage selectivity, high energy efficiency and most importantly, its suitability to enrich any specific isotope, including middle isotopes of the element consisting of several isotopes. Of late, focus has been on enrichment of medical isotopes for radiopharmaceutical industry using the available expertise and infrastructure. This article presents in detail the developmental steps in establishing the enrichment process towards realization of >95% enriched ^{176}Yb from its natural abundance of ~13%. Moreover, the process was successfully employed for enrichment of other Yb isotopes of medical importance, namely, ^{174}Yb & ^{168}Yb to realize >98% enriched ^{174}Yb and ~15% enriched ^{168}Yb from their natural abundances of ~ 32% and 0.13%, respectively.

KEYWORDS: *Laser based Isotope Selective Ionization, Ytterbium, Enrichment, ^{177}Lu.*

Introduction

In recent years, there has been a growing demand of the medical isotope Lutetium-177 in radiopharmaceutical industry. Although not available in nature, ^{177}Lu can be produced by neutron irradiation of precursor isotopes ^{176}Lu (direct route) or ^{176}Yb (indirect route) in isotopically pure form[1]. This necessitates enrichment of the precursor isotope. Both direct and indirect routes have their own advantages and disadvantages. The ATLA Facility of Beam Technology Development Group has focused on both these approaches. This article describes the recent developments in the RIS facility at Engineering Hall-6 on enrichment of Yb isotopes.

Laser based isotope selective excitation followed by ionization and collection using electro-magnetic fields offers one of the most efficient techniques for isotope enrichment/ denaturing[2,3]. The complete process of enrichment requires inputs and expertise from diverse fields of science and technology and in that sense, it is truly multi-disciplinary. Availability of an efficient photoionization (PI) scheme, high power high repletion rate tunable lasers fulfilling the requirements of wavelength, line widths and intensities solicited by the PI scheme, highly collimated low loss atomic beam generation, efficient collection of the photoions as enriched product and well developed post-process treatment for product extraction are the key factors in a successful laser based enrichment process. Further, various aspects in laser-atom interaction affecting selectivity and accessibility of the process, in ion extraction e.g. plasma effects, sputtering of the already deposited product layers by ions and in non-selective pick-up processes deteriorating the selectivity need attention.

*Authors for Correspondence: Asawari D. Rath and S. Kundu
E-mail: asawarim@barc.gov.in and skundu@barc.gov.in

Isotope Selective Three-step Photoionization Scheme for Ytterbium

At the heart of laser based isotope enrichment lies a proficient multi-step isotope selective photoionization scheme giving optimum selectivity and product yield. Yb has two valence electrons and very few transitions originating from its ground level. Its ionization potential is 6.254eV. This necessitates selection of three-step photoionization scheme for selective photoionization of its isotopes using the availble laser infra-structure supporting visible range of spectrum. Yb has only one transition at 555nm starting from its ground level in visible range. A selective photoionization scheme as depicted in Fig.1 with 555nm as first step is available in literature[4] and has been used in other works on enrichment of Yb isotopes. As is evident from Fig.1, the isotopes shifts of even isotopes are ~500MHz/amu in first step transition and ~1.3GHz/amu for second step transition. However, there are two odd isotopes exhibiting hyperfine structure, with their components spanning over the spectral lines of the even isotopes. Consequently, to achieve requisite selectivity of > 95 %, very narrow line width lasers are indispensable for first and second step excitations. The ionizing transition at 582nm has broad profile and use of multimode laser for the third step is acceptable.

Development of Single Longitudinal Mode Process Dye Lasers

Dye lasers offer best suitable choice for enrichment process as they suffice to all the requirements of process like wavelength tunability, high power generation (up to tens of W) at high repetition rates (12.5KHz), *etc*. We had already developed process dye lasers pumped by Copper Vapour Laser (CLV) MOPA chains and Diode Pumped Solid State Green Lasers (DPSSGLs) with ~3GHz line width in multi-mode
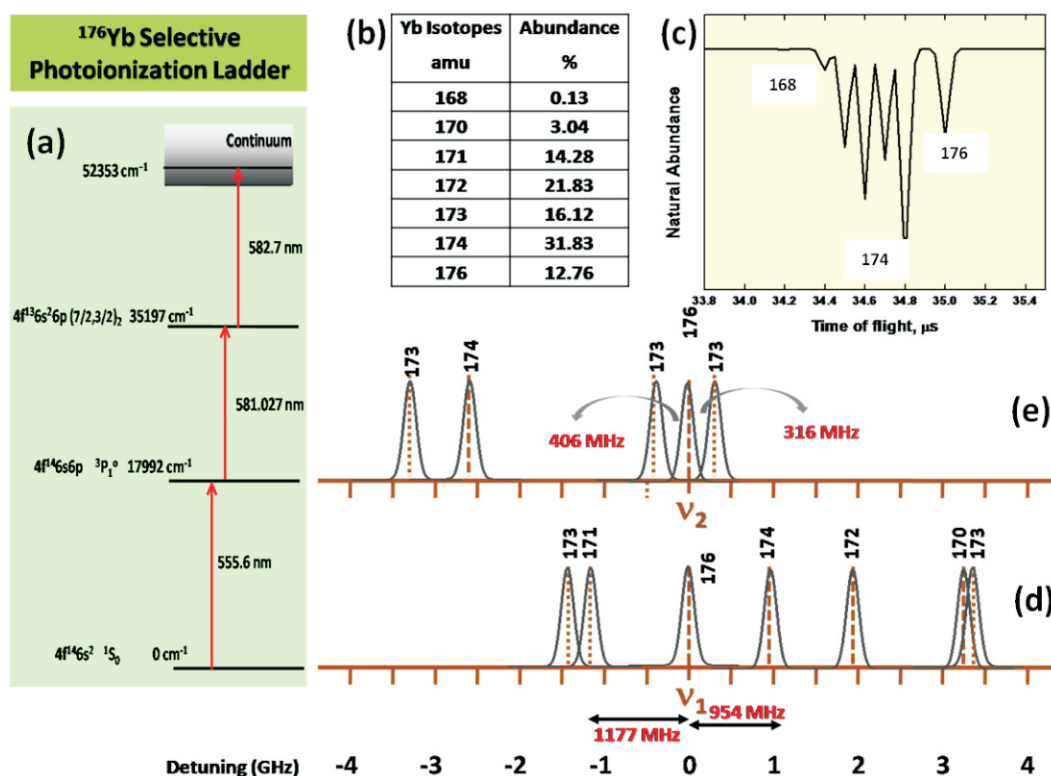
Fig.1: Three-step photoionization scheme used for selective photoionization of Yb isotopes is shown schematically in (a) with Yb energy levels and corresponding electronic configurations, (b) Presents natural composition of Yb isotopes, (c) Shows mass spectrum of Yb in natural composition when multi-mode lasers were used while (d) and (e) Depict the spectral regions in the vicinity of first and second step transitions respectively of ^{176}Yb spectral lines where the closeby spectral lines of other Yb isotopes that have maximum effect on selectivity are clearly evident.
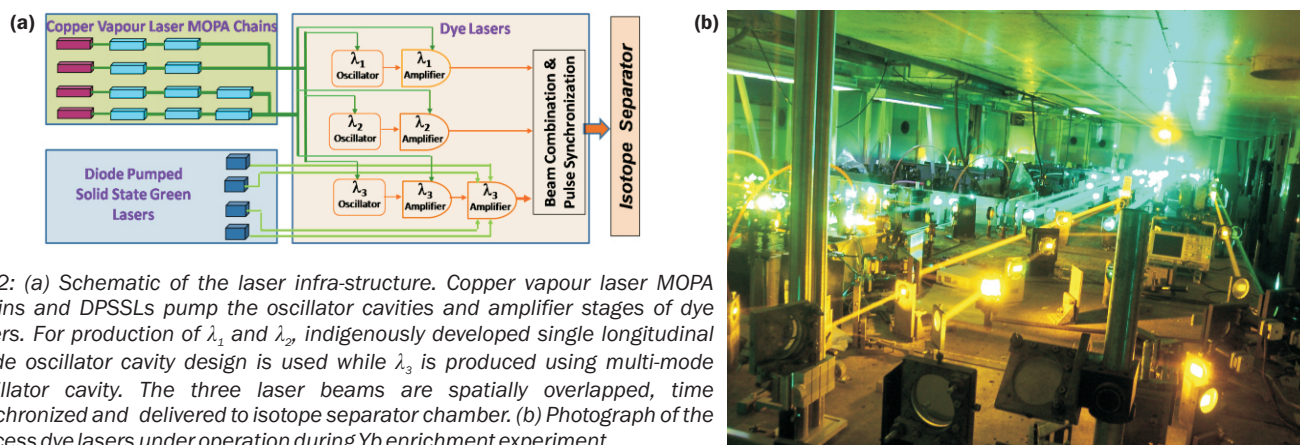

Fig.2: (a) Schematic of the laser infra-structure. Copper vapour laser MOPA chains and DPSSLs pump the oscillator cavities and amplifier stages of dye lasers. For production of λ_1 and λ_2, indigenously developed single longitudinal mode oscillator cavity design is used while λ_3 is produced using multi-mode oscillator cavity. The three laser beams are spatially overlapped, time synchronized and delivered to isotope separator chamber. (b) Photograph of the process dye lasers under operation during Yb enrichment experiment.

operation. Schematic of the laser infra-structure is presented in Fig.2 (a) and a photograph shows the dye lasers and beam combination set-up in Fig.2 (b). As a next step, we indigenously developed single longitudinal mode (SLM) dye oscillator cavity generating laser output with line width ~60MHz, time averaged line width ~100MHz and excellent stability over couple of hours[5]. A recording of wavelength and line width stability of the SLM laser over a period of 4 hours is shown in Fig.3 when laser was tuned to 555nm. In SLM laser development, the main challenge faced was the mode hops owing to temperature fluctuations in the oscillator cavity as well as dye solution. To circumvent this, the oscillator cavity was temperature stabilized. Further, various water based binary solvents offering superior thermo-optic properties were explored for their photostability and lasing efficiency and suitable solvent was optimized for process dye laser generation. The aqueous nature of dye solution also offered better safety against fire hazard. The first and second step

lasers with average powers of 700mW and 1.5-2W, respectively, and ionizing laser with average power of ~25W were spatially overlapped to make a combined beam with the help of dichroic as well as polarization based beam combiners. The temporal delays between the pulses from the three lasers were arranged to ensure their sequential arrival in the interaction region with delay of ~ 5ns.

Qualification of Laser-Atom Interaction and Optimization of Laser and Atomic Parameters

To ensure high selectivity as well as high product yield, tuning of SLM laser wavelengths precisely to the spectral lines of desired isotope is crucial. Consequently, the transition wavelengths pertaining to first and second step of the ^{176}Yb PI scheme were precisely determined within ±30MHz for first and second step. Resonance ionization mass spectroscopic technique was employed in a time of flight mass spectrometer (TOFMS) developed in house and a protocol was established
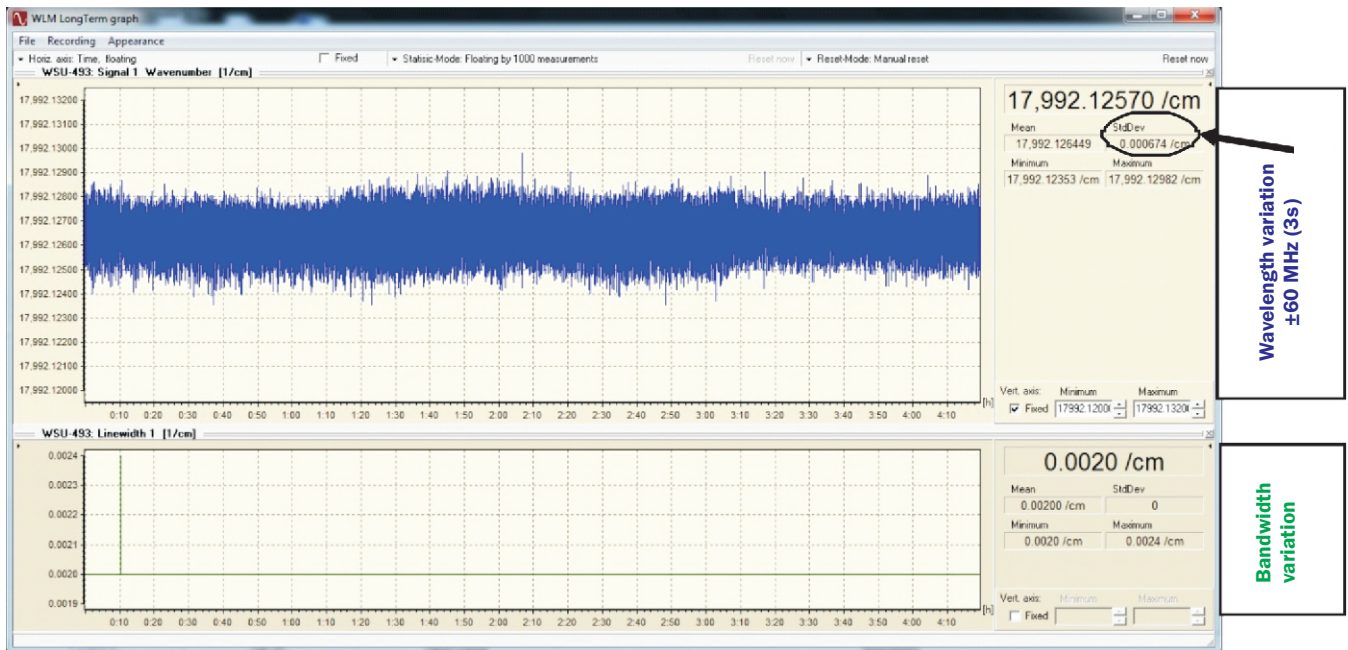
Fig.3: Wavelength of the indigenously developed SLM dye laser tuned to 555nm recorded over four hours shows highly stable output with standard deviation in wavelength of 0.000674 cm^{-1} i.e. 21MHz with fluctuations (maxima to minima) limited within ± 100MHz.
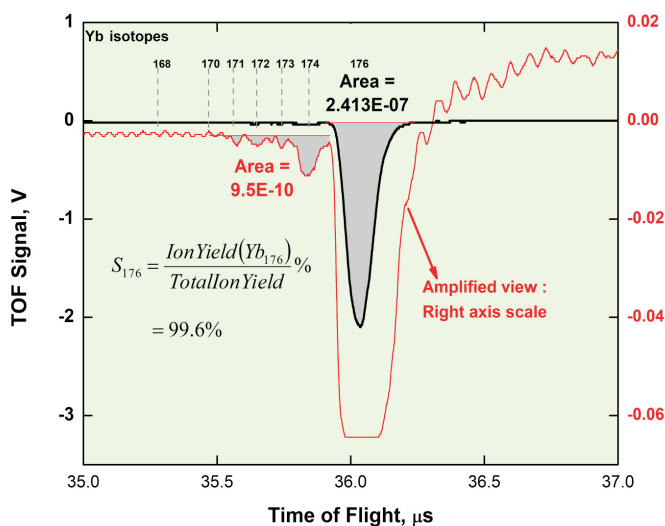

Fig.4: Mass spectrum of Yb isotopes showing selective ionization of ^{176}Yb with lasers tuned to its spectral lines at optimized intensities. For clarity amplified view of the spectrum is also plotted (in red) and the relevant scale is shown along the right axis. Further, positions of all Yb isotopes are marked with dashed vertical lines. The spectroscopic selectivity or degree of enrichment of ^{176}Yb is 99.6 %.

for precise wavelength determination pertaining to all even isotopes[6]. Further, the same set-up was used for process qualification in terms of spectroscopic selectivity. Towards this, the laser-atom interaction process in enrichment chamber was mimicked in the TOFMS and the effect on selectivity of the laser intensities was evaluated by analyzing the respective mass spectra. The intensities of the precisely tuned lasers were optimized to get maximum ion yield with spectroscopic selectivity of >99 %. The corresponding mass spectrum is presented in Fig.4. For clarity amplified view of the spectrum is also plotted (in red) and the relevant scale is shown along the right axis. Further, positions of all Yb isotopes are marked with dashed vertical lines. The optimum values of laser intensities

were used in the actual enrichment experiment, where the lasers selectively ionized ^{176}Yb atoms from a well-collimated Yb atomic beam having typical atomic number density of ~10^{11}/cc in the interaction zone of the enrichment chamber.

Experimental Chamber for Enrichment Experiments

The enrichment chamber houses all the modules necessary in enrichment process, *viz*. i) Yb atomic beam generator, ii) collimating structures for shaping the beam to minimize scattering as well as reducing the residual Doppler width in the laser propagation direction, iii) ion extraction assembly which extracts the photoions by using DC electric fields, and delivers them for deposition on the collector plate. A schematic of these modules is shown in Fig.5. The chamber is operated at 10^{-5} mbar or better vacuum.

Atomic Beam Generator

The atomic beam generator consisted of a tungsten crucible meticulously designed based on extensive thermal analysis, holding small chunks of ytterbium. The crucible was heated to 700K by radiative heat transfer from resistively heated tungsten filaments surrounding it to get atom number density of ~10^{13}/cc at source. The evaporated atoms escaped from the crucible slit through collimating structures in the form of smaller compartmentalized channels along beam axis. The channel dimensions were designed for reduction of Doppler width along both laser propagation direction and the direction of ion trajectories during collection to reduce nonselective pick-up of unwanted isotopes. The resulting atomic beam had reduced Doppler width of ~350MHz.

Multi-pass Arrangement of Lasers to Enhance Atom Accessibility

The three lasers tuned to ^{176}Yb transitions having good spatial overlap and optimum temporal synchronization were passed through the ionization region of the enrichment chamber. The combined beam with cross-sectional area of 12mm x 10mm intersected the atomic beam multiple times using a specially designed multi-pass mirror assembly to extend the interaction region along the direction of atomic
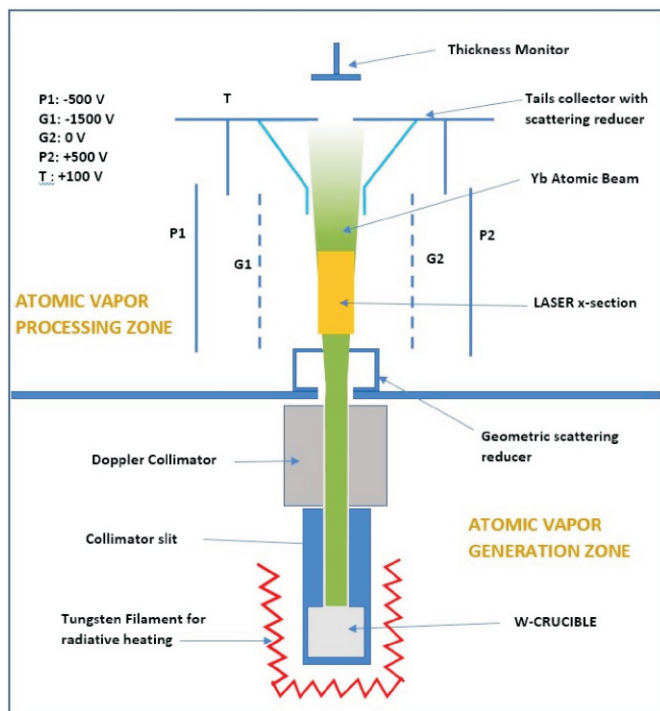
Fig.5: Schematic of the modules of experimental chamber necessary in enrichment process where vapour generation zone, Doppler width reducer zone and ion generation (laser-atoms interaction zone) and collection zone are marked appropriately. Typical voltages applied to ion collector (P1, G1)) /repeller (P2, G2) grids and plates are also shown.

Fig.6: A photograph showing deposition of photoions on the collector plate.

Fig.7: Graphical representation of the isotopic composition in the feed (right) and product (left).

beam resulting in total ionization volume of dimensions of 120mm x 12mm x 45mm. The multi-pass arrangement ensured that at least 90% of the atoms in the beam were irradiated by the lasers at least once, thus reducing sample loss and increasing collection rate.

Ion Extraction and Collection Assembly

The photoions generated in the process were directed towards collector plate by use of DC electric field. The ion collection assembly as schematically represented in Fig.5 consists of repeller plate, repeller grid, collector grid and collector plate as shown. This design facilitated significant reduction in self-sputtering of product ions as well as non-selective deposition of neutrals due to geometrical scattering from the primary as well as secondary sources. The DC extraction field was set in the range 200-400V/cm in the ionization region located between the collection and repeller grids to minimize the plasma effects. The collection plate was kept at ~500-850V generating a repelling effect on the ions and decelerating them, thus enabling their soft landing on the collector plate, consequently minimizing the self-sputtering[7]. The neutral atomic beam was collected on a tails collector which also had provision to measure atom flux using a quartz crystal based thickness monitor. Typical number density of the Yb atoms in the ionization region was ~10^{11} atoms/cc.

Results and Analysis

A photograph of the collector plate is shown in Fig.6 in which Yb ions deposited on the plate are clearly seen. Consequent to the enrichment experiment, the collector plates were eluted with nitric acid to remove the deposited Yb isotope. Small parts of this liquid sample were used for diagnosis to determine the quality and quantity of the product using ICPMS and TIMS techniques at ACD and EmA&ID, BARC, respectively. The isotopic composition of the product based on
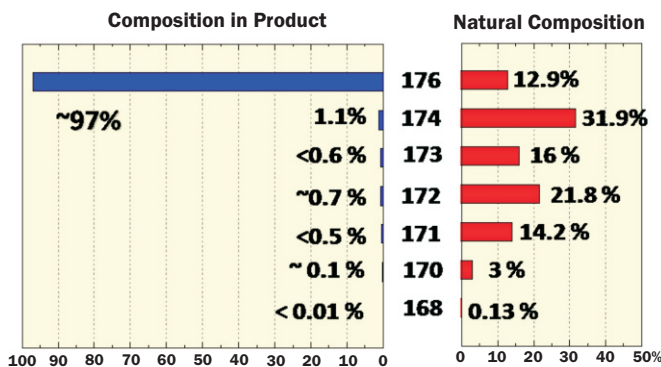
their evaluation is depicted in Fig.7 along with natural composition of Yb isotopes. After completion of analysis the product was given to RPhD for neutron irradiation in Dhruva reactor for generation of the medical isotope [177]Lu. At present, ^{177}Lu thus produced is being evaluated for clinical trials.

We have performed a series of enrichment experiments in our test set-up for [176]Yb which yielded better than 95% degree of enrichment from its natural abundance of 12.9% with 5-7mg/hour production rates, showing excellent consistency and reproducibility.

Among other isotopes of Yb, apart from [176]Yb, the isotopes [168]Yb and [174]Yb also have applications in radiopharmaceutical industry as in pure form they can be used to produce the medical isotopes [169]Yb and [175]Yb, respectively. Further, [169]Yb has industrial applications as well. The technology developed for enrichment of [176]Yb is easily extendable to these isotopes. Consequently, we have performed enrichment experiments for production of isotopically pure [168]Yb and [174]Yb as well. Towards this, same methodology developed for [176]Yb was followed to determine the transition wavelengths pertaining to selective photoionization scheme for each isotope[8,9]. Further, the selective laser-atom interaction process was qualified for spectroscopic selectivity better than 99% and the optimized laser parameters were used for actual enrichment experiments, in which 98% enriched [174]Yb and 15% enriched [168]Yb were collected successfully. Fig.8 shows photograph of the enriched product recovered in process runs for the Yb isotopes [176]Yb, [174]Yb and [168]Yb.

Before every enrichment run, the laser-atom interaction is qualified for process parameter optimization for spectroscopic selectivity of >99%. However, the actual selectivity realized in experiments is on lower side. This is credited to two factors. Firstly, the nonselective processes like neutral atom scattering from secondary sources, *etc.* deposit
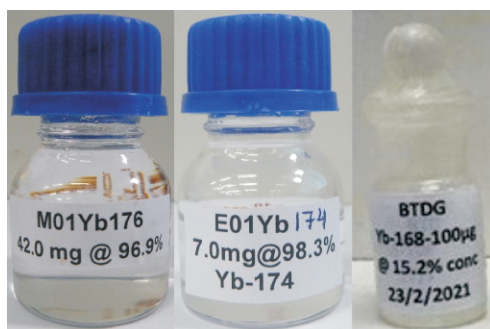
Fig.8: Sample product in liquid form recovered from enrichment experiments for Yb isotopes ^{176}Yb, ^{174}Yb and ^{168}Yb, respectively.

Yb atoms on collector plate non-selectively. Secondly, the residual Doppler broadening inside enrichment chamber (~350MHz) is much more than that during qualification experiment in TOFMS. This results in larger overlap between lasers tuned to the required isotope and spectral lines of unwanted isotopes leading to reduction in spectroscopic selectivity. The first factor is significant in enrichment of ^{168}Yb, owing to the fact that a small percentage of non-selective deposition on collector from the atomic beam is substantially large in comparison with the selectively deposited ^{168}Yb photoions, which by abundance are only 0.13% in the atomic beam. The second factor is more important in enrichment of ^{176}Yb as the separations between spectral lines of ^{176}Yb and those of odd Yb isotopes are very small, particularly, in second step. Consequently, the degree of enrichment realized in collection of ^{168}Yb is much smaller as compared to the other two isotopes, albeit it is at par with the enriched ^{168}Yb product requirement in medical and industrial sector.

Conclusion

In summary, ATLA Facility has extended the existing capabilities of laser based isotope selective resonance ionization technology to include medical isotopes, ^{176}Yb, ^{168}Yb and ^{174}Yb. Enrichment of Yb isotopes is particularly challenging owing to the overlapping nature of the spectral lines of naturally existing isotopes. It necessitates use of narrow line width lasers to achieve requisite selectivity. To cater to this, we have successfully developed single longitudinal mode process dye lasers indigenously with high average powers and high repetition rates and pumped by CVLs and/or DPSSLs. A protocol is established for precise determination of isotope specific transition wavelengths and qualification of the selective ionization process in terms of laser intensities. Well collimated atomic beam of Yb atoms is generated with residual Doppler width of ~350MHz in the interaction region. The photoions resulting from selective ionization are collected by use of soft landing technique to avoid self-sputtering. We have realized >95% enrichment in ^{176}Yb with 5-7mg/hr production rate with high reproducibility. Further, same process is employed for enrichment of ^{174}Yb and ^{168}Yb to realize >98% enriched ^{174}Yb and 15% enriched ^{168}Yb. At present, ^{177}Lu produced by neutron irradiation of the enriched ^{176}Yb from our facility is being evaluated in clinical trials.

References

[1] A. Dash, M. Raghavan, A. Pillai and F. F. Knapp Jr., Production of (177)Lu for Targeted Radionuclide Therapy: Available Options, Nucl Med Mol Imaging, 2015, **49**, 85.

[2] V. S. Letokhov, "Laser isotope separation", Nature, 1979, 277, 5698, 605.

[3] P. A. Bokhan, V. V. Buchanov, N. V. Fateev, M. M. Kalugin, M. A. Kazaryan, A. M. Prokhorov, D. E. Zakrevsky, Laser Isotope Separation in Atomic Vapor Wiley-VCH, Berlin, 2006, ISBN 3-527-40621-2.

[4] B. B. Krynetskii, V. A. Mishin, and A. M. Prokhorov, Effective scheme of photoionization of ytterbium atoms for laser separation of isotopes, Zhurnal Prikladnoi Spektroskopii, 1991 **54**, 558.

[5] A. K. Singh A. Khattar, A. Wahid, J. S. B. Singh, S. K. Maurya, P. R. Mohite, J. S. Dhumal, and S. Kundu, Development of high average power, high pulsed repetition rate single longitudinal mode dye lasers for selective photo-excitation of Yb isotopes of medical use, Proceedings of the 29th DAE_BRNS National Laser Symposium NLS-29, 2021, 12-15.

[6] D. Biswal, A. U. Seema, R. C. Das, D. R. Rathod, A. K. Singh, A. Khattar, J. S. B. Singh, A. Wahid, P. R. Mohite, S. K. Maurya, J. S. Dhumal, J. Thomas, Asawari D. Rath, S. Kundu, Precise Determination of laser wavelengths pertaining to three-step selective photoionization for enrichment of ^{176}Yb and qualification of product selectivity, Proceedings of the 29th DAE_BRNS National Laser Symposium NLS-29, 2021, 437-440.

[7] B. Dikshit and A. Sharma, Design and Analytical Evaluation of a New Ion Collection Geometry for Improvement in Quantity and Quality of Product During Laser Isotope Separation, IEEE Transactions on Nuclear Science, 2020, **67**, 2465-2473, doi: 10.1109/TNS.2020.3038066.

[8] Diptimayee Biswal, A. U. Seema, R. C. Das, D. R. Rathod, A. K. Singh, A. Khattar, J. S. B. Singh, A. Wahid, P. R. Mohite, S. K. Maurya, J. S. Dhumal, J. Thomas, Asawari. D. Rath, S. Kundu, Three-step three-colour selective photoionisation of natural ytterbium for enrichment of ^{168}Yb, Proceedings of the 30th DAE-BRNS National Laser Symposium, CP-09-20, 2022, 79-80.

[9] A. U. Seema, Diptimayee Biswal, R. C. Das, D. R. Rathod, A. K. Singh, A. Khattar, J. S. B. Singh, A. Wahid, P. R. Mohite, S. K. Maurya, J. S. Dhumal, J. Thomas, Asawari. D. Rath, S. Kundu, Three colour isotope selective photoionisation of ytterbium for ^{174}Yb enrichment, Proceedings of the 30th DAE-BRNS National Laser Symposium, CP-09-25, 2022, 81.

Laser Isotope Separation

Design and Development of Separator for Laser Isotope Separation of Lanthanides for Medical Applications

S. P. Dey*, K. Karmakar, Dileep Kumar V, Tarang Garg and Sanjay Sethi

Advanced Tunable Laser Application Facility, Beam Technology Development Group
Bhabha Atomic Research Centre, Mumbai-400085, INDIA

Separator for LIS

ABSTRACT

Beam Technology Development Group is involved in Laser Isotope Separation of lutetium, ytterbium and samarium isotopes of interest for medical applications. The technology is complex and requires integration of information and knowledge from various engineering disciplines, plasma and laser physics, atomic spectroscopy, chemistry and material science. The authors present here the philosophy and major considerations in the development of the separator chamber and its various subsystems.

KEYWORDS: *Laser Isotope Separation (LIS), Separator Design, Photo-ion Extraction, Multipass Optics.*

Introduction

Laser Isotope Separation (LIS) is one of the most promising but technically challenging isotope separation methodology conceived so far in the world. In LIS, precisely tuned lasers are used to selectively ionize a particular isotope of the feed material in atomic vapour form. The photo-ions are collected as product applying electric field (Fig.1). The LIS method becomes much more efficient than centrifuge when the isotope lies at the middle of the mass spectrum and a high enrichment is required. Additionally centrifuge requires feed as gaseous compound at room temperature. Hence, LIS is an attractive choice for producing Lu-176, Yb-176, and Sm-152 etc. with high isotopic concentration for medical applications.

The high vacuum process system consisting of the vacuum chamber and all its internal systems is commonly called the separator. High vacuum becomes a primary requirement for the process as the background pressure affects the formation of atomic beam, particle collisions and undesired neutral atom collection, charge exchange and ion collection, ultimately diluting the product concentration which is the major advantage of this process. Apart from the vacuum system, the other subsystems are atomic vapour generator, laser multipass optics, ion extraction system, gauges and monitoring instruments. The authors present some of the major aspects involved in the development of the separator system in the following sections.

Sizing and layout

The primary requirement for sizing is that the atomic source along with the ion extraction system should fit inside and are accessible. The chamber should be able to accommodate a vapour source of 400mm length and corresponding 450mm long photo-ion collector plates. Beyond this there are linear guide mounted laser beam apertures,

thermal shields for protection of optics and space for connecting thermocouples. Along the height, the source to tails collector is approximately 400mm. Away from this; there is also a quartz crystal thickness monitor for online vapour flux measurement and space for electrical feedthrough.

The commonly used cross-section for pressure vessels is circular. However, the LIS system is slightly different. The aspect ratio of the processing zone is skewed as the requirement in the height and length direction is much more than the width. With this shape a circular section remains partly unused and increases the volume which leads to more load on the vacuum system. A cuboid system with an internal dimension of 600mm×550mm×750mm and double pivot fully openable doors at the front/back, providing clear access to the internals, is selected as preferred shape. The chamber is water
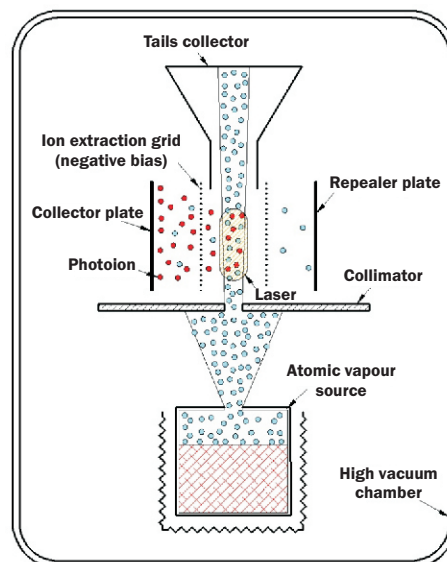

Fig.1: Schematic layout of LIS system.

*Author for Correspondence: S. P. Dey
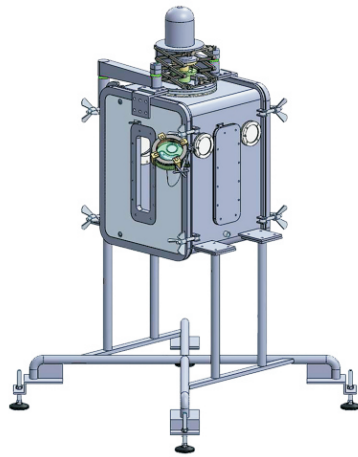*E-mail: spdey@barc.gov.in*

Fig.2: Geometric model of the separator.

Fig.3: Stress plot of the chamber at severest load case condition.

cooled with cooling water jacket over the whole surface and has an internal volume of ~350L. There are eleven ports of DN-63 to DN-250 size and seven oblong ports catering to the vacuum system, gauges, monitoring instruments, electrical feedthroughs, optics and non-orthogonal viewing Fig.2 shows the schematic geometric model of the separator. The optics-ports are further connected to an optics-chamber which is detailed later. The overall chamber is made modular and the length of the chamber can be increased by addition of more modules.

Structural Design

A primary difference between the chambers with circular and rectangular cross-sections is the stress pattern. The rectangular geometry is guided by bending stress whereas the circular ones by membrane stress leading to lower material thickness and weight. However, for the rectangular sections as in current case, the specific advantages outweigh the increase in weight. From the requirement of weldable non-magnetic material, stainless steel AISI-304L is selected as structural material. In the present separator the 6mm thick inner shell is reinforced with welded square bars of 12mm×12mm cross-section. The jacket is 8mm thick. The design is carried out for the severest load case conditions comprising of the vacuum inside i.e. near zero absolute pressure, 4 bar gauge pressure of water inside jacket and 1.5 bar gauge pressure inside chamber for testing Fig.3 depicts the stress plot of the chamber.

The reinforcements on the shell are also used as the water flow path for cooling the chamber. The reinforcement size and spacing has been optimized from structural and heat transfer coefficient considerations. The flanges of the chamber are integrated type without any neck/nozzle. Apart from making the overall chamber size very compact, these flanges also provide stiffening to the shell and jacket. Although the ASME boiler and pressure vessel code, Section VIII, Div-I, Appendix-13 provides guidelines for design of noncircular sections, the present design is carried out primarily by first principle calculations and FEM analysis.

Thermal hydraulic analysis

The thermal hydraulic design is carried out to optimize the pressure drop in the flow system and the flow velocity hence heat transfer. The present design with nominal flow channel dimensions of 26mm×12mm can cater to uniform heat flux equivalent to ~20kW. The cooling water temperature rise is limited to ~18°C at 16lpm flow. Fig-4 shows the design curve for the shell of the chamber.

Fabrication

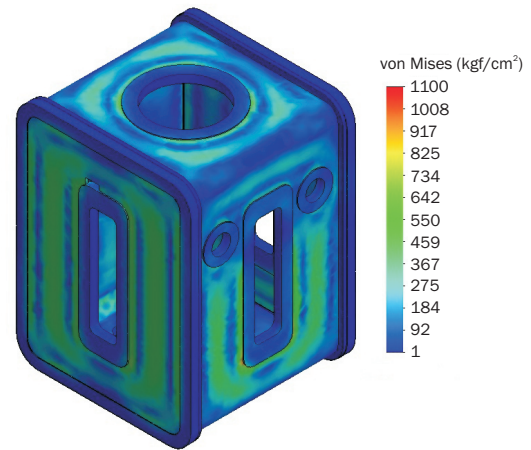All over the world there are many codes for design and

fabrication of process vessels. Few notables among them are, AD. Merkblatter (Germany), BS 5500 (United Kingdom), EN-13445 (France), IS 2825 (India) and ASME Boiler and Pressure Vessels Code (USA). Among them the ASME Boiler and Pressure Vessels Code is more popular due to its wide applicability and detailed QA guidelines. The fabrication of the present separator is as per the guidelines of ASME Section VIII Div-I, Section V and Section IX.

The overall flow of the fabrication was guided by the detailed QA plan. The flanges, plates and openings on the shell and jacket were made by water-jet cutting instead of conventional machining. Stainless steel being a poor thermal conductor, distortion of the welded section is inevitable even with proper stiffening and support. Stress relieving before removal of supports reduces the distortion. However, for most of the surfaces, keeping margin for further machining helped to maintain the dimensional requirements Fig.5 shows the integration of the water flow channels on the shell.

Chemical analysis of material, liquid penetrant test, ultrasonic test, radiography and hydro test were performed at various stages during fabrication. However the final acceptance was based on helium leak testing at 1×10^{-10} mbar.L/s sensitivity.

Vacuum system

The final product is used for human consumption as injectable, therefore, clean processing environment with minimum contamination is essential in LIS. A DN250 TMP with 1900lps nominal pumping capacity is used in the system with rotary pump backing for maintaining high vacuum. However the metal vapour in the processing zone, if swept to the high vacuum system, pose hazard to the TMP. Hence a vapour protection baffle is provided at the mouth of the TMP although it reduces the conductance and the pumping speed. The pressure is measured at two different locations with full range combination gauge, Penning and Pirani gauge. With proper
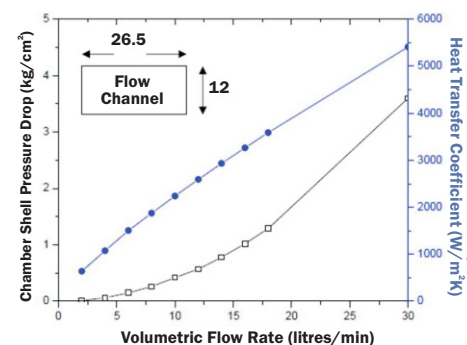

Fig.4: Thermal hydraulic design curve for the shell.

Fig.5: Separator shell with square bars as structural reinforcements and water flow channels.
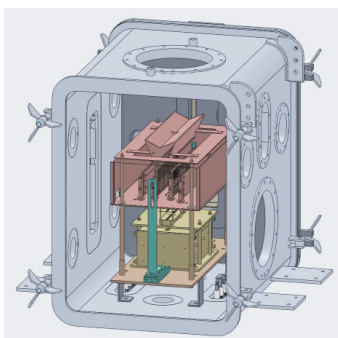

Fig.6: Schematic assembly view with vapour source, collimator, laser aperture and ion collectors.

Fig.7: Assembly of electrostatic photo-ion collectors.

outgassing of the system, the chamber operates at baseline pressure of ~2×10^{-6} mbar.

Laser-Atom interaction and Ion extraction system

There are four major systems to be aligned inside the process chamber, i.e., vapour source, collimator, laser beam and ion collectors. The alignment and its repeatability become critical as any misalignment leads to a direct reduction in the efficiency of the process. As an example, misalignment of 1mm between the a laser beam of 10mm diameter irradiating a 10mm atomic beam leads to ~10% loss of product generation efficiency.

The laser-atom interaction and ion collection system is designed with a philosophy of guided manual installation. Each of the four systems is built from a single reference and the parts are aligned to the fit-up tolerance of the components leading to fast and accurate assembly (Fig.6 and 7).

Laser multi-pass Optics

The lasers used in the LIS system are routed multiple times through the processing zone. This is done by plane parallel mirrors place at the two longitudinal ends of the processing zone. If the multipass optics is placed outside the chamber boundary, there is an ease in operation but there is loss every time the laser beam passes through the optical window which becomes significant as the number of laser passes increases. Essentially this is loss of precious photon. This loss of laser power is avoided when the multipass optics system is placed inside the vacuum boundary. The mirror maneuvering becomes complex as the motions are controlled through stepper motors however the system has more laser

Fig.8: Commissioned Separator with external optics box and high vacuum system.

power available at the processing zone. To accommodate the optics inside the chamber vacuum boundary, a separate optics enclosure is attached to the chamber which has separate door for independently handling the optics inside. The radiative heating of the optics box from the high temperature vapour source is minimized to protect the multipass optics housed inside. The optics boxes are optimized in size to reduce the volume addition as these are also evacuated though the main vacuum system of the chamber (Fig.8).

Conclusion

In conclusion, the separator development was a work of assimilating knowledge and ideas from multiple disciplines involved in the LIS work including various aspects of structural, thermal hydraulic and kinematic design, high vacuum design, handling of precision optics and ion extraction systems, design of high voltage system specifically to work with photoplasma. The system has been commissioned. It is being used for characterization of the separator internals and also for LIS experiments.

Acknowledgements

Bibliography

[1] P. A. Bokhan et al., Laser Isotope Separation in Atomic Vapor, WILEY-VCH Verlag GmbH&Co., ISBN-13: 978-3-527-40621-0.

[2] P.R.K. Rao, Laser isotope separation of uranium, Current Science, 2003, **85**, 615 .

[3] Hyunmin Park et al., Laser Isotope Separation of 176Yb for Medical Applications, Journal of the Korean Physical Society, 2006, **49**(1), 382-386.

[4] Biswaranjan Dikshit and Archana Sharma, Design and Analytical Evaluation of a New Ion Collection Geometry for Improvement in Quantity and Quality of Product During Laser Isotope Separation, IEEE Transactions on Nuclear Science, 2020, **67**(12), 2465- 2473.

[5] Ilora G Finlay, Malcolm D Mason and Mike Shelley, Radioisotopes for the Palliation of Metastatic Bone, Cancer: A Systematic Review, Lancet Oncol, 2005, **6**(6), 392-400.

Isotope Separation

Analytical Approach to Understand Laser Isotope Separation Process of Yb-176 for Non Carrier Added (NCA) Radioisotope Lu-177

K. K. Mishra[1]*, M. Mascarenhas[1] and Archana Sharma[2]

[1]*Laser and Plasma Technology Division, Beam Technology Development Group, Bhabha Atomic Research Centre, Mumbai-400085, INDIA*
[2]*Beam Technology Development Group, Bhabha Atomic Research Centre, Mumbai-400085, INDIA*
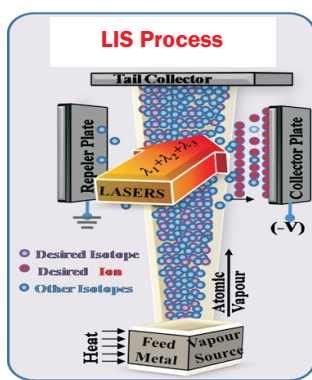
LIS enrichment Process for Yb-176

ABSTRACT

Lutetium-177 (Lu-177) has emerged as a promising short range β-emitter for targeted radiotherapy. There are two ways to produce Lu-177. One is the Carrier Added (CA) method in which Lu-176 is used as a source material and second method is Non Carrier Added (NCA) wherein enriched Yb-176 is used as a source metal in nuclear reactor. Natural abundance of Yb-176 is only 13%, however the isotopic purity requirement of source material concentration is more than 95% of Yb-176. Laser Isotope Separation (LIS) method has been intensively used worldwide to produce high enriched Yb-176 (more than 95%) in weighable amount (10-20 mg/hr). At Bhabha Atomic Research Centre (BARC), multiple experiments for LIS of Yb-176 have been conducted in RIS facility of BTDG. Yb-176 enriched to 97.1% with Yb-174 1.09% has been obtained at mass production rate 5 to 10 mg/hr. In this paper a mathematical model of the LIS process applicable for high enrichment factor with mg quantity as required for medical isotopes is presented. Data generated from the model was compared with experimental results.

KEYWORDS: *Lutetium-177, Carrier Added (CA) Method, Laser Isotope Separation (LIS), Non Carrier Added (NCA) Method, LIS Process, Yb-176, Enrichment of Yb-176.*

Introduction

Lutetium-177 (Lu-177) has emerged as a promising short range β-emitter for targeted radiotherapy[1-2]. Demand of Lu-177 has increased many folds. Lu-177 is produced [3-5] in a nuclear reactor through irradiation of source material with neutrons. Currently, there are two ways to produce Lu-177. One is Carrier Added (CA) method in which Lu-176 used as a source material and second method is Non Carrier Added (NCA) where in enriched Yb-176 used as a source metal in nuclear reactor. Due to chemical difference between Lu-177 and Yb-176 carrier free Lu-177 is possible by separating Lu-177 from Yb-176 chemically. Natural abundance of Yb-176[6] is only 13%, however the isotopic purity requirement[7] of source material concentration is more than 95% of Yb-176 and less than 5% of Yb-174 (natural abundance 32%) to produce high activity Lu-177 in nuclear reactor.

Laser Isotope Separation (LIS) method[8-9] has been intensively used worldwide to produce high enriched Yb-176 (more than 95%) in weighable amount (10-20 mg/hr). At Bhabha Atomic Research Centre[10-11] extensive work has carried out for various isotopes. With this experience and utilization of RIS facility of Beam Technology Development Group in BARC multiple experiments for LIS of Yb-176 have been conducted. Enriched Yb-176 97.1% with Yb-174 1.09% has been obtained at mass production rate 5 to 10 mg/hr. In literatures various physical aspects of LIS process are already discussed.   .

Author for Correspondence: K. K. Mishra
E-mail: kkmishra@barc.gov.in

The aim of this paper is to present a mathematical model of the LIS process applicable for high enrichment factor with mg quantity as required for medical isotopes. Model is based on isotropic mass balance and change of isotropic concentration of target isotope with controllable process parameters. The outcome of this calculation such as enrichment factor and mass of enriched Yb-176 is compared with the plant data obtained in RIS facility.

In LIS process, atoms of target isotope (Yb-176) in vapor stream get ionized after interaction with tuned laser beam. Ionized atoms are separated from the main vapor stream by electrostatic field. In the RIS facility a resistive heating system has been designed to evaporate Ytterbium by sublimation at temperature in the range of 780K to 820K to provide adequate Yb vapor atoms for laser interaction. The in house dye laser pumped by cover vapor laser (CVL) and Diode Pumped Solid State Laser (DPSSL) has been developed to selectively ionize Yb-176. Extraction mechanism of charged isotope Yb$^+$-176 has been designed [12] in house.

Evaporation and Free Jet Expansion from a Rectangular Slit

During the process, the linear vapor jet coming out from a crucible at pressure (10–20 Pa) freely expands into vacuum chamber of pressure 10^{-3} Pa. As pressure ratio (source/background) is higher than critical ratio $[(\gamma+1)/2]^{\gamma/(\gamma-1)}$ = 2.05 (from gas dynamics), the vapor jet comes out from source reach to sonic speed at the exit plane, then it expand supersonically into vacuum. Properties of vapor at source as well as at a height are discussed below.

Vapor Pressure of Yb metal [13] is given by

$$Log_{10}P_0 = 14.117 - 8111/T_0 - 1.0849\,Log_{10}T_0 \qquad (1)$$

(Where P_0 in Pa)

Number density at source is calculated from ideal gas equation as

$$n_0 = \frac{P_0 A_v}{T_0 R_0} = \frac{P_0}{kT_0} \qquad (2)$$

Average thermal velocity of atom from kinetic theory of gas is given by

$$V_{th} = (8RT_0/\pi)^{0.5} \qquad (3)$$

Knudsen number[14-15] is the ratio of mean free path of atom to the dimension of source. It is an important parameter of the vapor source which governs flow dynamics of vapor jet issuing out from reservoir. The Knudsen number at source influences the atomic properties of vapor at atom-laser interaction zone. Mathematically it is given by Eqn. 4

$$kn_0 = \frac{\lambda}{w} = \frac{1}{1.414x\pi d^2 n_0 w} \qquad (4)$$
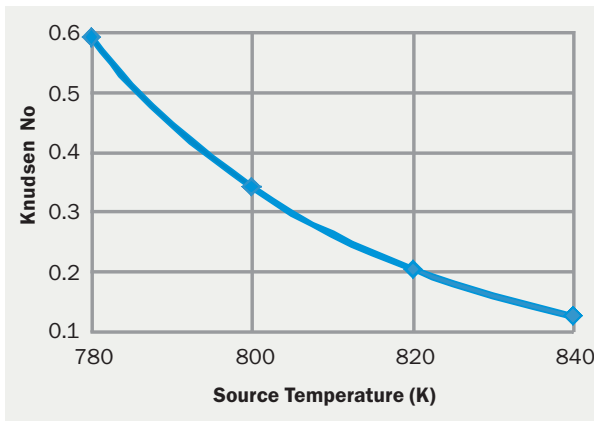

Fig.1: Variation of source Knudsen No with temperature.

It is seen from Fig.1 that Knudsen number remains in between 0.3-0.2 during evaporation of Yb in operating temperature range 800-820K. This is the transition regime of vapor flow where continuum gas flow equations[14] do not apply. Hence, continuum properties of free jet expansion is not discussed in this paper. In is model, vapor jet properties after expansion are calculated by using analytical equations derived by Monte Carlo particle test method for three dimensional non-collisional flow from a rectangular slit[16].

Number density[16] at height r from source plane

$$n_r = n^* \times (w/L) \times n_s \qquad (5)$$

Where, n_s is number density at sonic plane of source[15] given by

$$n_s = (2/Y+1)^{1/(Y-1)}n_0 = 0.65n_0 \qquad (6)$$

and n* is the geometric expansion factor[16] decides change in number density with height and is given by

$$n^* = [\{(1+(L/r)^2\}^{0.5}-1]/(2\pi) \qquad (7)$$

Variation of number density during process at different location is shown in Fig.2. Number density at atom-laser interaction zone comes down by three orders from source.
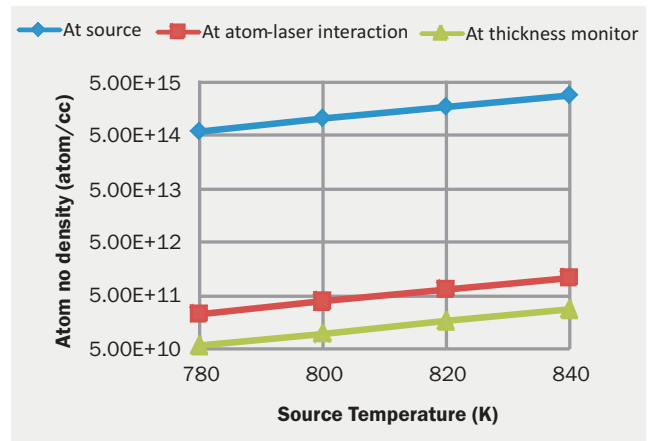
Fig.2: Variation of number density (Eqn.5) at various locations with source temperature.

Estimation of Thickness Monitor Data

Thickness monitor reading gives average arrival rate of atomic vapor in terms of thickness per unit time (A/sec). Product of mass density and thickness rate gives mass flux of metal vapor. Mass flux is also the product of number density of atom and its average velocity. Equating equation of mass flux

$$S_\rho = (M/A_v)\, n_T\, v_{th} \qquad (8)$$

Where, n_T is number density of Yb atoms striking at the thickness monitor. Since, at a larger height velocity of atom reaches v_{th} calculated at source temperature.

After substituting the values of constant and material properties thickness rate for Yb atoms comes to

$$S = 4.17x10^{-11}nv_{th}\ A/sec \qquad (9)$$

Where, n from Eqn.5 in atom/cc and v_{th} from Eqn.3 in m/s.

Matching of experimental and theoretical data for thickness monitor provides an additional check to get the accurate number density of vapor atoms in atom-laser interaction zone.

Fig.3: Variation of thickness monitor reading with source temperature.

Mass Balance and Enrichment Factor During LIS Process

Mass flow during LIS process is described in Fig.4

For total mass balance

$$F = P + W \qquad (11)$$

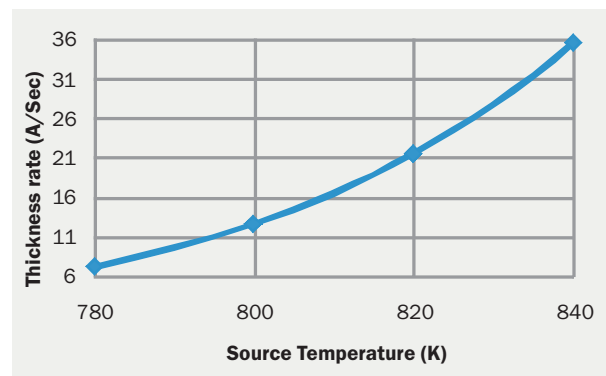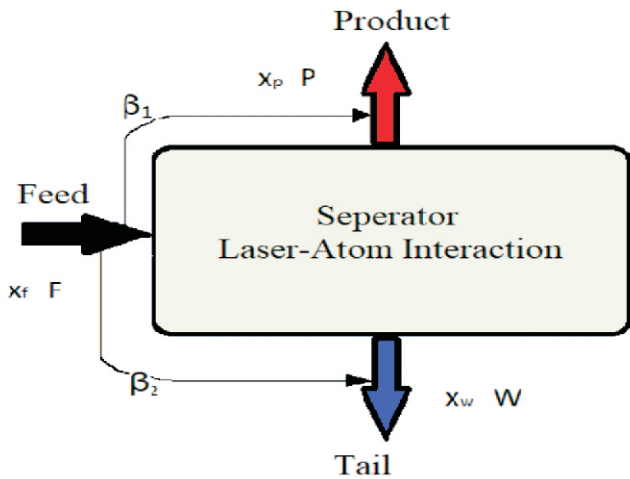*Fig.4: Mass flow during LIS process.*

For Yb-176 mass balance

$$x_f F = x_p P + x_w W \qquad (12)$$

Where, feed is given by Eqn.13 and its variation with source temperature is presented in Fig.5

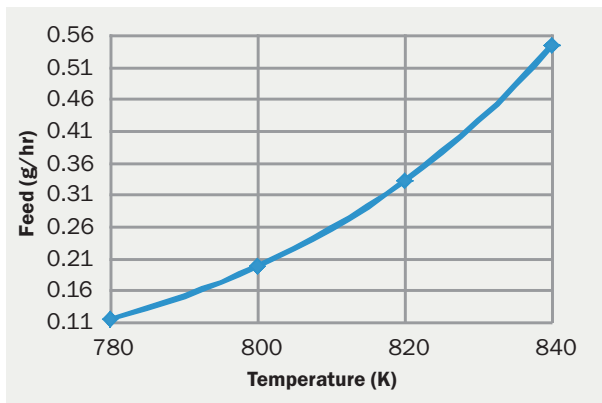$$F = (nV/t)(M/A_v) = 5.1727E\text{-}10 \, n \text{ mg/hr} \qquad (13)$$

Fig.5: Variation of feed with source temperature.

Quantity and Quality of Product

Process of mass collection on product collector is shown in Fig.6.

Total mass of Yb deposited at product collector P=Non-selective pick-up + Collection of Yb-176 ions after ionization and extraction.
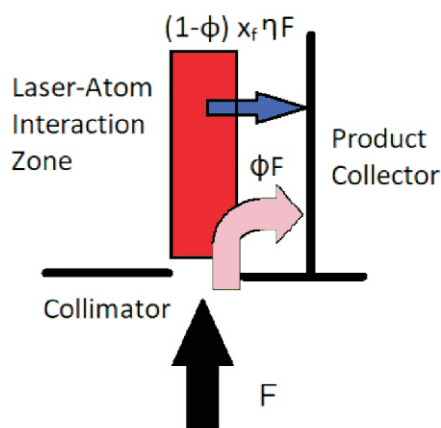
Fig.6: Deposition of material on product collector.

$$P = \Phi F + (1 - \Phi) \eta x_f = [\Phi + (1 - \Phi) \eta x_f] F \qquad (14)$$

From equation-14 it is evident that product collection is linearly depends on stripping efficiency as well as non-selective pick-up for a given feed.

Deposition of only Yb-176 at product collector

$P^{Yb\text{-}176}$ = Collection of Yb-176 due to non-selective pick-up + Collection of Yb-176 ions after ionization and extraction

$$P^{Yb\text{-}176} = [\Phi x_f + (1 - \Phi) \eta x_f] F \qquad (15)$$

Concentration of Yb-176 at product collector is given by Eqn.16

$$x_p = \frac{P^{Yb\text{-}176}}{P} = \left[\frac{\Phi + (1 - \Phi)\eta}{\Phi + (1 - \Phi)\eta x_f} \right] x_f \qquad (16)$$

Separation factor is given by Eqn.17

$$\beta_1 = \frac{x_p}{x_f} = \frac{\Phi + (1 - \Phi)\eta}{\Phi + (1 - \Phi)\eta x_f} \qquad (17)$$

As per equation-16 product quality (x_p) depends only on non-selective pick-up and striping efficiency for a given feed concentration. Variation of product quality is shown in Fig.7.
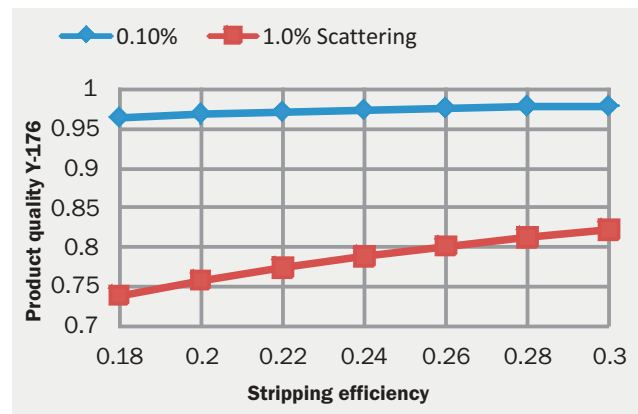
Fig.7: Variation of enrichment of Yb-176.

It is seen from Fig.6 that non-selective pick-up plays a major role to get high enrichment of more than 95% of Yb-176. Extraction geometry for product collection is designed such that non-selective pick-up comes down to 0.1% of feed.

Mass of 97.1% enriched product Yb-176 collected on product collector is shown in Fig.8 for various source temperatures (or feed) and stripping efficiencies. Production rate of 97.1% enriched isotope Yb-176 at a stripping efficiency 22% can be achieved in the range of 9 mg/hr to 16 mg/hr by
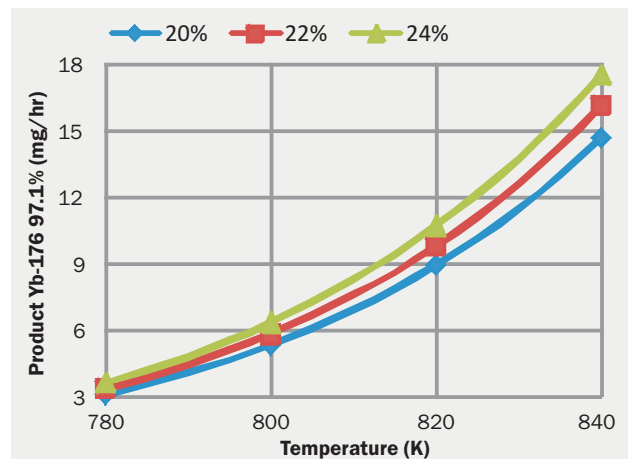
Fig.8: Variation of product mass (Eqn.14) for non-selective pick-up 0.1%.
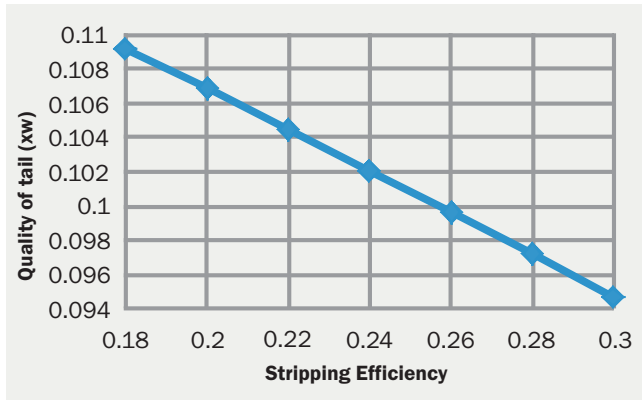
Fig.9: Variation of depletion of Yb-176 (Eqn.18).

controlling evaporation source temperature in between 820K to 840K. Hence, it is clear that production rate is very sensitive to the source temperature.

Mass depleted in Yb-176 collected at tail collector. Concentration of Yb-176 at tail collector is given by Eqn.18

$$x_w = \frac{(1-\eta)x_f}{(1-\eta x_f)} \qquad (18)$$

Depletion factor is given by Eqn.19

$$\beta_2 = \frac{x_f}{X_w} = \frac{(1-\eta x_f)}{(1-\eta)} \qquad (19)$$

Eqn.18 shows that depletion factor does not depend on scattering but decreases with increasing stripping efficiency as expected (Fig.9).

Comparison of Experimental Data with Analytical Values are listed in Table Below

| Description	Experiment	Model
Temperature of crucible	810 K	820 K
Height of thickness monitor	240 mm	240 mm
Rate of deposit on thickness monitor	20 A/s	21.4 A/s
Non selective pick up (Scattering)	0.1%	0.1%
Stripping efficiency $\eta = \eta_a \times \eta_i \times \eta_{ex}$	18–28%	22%
Quantity of product	5.57 mg/hr	9.82 mg/hr
Quality of Yb-176 at product collector	97.1%	97.1%
Quality of Yb-176 at tail collector	9.12%	10.4%

Conclusions

Product quality 97.1% Yb-176 is achieved with stripping efficiency of 22% or more by restricting non-selective pick-up less than 0.1%. Product collection of 5.57mg/hr during experiment is less as compared to model value of 9.82 mg/hr. Moreover, concentration of Yb-176 at tail collector is less during experiment as compared to the model data. Both facts suggest that collection of enriched product is insufficient during experiment. So extraction mechanism and product collection geometry is to be improved.

Notations

L = source length

w = source width

A = source area (wxL= 5mm x 100mm)

T_0 = Source temperature

P_0 = Source Pressure

n_0 = number density at source

M = Atomic weight of Yb=173

R_0 = Universal gas constant = 8314 J/mole-K

γ = Specific heat ratio = 5/3 for monotonic gas

$R = R_0/M$ = Characteristic gas constant = 48.05 J/kg-K

A_v = Avogadro No

$k = R_0/A_v$ = Boltzman constant

d = atomic diameter

kn_0 = Knudsen number at source

λ = Mean free path of atom

S = thickness rate

ρ = mass density of Yb,

F = Feed or Throughput or mass supplied to atom-laser interaction volume

P = Product mass collected at product collector

W = Tail or waist mass collected at other location known as tail

x_f, x_p, x_w : Concentration of Yb-176 in feed, product and tail respectively

β_1 = Enrichment Factor = (x_p/x_f)

β_2 = Depletion Factor = (x_f/x_w)

Φ = Non selective pick-up (or Scattering efficiency) = Fraction mass of feed that reach to product collector without seeing laser

η_a = Fraction of Yb-176 atoms in laser interaction zone available for atom –photon reaction

η_i = Ionization efficiency= Fraction of Yb-176 atoms which ionized by laser in interaction zone

η_{ex} = Extraction efficiency = Fraction of ionized Yb-176 atoms collected at product collector

η= Stripping efficiency of Yb-176 ions (Ionization, extraction etc) = Overall fraction of Yb-176 atoms which go to laser interaction zone that collected at product collector

$\eta = \eta_i \times \eta_{ex} \times \eta_a$

n = Average no density of atom at laser interaction volume, atom/cc

V = Volume of interaction zone (10 mm x 40mm x 100mm = 40 cc)

v = Frequency of laser (rep rate) Hz = 12500 Hz

t = Time for single pulse = 1/12500 sec = 80 x 10^{-6} sec

References

[1] J. L. Parus, R. Mikolajczak, Beta-emitting radionuclides for peptide receptor radionuclide therapy. Current Topics in Medical Chemistry 2012, **12**(23), 2686-93.

[2] A. M. R. Pillai, F. F. Knapp, Evolving Important Role of Lutetium177 for Therapeutic Nuclear Medicine. Current radio-pharmaceuticals, 2015, **8**(2), 78-85.

[3] V. A. Tarasov, O. I. Andreev et al., Production of No- Carrier Added Lutetium177 by Irradiation of Enriched Yb-176, Current Radiopharmaceuticals, 2015, **8**, 95-106.

[4] A. Dash, A. M. R. Pillai, Jr. F. F. Knapp, Production of Lu-177 for targeted radio nuclides therapy, Available Options, Nul Med Mol Imaging 2015, **49** (2), 85-87.

[5] W. V. Vogel, et al., Challenges and future option for the production of Lu-177, Eur Jl of Nuclear Medicine and Molecular Imaging, 2021, **48**, 2329-2335.

[6] R. John de Leater and Nino Buklic, The isotopic composition and atomic weight of ytterbium. June 2006 International Journal of Mass Spectrometry, **252**(3), 222-227.

[7] Y. G. Toporov, et al., Production of high specific activity 177-Lu preparation using SM research reactor, 5th International Conference on Isotopes Brussels, Belgium, 25–29 April 2005 , 10.

[8] O. I. Andreev, et al., Production of highly enriched Yb-176 isotope in weight amounts by the atomic vapour laser isotope separation method, Quantum Electronics, 2006, **36**(1), 84-89.

[9] H. Park, et al., Laser Isotope Separation of Yb-176 for medical Applications Journal of Korean Physical Society 2006, **49**(1), 382-386 .

[10] P. R. K. Rao, Laser Isotope Separation of Uranium, Current Science, 2003, **85**, 615.

[11] Kundu S, et al., Summary of experimental results of RIS facility and Future projection, BARC/2020/R/006.

[12] B, Dikshit, A. Sharma, Design and analytical evaluation of a new ion collection geometry for improvement in quantity and quality of product during laser isotope separation; IEEE Trans Nuclear Science, 2020, **67**(12), 2465-2473.

[13] C. B. Alcock Vapor pressure of metallic elements, 2000, CRC Press LLC.

[14] G. A. Bird, Molecular Gas Dynamics and Direct Simulation of Gas flow, Clarendon Press, Oxford, 1994.

[15] J. Mukharjee, K. K. Mishra, L. M. Gantayet, Study of free jet expansion, BARC/1995/E/016.

[16] A. Rosengard, Three Dimensional Free jet Flow from a finite Length Slit, Rarefied Gas Dynamics, ed. Muntze, et al., 1988, (16th RGD), 312-326.

Isotope Shift Calculations

Quantum Chemical Calculations of Vibrational Frequencies and Associated Isotope Shifts in SF_6, MoF_6, and UF_6: A DFT Study

Ayan Ghosh* and J. Padma Nilaya

Laser and Plasma Technology Division, Beam Technology Development Group,
Bhabha Atomic Research Centre, Mumbai-400085, India
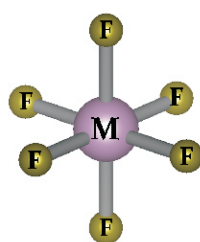
Structure of MF_6 (M = S, Mo, and U)
O_h Symmetry

ABSTRACT

The accuracy of the performance of DFT functional in estimating the vibrational isotope shift in any chemical system motivated us to determine the isotope shift of the fundamental vibrational modes of SF_6, MoF_6, and UF_6 molecules by employing B3LYP, PBE0, and M06 functionals. They have also been employed to explore the molecular structure, stability, harmonic vibrational frequencies, and charge distribution. The isotope shifts (Δv_3) have been found to be 17.1-17.8, 1.0-1.2, and 0.63-0.67cm^{-1} for the $^{32}SF_6$-$^{34}SF_6$, $^{97}MoF_6$-$^{98}MoF_6$, and $^{235}UF_6$-$^{238}UF_6$ isotopomers, respectively, that agree well with the experimentally measured isotope shifts.

KEYWORDS: *Hexafluorides, Density Functional Theory, Structure and Stability, Vibrational Frequency, Isotope Shift.*

Introduction

Enrichment of relevant isotopes through efficient techniques is important for the front-end of the Indian nuclear fuel cycle and medical industry in addition to being a deterrent in the current world scenario. The enrichment of the ^{235}U isotope (natural abundance 0.72%) understandably therefore, assumes a significant role. Of the many radio-isotopes employed in radiopharmaceutical industry, ^{32}P that is used for the bone pain palliation in the skeletal metastases is produced in N-reactor through the bombardment of ^{32}S by fast neutrons. ^{99m}Tc radio-isotope is known as the 'Work Horse' in Nuclear Medicine as more than 80% of radiopharmaceuticals use this isotope. It is prepared from the $^{99}Mo/^{99m}Tc$ generator where ^{99}Mo itself is produced in a nuclear reactor through ^{98}Mo (n, γ) ^{99}Mo reaction. ^{99}Mo emits particle and eventually decays to ^{99m}Tc. Since the medical radio-isotopes are administered to the patients, the radio-chemical as well as the radio-nuclide purity is of utmost importance. To obtain the required specific activity, ^{32}S and ^{98}Mo having natural abundances 94.99% and 24.29% need to be suitably enriched.

Among all the existing enrichment processes, *viz.*, gas diffusion, gas centrifuge, electromagnetic separator, laser isotope separation (LIS) processes, the LIS is considered most promising as it is known to be an energy efficient process with a relatively much smaller foot print. The LIS process that employs molecular gas as the working medium, termed the molecular laser isotope separation (MLIS) where the desired isotopic species is selectively excited and separated through infrared multi-photon dissociation (IRMPD) was earlier considered impractical owing to the requirement of prohibitively high

power of coherent light. However, there has been a resurgence of interest in it of late due to the so called SILEX (Separation of Isotopes by Laser Excitation) technology[1] that, although not explicitly spelt out in open literature, is most likely based on low-energy processes[2]. In this direction, very recently, Makarov and co-workers have reported very high enrichment factor for ^{34}S isotope in SF_6 by employing the laser assisted gasdynamic expansion scheme[3].

Due to several advantages, *viz.*, the mono-isotopy of fluorine atom, higher vapor pressure, gaseous form at room temperature, the MF_6 (M = S/Mo/U) is considered to be the most suitable molecule for the separation of isotopes of S, Mo, and U. It is essential to have a prior knowledge of the vibrational frequencies and the associated isotope shifts of the molecules of interest to be able to selectively excite the desired isotopic species and separate it from the rest. This information may not be obtainable from literature for all molecules of interest and hence the calculation of the vibrational frequencies and the corresponding isotopic shifts assumes significance. In this article, we present the geometry optimization of a molecule followed by the vibrational frequency calculations for obtaining the isotope shift in SF_6, MoF_6, and UF_6 molecules by employing density functional theory (DFT).

Computational Methodology

All the theoretical computations have been carried out by using density functional theory based methods in Turbomole-7.2.1 software[4]. The structures of MF_6 (M = S, Mo, and U) have been optimized in singlet ground electronic spin state using two hybrid DFT GGA functionals, *viz.*, Becke three-parameter exchange and Lee–Yang–Parr correlation (B3LYP)[5] and hybrid form of Perdew-Burke-Ernzerhof exchange and correlation (PBE0) [6]; and a hybrid DFT meta-GGA functional,

*Author for Correspondence: Ayan Ghosh
E-mail: ghosha@barc.gov.in

Table 1: Optimized M-F bond length (R_{M-F}) in Å, Partial NPA charges on 'M' atom (q_M) and each 'F' atom (q_F), HOMO Energy (E_{HOMO}) and LUMO Energy (E_{LUMO}) and their gaps (ΔE_{Gap}) in eV for MF_6 (M = S, Mo, and U) molecules by using B3LYP, PBE0, and M06 methods with DEF2 basis set.

Molecule	Methods	$R_{M-F (Calc.)}$	$R_{M-F (Expt.)}$	q_M	q_F	E_{HOMO}	E_{LUMO}	ΔE_{Gap}
SF_6	B3LYP	1.580	1.561[a]	2.612	−0.435	−12.025	−2.109	9.917
	PBE0	1.566		2.610	−0.435	−12.405	−1.295	11.109
	M06	1.558		2.679	−0.446	−12.455	−1.349	11.106
MoF_6	B3LYP	1.817	1.817[b]	2.427	−0.404	−12.349	−5.869	6.480
	PBE0	1.817		2.434	−0.406	−12.743	−5.549	7.193
	M06	1.820		2.475	−0.413	−12.825	−5.672	7.152
UF_6	B3LYP	2.007	1.996[c]	2.358	−0.393	−−11.855	−6.460	5.395
	PBE0	1.988		2.335	−0.389	−12.120	−6.000	6.120
	M06	1.994		2.412	−0.402	−12.249	−6.352	5.897

[a]Ref. [10]; [b]Ref. [11]; [c]Ref. [12]

i.e., Minnesota exchange-correlation-2006 hybrid with 27% HF exchange (M06) [7]. For F, S, and Mo (28 electrons ECP) atoms, we have used def2-TZVPP basis set [8] while def-TZVPP basis set[8] has been employed for the U (60 electrons ECP) atom as implemented in the Turbomole software. This combination of basis set is defined as DEF2. The accuracy of the electron density based (DFT) methods coupled with basis sets is well known for the calculation of the electronic structure of any molecular system and its properties. The choice of larger basis set (DEF2) along with the abovementioned DFT functionals has shown to yield accurate results[9] in the electronic structure calculations of any chemical system using molecular orbital theory based techniques.

Optimized Structural Parameters of MF_6

The DFT based methods with B3LYP, PBE0, and M06 functionals have been employed to optimize the electronic structures of all the MF_6 (M =S, Mo, and U) molecules and the true minima in their respective singlet potential energy surfaces is obtained. The optimized structure of MF_6 (Fig.1) exhibits octahedral geometry having O_h symmetry at its minima. Table 1 lists the M-F bond distances in all the MF_6 (M = S, Mo, and U) molecules as obtained by using all the three abovementioned methods. The M-F bond lengths have been found to be in the range of 1.558-1.580, 1.817-1.820, and 1.988-2.007Å in SF_6, MoF_6, and UF_6 molecules, respectively, and the corresponding experimental values are 1.561, 1.817, 1.996Å. From the above results, it is evident that the calculated M-F bond distances are in close proximity with the experimental data lending credence to the adopted methodology.

Stabilities of MF_6 Molecules

The stability of any molecular system can be inferred from their HOMO-LUMO energy gaps (Energy gap between the highest occupied molecular orbital and lowest unoccupied molecular orbital) and the same for MF_6 molecules have been reported in Table 1 as obtained by employing all the adopted methods. Here, the S, Mo, and U atoms are bonded with the highest electronegative element F atom whereby the HOMO is stabilized significantly for all the MF_6 molecules. The computed values of HOMO-LUMO gap are in the range of 9.917-11.109, 6.480-7.193, and 5.395-6.120eV for SF_6, MoF_6, and UF_6, respectively. Higher value of ΔE_{Gap} for all the MF_6 systems
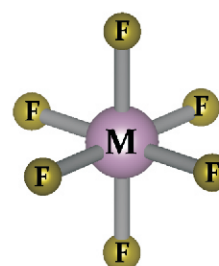

Fig.1: Optimized structure (O_h) of MF_6 (M=S, Mo, U).

studied here clearly emphasizes the greater stability of the systems with a very strong M–F bond.

Natural Population Analysis (NPA) of MF_6

The computed net NPA charges on M and F atoms in MF_6 (M = S, Mo, and U) have been reported in Table 1 as obtained by all the DFT functionals. From the Table 1, it is clearly evident that there is a significant charge distribution among all the constituent atoms in all the MF_6 molecules. The charges acquired by the M atoms are found to be 2.612, 2.427, 2.358 along the series S–Mo–U, while the corresponding charge residing on each F atom are -0.435, -0.404, -0.393 in SF_6, MoF_6, and UF_6 molecules, respectively, as obtained by B3LYP

Table 2: Fundamental vibrational frequencies (v_i in cm^{-1}) for $^{32}SF_6$ along with the isotope shift (Δv_i in cm^{-1}) for the $^{34}SF_6$ isotopomer in the parenthesis.

Modes (Deg.)	B3LYP	PBE0	M06	Expt.[a]
v_1 (A_{1g})	743.3	777.9	801.5	774.5
v_2 (E_g)	616.1	645.1	655.9	643.4
v_3 (T_{1u})	909.7 (17.1)	956.1 (17.8)	976.9 (17.4)	947.9 (17.1)
v_4 (T_{1u})	590.3 (2.7)	607.2 (2.9)	632.4 (2.8)	615.0 (2.6)
v_5 (T_{2g})	502.5	516.0	537.0	523.5
v_6 (T_{2u})	329.5	341.1	363.2	346.9

[a]Ref. [10]

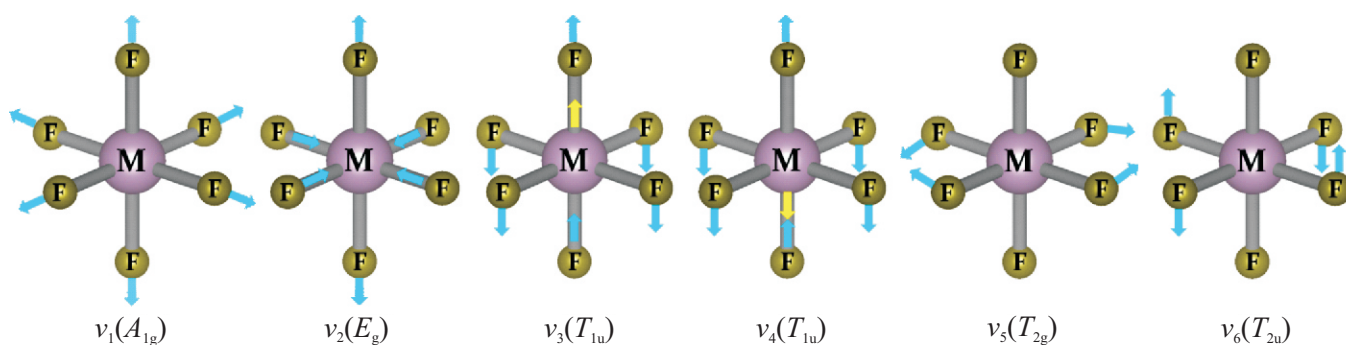$$\nu_1(A_{1g}) \qquad \nu_2(E_g) \qquad \nu_3(T_{1u}) \qquad \nu_4(T_{1u}) \qquad \nu_5(T_{2g}) \qquad \nu_6(T_{2u})$$

Fig.2: Fundamental vibrational modes of the hexafluoride (MF_6, M = S, Mo, and U) molecules.

method with DEF2 basis set. This implies that the positive (~+2) charge residing on the M center is being neutralized by the six negatively charged F atoms via electron transfer from the M atoms to the F atoms. This is attributed to the strong covalent M–F bond with large charge delocalization and electrostatic interaction between the oppositely charged centers.

Vibrational Frequency Analysis and Estimation of Isotope Shift in MF_6

One of the best ways to test the accuracy of any method is to analyze its ability to reproduce the vibrational frequencies of the molecular system. We have performed harmonic vibrational analysis in order to distinguish the different vibrational modes for the characterization of the MF_6 chemical system. In this context, it is to be noted that two electron density based methods (B3LYP and M06 functionals) accurately compute the vibrational frequency for the DHP ($^{12}C_5H_8^{16}O$) molecule, as can be seen when matched with the experimentally available data for abundant isotope[9]. Among various DFT functionals, B3LYP, PBE0, and M06 have been found to reproduce the vibrational frequency more accurately for all the hexafluoride (MF_6, M = S, Mo, and U) molecules. Therefore, the calculated vibrational frequency values for the SF_6, MoF_6, and UF_6 molecules at B3LYP/DEF2, PBE0/DEF2, and M06/DEF2 levels are given in Table 2, 3 and 4, respectively.

Since the octahedral (O_h) geometry is the lowest energy structure of all the MF_6 molecules, therefore, all the molecules

Table 3: Fundamental vibrational frequencies (ν_i in cm^{-1}) for $^{98}MoF_6$ along with the isotope shift ($\Delta\nu_i$ in cm^{-1}) for the $^{97}MoF_6$ isotopomer in the parenthesis.

Modes (Deg.)	B3LYP	PBE0	M06	Expt.[a]
ν_1 (A_{1g})	739.2	762.2	751.8	741.0
ν_2 (E_g)	642.8	661.1	654.2	643.0
ν_3 (T_{1u})	732.6 (1.0)	750.4 (1.1)	737.8 (1.2)	741.0 (1.0)
ν_4 (T_{1u})	257.2 (0.3)	259.0 (0.4)	264.3 (0.4)	264.0 (0.2)
ν_5 (T_{2g})	307.6	311.3	309.8	306.0
ν_6 (T_{2u})	118.9	120.6	135.7	190.0

[a]Ref. [11]

Table 4: Fundamental vibrational frequencies (ν_i in cm^{-1}) for $^{238}UF_6$ along with the isotope shift ($\Delta\nu_i$ in cm^{-1}) for the $^{235}UF_6$ isotopomer in the parenthesis.

Modes (Deg.)	B3LYP	PBE0	M06	Expt.[a]
ν_1 (A_{1g})	662.0	684.9	663.3	663.9
ν_2 (E_g)	532.7	543.5	514.8	529.8
ν_3 (T_{1u})	617.2 (0.63)	635.6 (0.63)	614.1 (0.67)	627.5 (0.65)
ν_4 (T_{1u})	188.4 (0.2)	189.8 (0.2)	182.8 (0.3)	189.1 (0.2)
ν_5 (T_{2g})	200.9	201.5	187.9	193.7
ν_6 (T_{2u})	143.2	145.2	147.7	147.6

[a]Ref. [12]

possess six fundamental modes of vibrations, viz., ν_1-ν_6. Among all the modes, ν_1 is non-degenerate (A_{1g}), ν_2 is doubly degenerate (E_g), and ν_3-ν_6 are triply degenerate (T_{1u}, T_{1u}, T_{2g}, T_{2u}) vibrational modes. Being a centrosymmetric molecule, Raman active modes cannot be IR active and vice-versa. Therefore, MF_6 has three Raman-active (ν_1, ν_2, ν_5) modes, two IR-active (ν_3, ν_4) modes, and one forbidden (ν_6) mode. Tables 2, 3, and 4 include all possible vibrational frequencies computed using the aforementioned DFT functionals, along with their degeneracy for the MF_6 molecules.

The pictorial representation of all the vibrational modes as obtained computationally agrees very well with experimental findings is represented in Fig.2. Since irradiation of the MF_6 molecules is possible with IR lasers, ν_3 and ν_4 modes are of our interest. Between ν_3 and ν_4, the frequency value for the ν_3 mode is higher than the corresponding ν_4 mode and generally, the isotope selective excitation of the ν_3 vibrational mode has been attempted experimentally. For the highest abundant isotopes, the calculated vibrational frequencies for ν_3 mode in $^{32}SF_6$, $^{98}MoF_6$, and $^{238}UF_6$ as shown in Tables 2, 3 and 4 are close to the experimental data available.

For the determination of the isotope shift ($\Delta\nu$), the IR frequencies have been calculated for all the isotopomers of MF_6. The difference in vibrational frequency with respect to that of the molecule with abundant isotopic species is termed 'Isotope Shift'. For SF_6, the isotope shift ($\Delta\nu_3$) values have been found to be 8.5-8.9 and 17.1-17.8cm^{-1} for the $^{32}SF_6$-$^{33}SF_6$ and $^{32}SF_6$-$^{34}SF_6$ isotopomers, respectively, while the corresponding experimental values are 8.6 and 17.1 cm^{-1}. In case of MoF_6, 1.0-1.2 and 2.1-2.4cm^{-1} are the isotope shifts between the $^{97}MoF_6$-$^{98}MoF_6$ and $^{98}MoF_6$-$^{100}MoF_6$ pairs. The isotope shift value was found to be 0.63-0.67cm^{-1} for $^{235}UF_6$ and $^{238}UF_6$ isotopomer while the experimentally measured value from literature is

0.65 cm^{-1}. As can be seen, the calculated values match pretty well with the experimental data available. The slight variation in the theoretically computed fundamental vibrational frequency values with the experimental data may also arise due to the anharmonicity effect which should be considered for precise determination of isotope shift. Further, the harmonic vibrational frequency analysis through some DFT functionals (B3LYP, PBE0, and M06) seem more promising methods for accurate determination of the isotope shift as reported by us[9].

Conclusion

The first principle based density functional theory based methods are important theoretical tools for the calculations of isotope shifts in the fundamental vibrational modes of the isotopomers. In order to determine the isotope shift, the geometry of the MF$_6$ (M = S, Mo, and U) molecules has been first optimized followed by fundamental vibrational frequency calculation for the different isotopomers of the molecules of interest. Knowledge of the fundamental vibrational frequencies and the corresponding isotope shifts play an important role in the choice of the process gas, the laser to be employed and the process parameter in molecular based laser isotope separation process.

Acknowledgements

References

[1] (a) www.silex.com.au; (b) SILEX Process www.chemeurope.com/en/encyclopedia/Silex_Process.html; (c) SILEX Uranium Enrichment SILEX Annual Report (2014), www.silex.com.au; (d) SILEX Uranium Enrichment SILEX Annual Report (2017), www.silex.com.au.

[2] J. L. Lyman, Enrichment separative capacity for SILEX Report LA-UR-05-3786 (2005) Los Alamos National Laboratory.

[3] V. N. Lokhman, G. N. Makarov, A. L. Malinovskii, A. N. Petin1, D. G. Poydashev, and E. A. Ryabov, Isotope-Selective Control of the Clusterization of SF$_6$ Molecules by an IR Laser during Gasdynamic Expansion of an SF$_6$/Ar Mixture. *Laser Phys.*, 2018, **28**, 105703, https://doi.org/10.1088/1555-6611/aad289.

[4] R. Ahlrichs, M. Bär, M. Häser, H. Horn, and C. Kölmel, Chem. Phys. Lett., 1989, **162**, 165. Available from http://www.turbomole.com.

[5] (a) A. D. Becke, A New Mixing of Hartree-Fock and Local Density-Functional Theories. J. Chem. Phys., 1993, **98**, 1372-1377, https://doi.org/10.1063/1.464304; (b) C. Lee, W. Yang, and R. G. Parr, Development of the Colle-Salvetti Correlation-Energy Formula into a Functional of the Electron Density. Phys. Rev. B, 1988, **37**, 785-789, https://doi.org/10.1103/PhysRevB.37.785.

[6] M. Ernzerhof and G. Scuseria, Assessment of the Perdew. Burke. Ernzerhof Exchange-Correlation Functional. J. Chem. Phys., 1999, **110**, 5029. https://doi.org/10.1063/1.478401.

[7] Y. Zhao and D. G. Truhlar, The M06 Suite of density functionals for Main Group Thermochemistry, Thermochemical Kinetics, Noncovalent Interactions, Excited States, and Transition Elements: Two New Functionals and Systematic Testing of Four M06-Class Functionals and 12 Other Functional. Theoret. Chem. Acc., 2008, **120**, 215-241, https://doi.org/10.1007/s00214-007-0310-x; Err. Theoret. Chem. Acc., 2008, **119**, 525. https://doi.org/10.1007/s00214-007-0401-8.

[8] F. Weigend and R. Ahlrichs, Balanced Basis Sets of Split Valence, Triple Zeta Valence and Quadruple Zeta Valence Quality for H to Rn: Design and Assessment of Accuracy. Phys. Chem. Chem. Phys., 2005, **7**, 3297-3305. https://doi.org/10.1039/B508541A

[9] A. Ghosh and J. P. Nilaya, Ab initio and DFT Benchmark Study for the Calculations of Isotopic Shifts of Fundamental Frequencies for 2,3-Dihydropyran. Struct. Chem., 2022. https://doi.org/10.1007/s11224-021-01829-4.

[10] R. S. McDowell, B. J. Krohn, H. Flicker, and M. C. Vasquez, Vibrational levels and anharmonicity in SF$_6$- I. Vibrational band analysis. Spectrochim. Acta., 1986, **42A**, 351- 369. https://doi.org/10.1016/0584-8539(86)80199-4.

[11] H. H. Claassen, H. Selig, and J. G. Malm, Vibrational Spectra of MoF$_6$ and TcF$_6$. J. Chem. Phys., 1962, **36**, 2888- 2890. https://doi.org/10.1063/1.1732396.

[12] D. M. Cox, and J. Elliott, IR Spectroscopy of UF$_6$, Spectrosc. Lett., 1979, **12**, 275-280. https://doi.org/10.1080/00387017908069153.
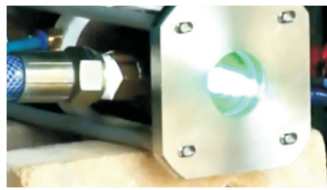
High Power Plasma Torch

Design and Development of Indigenous 100 kW Plasma Torch

R. L. Bhardwaj*[1], S. Lahiri[1], R. Shukla[2], M. L. Mascarenhas[1], Archana Sharma[3]

[1]*Laser & Plasma Technology Division, Bhabha Atomic Research Centre, Mumbai-400085, INDIA*
[2]*Pulse Power & Electromagnetics Division, Bhabha Atomic Research Centre, Visakhapatnam-531011, INDIA*
[3]*Beam Technology Development Group, Bhabha Atomic Research Centre, Mumbai-400085, INDIA*

High power plasma torch

ABSTRACT

Plasma technology is a vital tool in municipal and nuclear waste processing. The high temperature and high reactivity of free ions and radicals of the plasma make it a powerful medium to promote high heat transfer and chemical reactions, thereby enabling gasification of organic materials. Beam Technology Development Group is developing a 100kW thermal plasma torch indigenously. This article gives a brief overview of design basis and the progress of work towards the development of the plasma torch.

KEYWORDS: *Plasma torch, 100 kW plasma torch*, *HC torch, Electrode.*

Introduction

Hollow Cathode (HC) air plasma torches are generally used in high power applications. They are advantageous compared to pin type torches at higher power. A typical hollow cathode plasma torch is shown in Fig.1. It consists of two hollow electrodes made of copper and separated by a narrow gap of 2 mm.

Air as plasma gas is injected through a vortex chamber to achieve swirl action. Arc root attachments in both the electrodes moves continuously. This movement is both in longitudinal and radial direction. Longitudinal movement of arc attachment occurs by achieving dynamic equilibrium between Lorentz force and drag force. Lorentz force is a function of arc current while drag force is a function of gas flow rate. These two forces act in opposite direction and due to their dynamic behaviour generates voltage fluctuations in saw-tooth form. The frequencies of the fluctuation are linked to arc current, anode design and nature of plasma gas. The location of arc attachment and erosion rate of the electrode material determines the lifespan of the electrodes.

In this article, we discuss briefly the design and performance parameters of HC torch like variation of arc voltage, thermal efficiency of torch and oscillation frequency of voltage using similarity criteria given in literature [1-4]. These parameters were calculated for the range of utility limits available at site. A preliminary aerodynamic study was also conducted to characterize the air flow and the temperature distribution due to the air, considering plasma as a heat source.

Design basis

Following are the design criteria for thermal plasma torch intended to use for treatment of organic wastes:

a) High thermal efficiency for economical treatment.

b) Large volume of high temperature region for easy decomposition of organic wastes.

c) Abundant oxygen quantity sufficient for transforming the decomposed wastes into stable and innoxious elements.

d) Low electrode erosion rate for long lifetime of the torch.

Power source and utilities for plasma torch

The power source for a thermal plasma torch consists of a main arc power supply and a trigger power supply (Fig.2). The trigger power supply initiates the arc and main arc power supply gives energy to maintain it. A high voltage and frequency trigger power supply is used for igniting the arc discharge whilst using Argon as the plasma gas. Once a breakdown is initiated, the plasma gas is changed to air. The main arc power supply has a capacity of 100kW (500V and 200A).

Design by similarity criteria

Zhukov had developed similarity criteria on the basis of dimensionless equations, describing physical phenomena
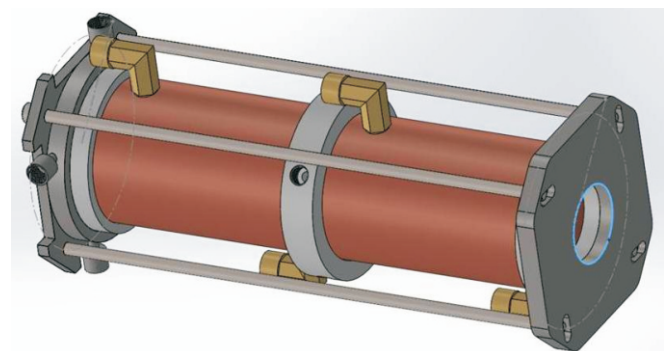
*Author for Correspondence: R. L. Bhardwaj
E-mail: radhe@barc.gov.in

Fig.1: Model of a HC torch.

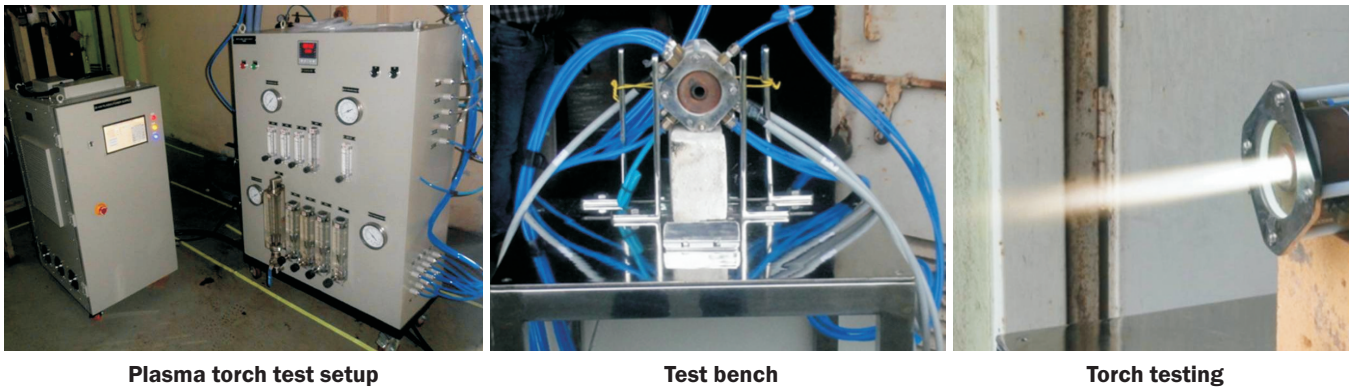| Plasma torch test setup | Test bench | Torch testing |

Fig.2: Plasma torch testing facility.

occurring in plasma torches. These dimensionless equations and validated our simulation results using literature values [2].

The maximum capacity of the main arc power supply (U, I), maximum plasma gas (G'), cooling water (g') determines the range of electrode dimensions.

Based on the following limiting conditions $0 < I < 200A$, $0 < U < 520V$, $0 < G' < 300slm$ @, g' = 50-60lpm, anode length (l_a) = 120mm and cathode (l_c) = 110mm and vertex diameter D= 45mm have been taken and the following combination of anode (da)-cathode (dc) diameters were used for study of electrode diameter effect on performance parameters

1. da=14mm & dc=16mm
2. da=14mm & dc=18mm
3. da=16mm & dc=18mm
4. da=16 mm & dc=20 mm

The variation of voltage (Fig.3a), efficiency (Fig.3b), and oscillation frequency of voltage were calculated w.r.t. the variation in current and gas flow rate based on similarity criteria. Following are the observations made:

a) The arc voltage decreases with rise in the arc current and concurs with a typical V/I characteristic of arc. It is clear from the graph (Fig.3a) that arc voltage decreases with increase in electrode diameter, however its change with cathode diameter is much more dominant than change in anode diameter.

b) Arc voltage increases with corresponding increase in the gas flow rate. The change in anode diameter is less dominant than the change in cathode diameter.

c) Efficiency of torch decreases with corresponding increase in the current. With increase in electrode diameter efficiency increases this is due to decrease in heat transfer from arc to electrode wall because the gap between these two increases however causing increase in gas flow rate requirement.

d) Frequency of oscillation of voltage increases with corresponding increase in arc current and is inversely proportional to square of anode diameter. The effect of change in cathode diameter is less dominant then that in anode diameter. However it does not varies much with variation in gas flow.

e) With increase in electrode diameter higher temperature zone in the plume spreads, which is an important performance characteristic. However axial velocity of plasma gas decreases with increase in electrode diameter leading to decrease in available oxygen flux for waste treatment. So, there should be an optimization among efficiency, high temperature zone and axial velocity.

Preliminary flow simulations

In order to optimize the flow rate of air for a particular diameter of torch, a typical distribution of temperature and
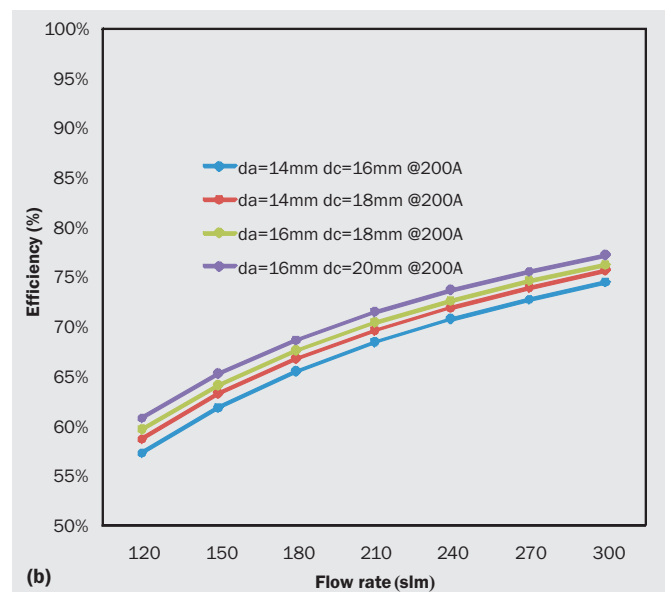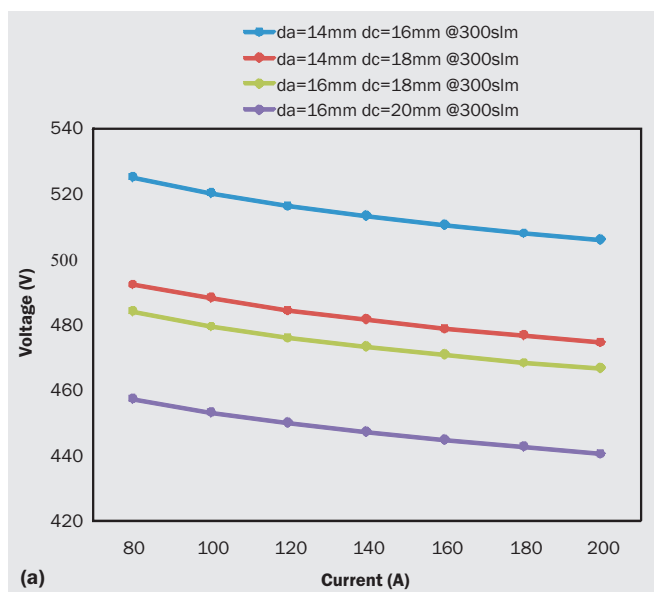

Fig.3: (a) Typical variation of arc voltage for different arc current for air flow rate = 300 slm
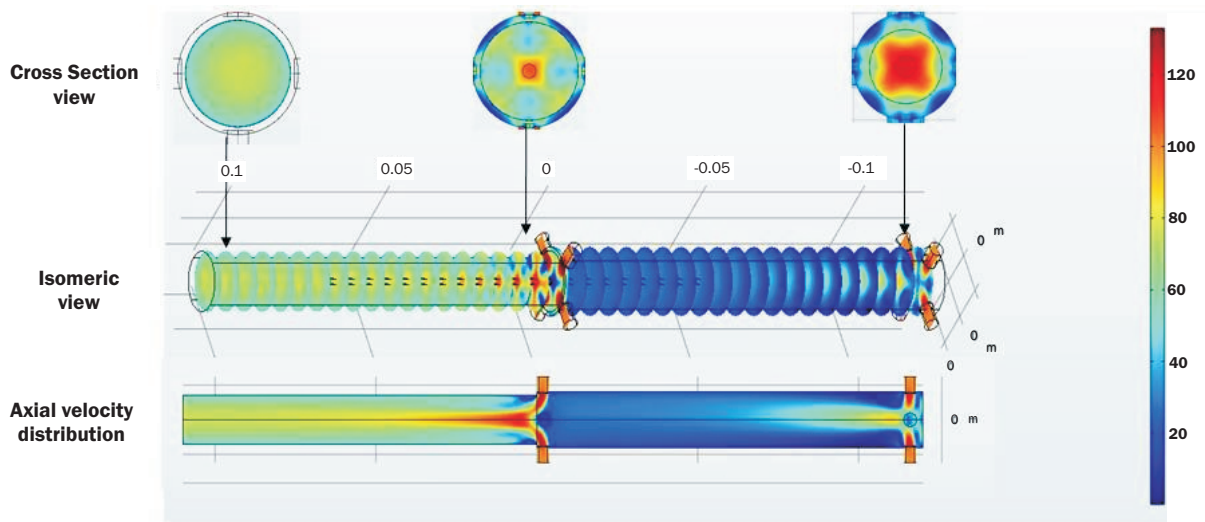*(b) Typical variation of efficiency for different gas flow rate.*

Fig.4: Typical velocity distribution (in m/s) of a 14 mm anode 16 mm cathode torch.
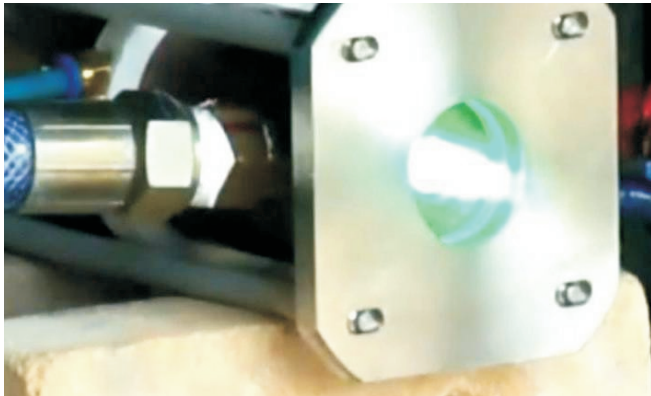

Fig.5: High power plasma torch testing at Hall-6 in BARC.

velocity (Fig.4) was simulated in commercial multiphysics simulation software, using the plasma as an extended heat source. Various combinations of nozzle geometry and flow rate variations were simulated and validated using data from literature [2].

Testing of the plasma torch

Based on the electrical and aerodynamic calculations, a plasma torch has been fabricated. It is being tested to achieve the optimum operating conditions, as shown in Fig.5.

Conclusion

Plasma torches act as high enthalpy sources that can be used in cutting, welding, spraying, machining, plasma metallurgy, underwater cutting and space simulations. Beam Technology Development Group is developing expertise in design, development and testing of high power plasma torches. In view of the widespread high power industrial and nuclear applications, the development of the 100 kW plasma torch by BARC will pave way for wider deployment of the technology in the near future.

References

[1] J.-F. Brilhac, et.al., Study of the Dynamic and Static Behaviour of dc Vortex Plasma Torches: Part II: Well-Type Cathode, Plasma Chem. Plasma Process., 1995, **15** (2), 257-276.

[2] Min Hur, et.al., Operational features and air plasma characteristics of a thermal plasma torch with hollow electrodes, Plasma Sources Sci. Technol., 2003, **12**, 255–264.

[3] M. F. Zhukov, I. M. Zasypkin, A. N. Timoshevskij, B. I. Mihailov and G. A. Desyatkov., Electric arc Thermal Plasma Generators, 1999, Novosibirsk: Nauka, 17.

[4] D. Y. Batomunkuev, S. P. Vashenko Electric arc plasmatorch of a two-chamber scheme with reverse polarity of electrodes connection, 2019, J. Phys.: Conf. Ser. **1393** 012003.
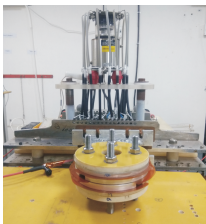
Magnetic Pulse Welding

Magnetic Pulse Welding of AA 5052 "Tube-Plug"

JMVVS Aravind*[1], Shobhna Mishra[1], Surender Kumar Sharma[1], G. Kiran Kumar[1], Rishi Verma[1], Rashmita Das[1], Basanta K. Das[1], Renu Rani[1], N. Sathi Babu[1] and Archana Sharma[1,2]

[1]*Pulsed Power & Electro-Magnetics Division, Bhabha Atomic Research Centre, Visakhapatnam, Andhra Pradesh-531011, INDIA*
[2]*Beam Technology Development Group, Bhabha Atomic Research Centre, Mumbai-400085, INDIA*

Magnetic Pulse Welding
Experimental setup

ABSTRACT

Magnetic Pulse Welding (MPW) is a solid-state joining process, in which a conductive flyer metal is accelerated to impact a target metal with high energy, thus forming a metallurgical bond. In the present article, compression MPW of Al-5052 tube (21.3mm I.D., 1.5mm thick) to Al 5052 plug is demonstrated. The impact velocity and time of impact are estimated using analytical equations. The experiment is performed at 15kV/295kA/23kJ, to obtain a helium leak rate better than 10^{-12}mbar. lit/s. Also weld interface morphology is studied and observed to be of wavy nature.

KEYWORDS: *Magnetic Pulse Weld (MPW), High Impact Welding, Interface Studies.*

Introduction

Magnetic Pulse Welding (MPW) is a well-established technology under the branch of solid-state joining processes, in which high impact pressure is generated to form a weld joint between two overlapping surfaces, by sequential collision of one metal over the other metal[1]. Fig.1. shows the schematic layout of MPW process.

The impact pressure is generated by discharging the electrostatic energy stored in a capacitor bank into the tool coil, which produces a magnetic field. This time-varying magnetic field when interacts with the flyer tube, it produces eddy currents in the flyer tube, which in turn shield the magnetic field from entering the flyer tube. This differential magnetic pressure on both sides of flyer tube accelerates it towards the target metal to collide with a high impact velocity. The main advantage of MPW is jetting action during the process cleans the contaminants, dirt, oxide layers and makes the clean metal surfaces to interact to form joining[1]. Along with the tool coil, a replaceable field shaper is used[2]. Usually, copper material is used for tool coil/field shaper because of its high electrical conductivity.

The chemical composition of AA 5052 is shown in Table. 1.

Table 1: Chemical composition of AA 5052 (in %)

Al	Mg	Si	Mn	Zn	Cr	Fe	Cu
95.7-97.7	2.2-2.8	0.25	0.1	0.1	0.15-0.35	0.4	0.1

AA 5052 is used in marine atmospheres because of its high corrosion resistance properties. Usually, welding of AA by Gas Tungsten Arc Welding (GTAW), Gas Metal Arc Welding (GMAW), *etc.*, faces a lot of drawbacks due to its high co-efficient of thermal expansion (α) and high thermal conductivity(κ). In MPW, there is no application of heat to melt the base metal,

*Author for Correspondence: JMVVS Aravind
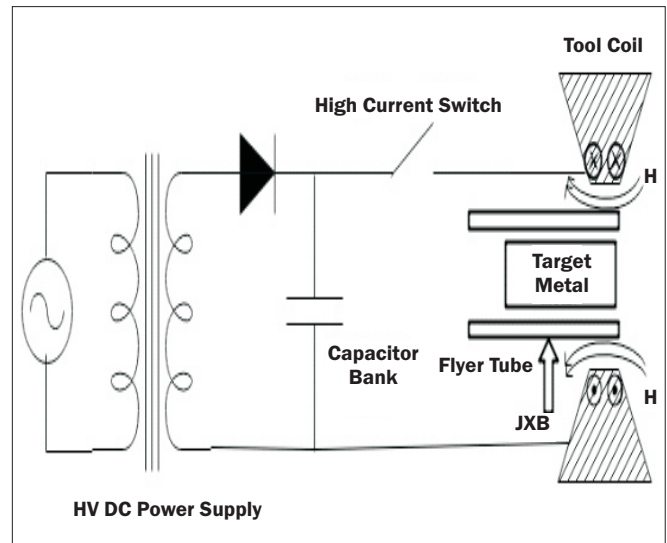*E-mail: jaravind@barc.gov.in*

Fig.1: Schematic layout of MPW system.

hence the tendency of cracking and HAZ is reduced. Also, the jet formed during the phenomenon itself clean the two mating surfaces to remove oxides. Expansion studies on AA 5052 has already been done[3].

After joining the metals, the bond quality is assessed by Destructive tests *viz.* Tensile test, Micrographic studies, *etc.* and Non-Destructive techniques *viz.* helium leak test, ultrasonic test, etc. In the present study, an attempt is made to perform the MPW of AA 5052 and to validate the joint established by Helium leak test and to study weld interface morphology.

Experimental Set Up

The MPW experimental installation is as shown in the Fig.2. It is having five sub-systems as explained in this paper.
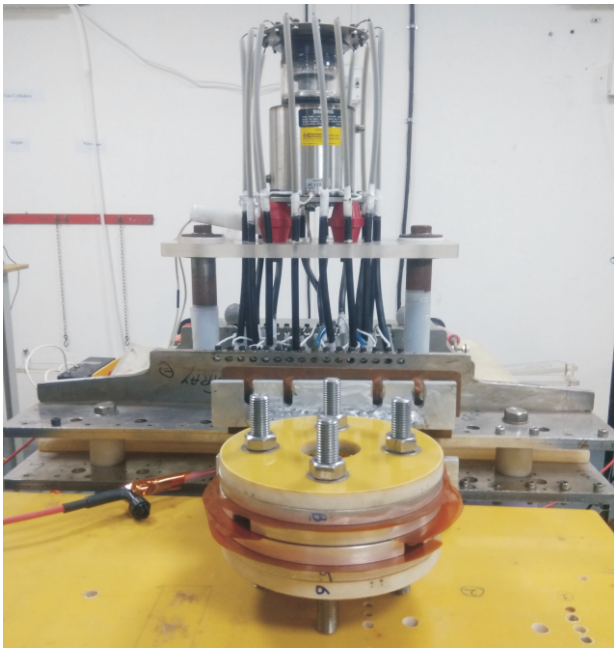
Fig.2: MPW experimental setup.

Power Supply: A 25 kV/ 800 mA HV DC power supply is used to charge the capacitor bank.

Energy Storage: A 208μF/44kV capacitor bank is used to perform the present MPW studies. For the present study, the capacitor bank is charged up to a voltage of 15kV, with a stored energy 23kJ.

High Current Switch: A high voltage and high current Ignitron switch (model NL8900) and trigger module is used to discharge the stored energy in the capacitors into the load.

Tool coil and field shaper: A four-disc Aluminium bitter coil and field shaper (ETP grade copper) as shown in schematic Fig.3 is used for the present study.
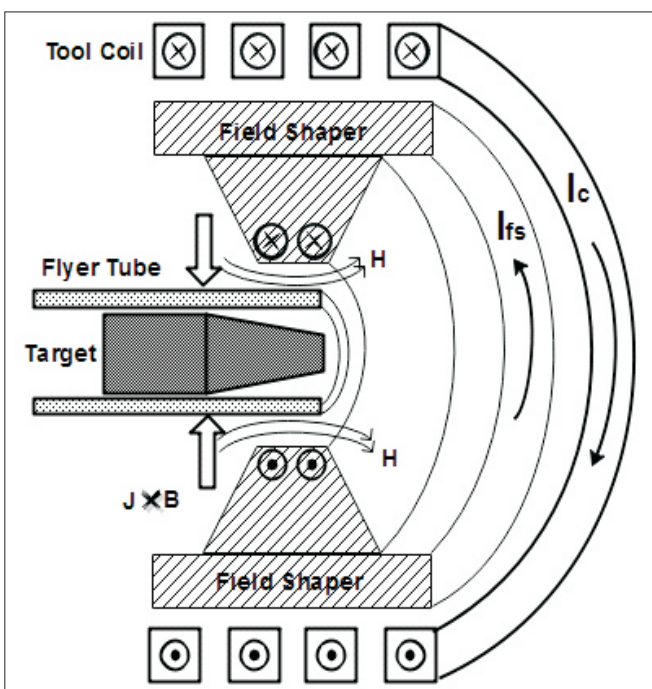

Fig.3: Schematic showing 4-disc coil, field shaper and weld sample.

Table 2: Dimensions of job sample

Description	Value
Outer Diameter, O.D	21mm
Inner Diameter, I.D	18mm
Thickness, t	1.5mm
Total flyer length, T.L	15mm
Over Lap length, O.L	8mm
Target taper angle, θ	10^0

Job Sample: The job assembly is composed of flyer tube and target. The dimensions of assembly are tabulated in Table. 2.

Theoretical Details

Generation of Magnetic Pressure on flyer tube

When the sinusoidal current passes through the tool coil, magnetic field density (B) is generated in the annular air region between the field shaper and flyer tube as shown in Fig.3. The magnetic field intensity (H) can be solved using the Magnetic Diffusion equation.

$$\frac{1}{\mu\sigma} * \nabla^2 H = \frac{H}{t} \tag{1}$$

where, μ and σ represents the magnetic permeability and electrical conductivity of the respective medium.

The current density J in the flyer tube can then be find out using Ampere law.

$$\nabla \times H = J \tag{2}$$

This time varying magnetic field B, interacts with the eddy currents generated in the flyer tube with a current density J, which in turn develops a radial inward Lorentz force (F=JXB) on the flyer tube. The dynamic impacting pressure generated on the tube can be evaluated as,

$$P_{mag} = \int_0^t F.td = \frac{(B_{out}^2 - B_{in}^2)}{2}$$

$$P_{mag} = \frac{B_{out}^2 (1 - exp(-\frac{2t}{\delta}))}{2} \tag{3}$$

B_{out} and B_{in} are the magnetic field densities outside and inside the flyer tube. The skin depth at operating frequency can be calculated using $\delta = 1/sqrt(\pi f \mu \sigma)$.

Kinematics of flyer tube

The magnetic pressure used to initiate the deformation in the flyer tube is estimated using the mechanical properties of the material *viz.* yield strength, strain rate, *etc.*

$$P_{def} = \frac{\sigma t}{r} \tag{4}$$

Once this pressure is exceeded, the extra pressure applied is utilized to accelerate the flyer to sufficient impact velocity towards the target material. Hence, the pressure used to accelerate the flyer is solved using Eq. 5.

$$P_{acc} = P_{mag} - P_{def} \tag{5}$$

The instantaneous velocity profile and radial displacement of the flyer can be solved by integrating the above equation with respect to time.

$$vel(t) = \frac{1}{m} *_? \ Facc.dt$$

$$vel(t) = \frac{1}{m} *_? \ (Pacc * As).dt \qquad (6)$$

$$dis(t) = \ vel(t).dt \qquad (7)$$

where, As= l*2pr is the surface area of the tube.

The time required to impact the target material is called as impact time T_{imp}. This impact time depends on annular gap (between tube and target), magnetic pressure, discharge frequency, and varies along the weld length.

Results

Simulation Results

The Magnetic Field Density (B) and Magnetic pressure corresponding to the experimental conditions are calculated by solving the Eq. (1), (2) and (3) with the help of FEMM, version 4.2 software. Fig.4 shows the distribution of B field in shaper-flyer tube region at peak current instant. The peak values of B field, magnetic pressure is found to be 22Tesla, 192MPa, respectively. The radial gap between the tube and target is maximum at free end of flyer tube and decreases along its length towards the other side. Hence, for a uniform pressure
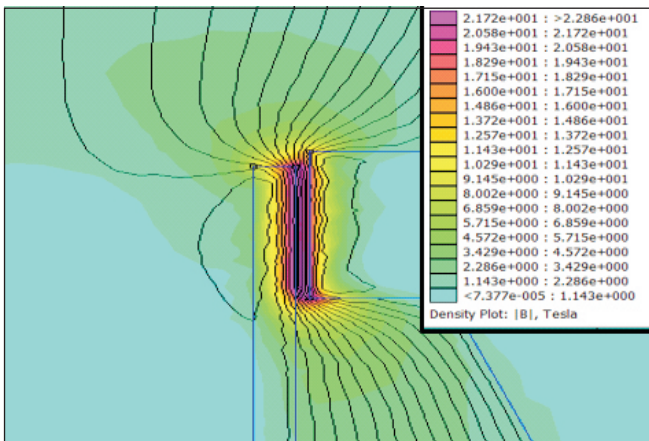

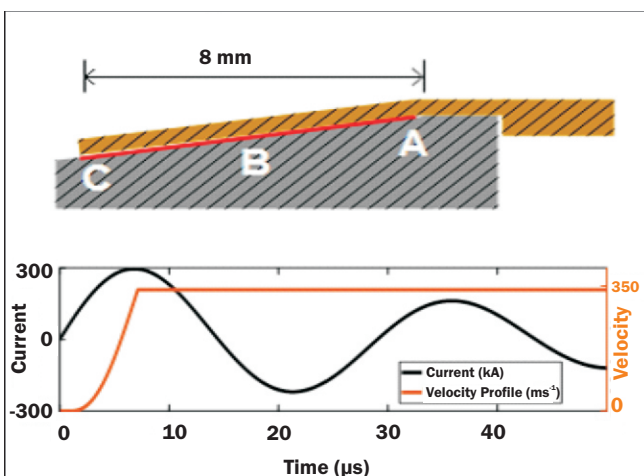Fig.4: Magnetic field, B pattern in field shaper-flyer tube assembly.

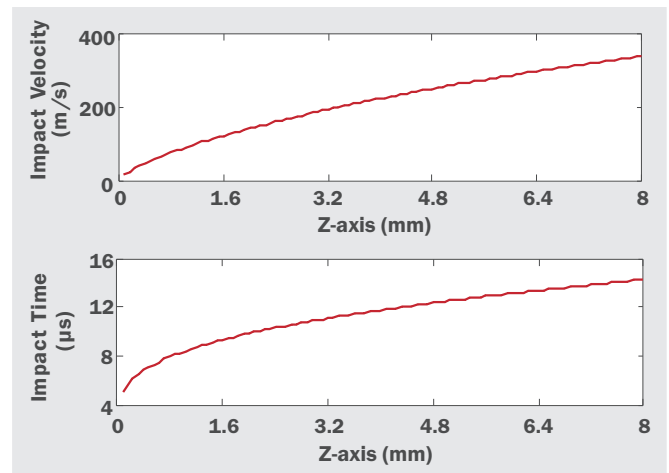Fig.5: Estimation of coil discharge current and velocity profile at point C.

Fig.6: : Estimated impact velocity and impact time (T_{imp}) along length of tube.

over its length, the collision is at an oblique angle and Fig.4 Magnetic field, B pattern in field shaper-flyer tube assembly sequential collision takes place along its length. Analytical equations are solved to estimate the velocity profile, radial displacement and time of impact.

Fig.5. shows the plot of estimated discharge current at 15 kV and velocity profile of the point C using numerical code. It is observed that the flyer tube end point C collides with the plug with impact velocity of 350 m/s at 14.5 μs, which corresponds to the quarter cycle of the current pulse.

Fig. 6 shows the plot of impact velocities and time of impact along the length of weld. The time instant of collisions at point A is earlier than point B and point C. This depicts that the sequential collision taking place along the weld length at some oblique angle.

Experimental Results

Fig.7. Shows the measured value of discharge current with a peak current of 295kA, when the capacitor bank is charged to a voltage 15 kV/23kJ. This peak current is obtained at 14.5μs, with a dominant frequency 18kHz. The corresponding skin depth can be evaluated as 0.5mm. The thickness of the Al 5052 flyer tube is 1.5mm (t>δ), to avoid magnetic field diffusion.

The welded sample is subjected to Helium leak test by using Mass Spectrometer Leak Detector (Pfeiffer make). The leak observed in the Helium environment is better than 10^{-12}mbar. lit/s. For further analysis, the Al-Al welded sample is
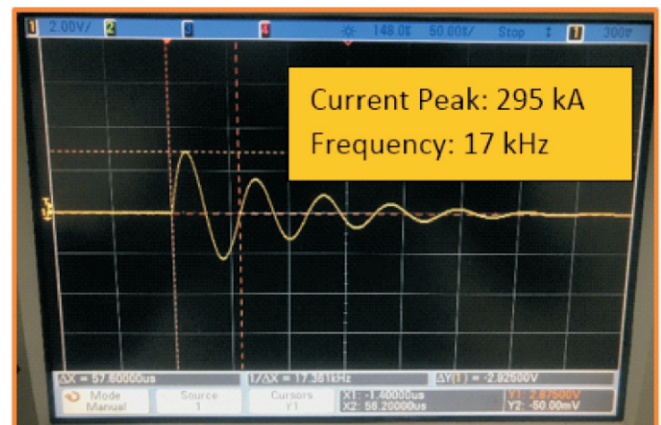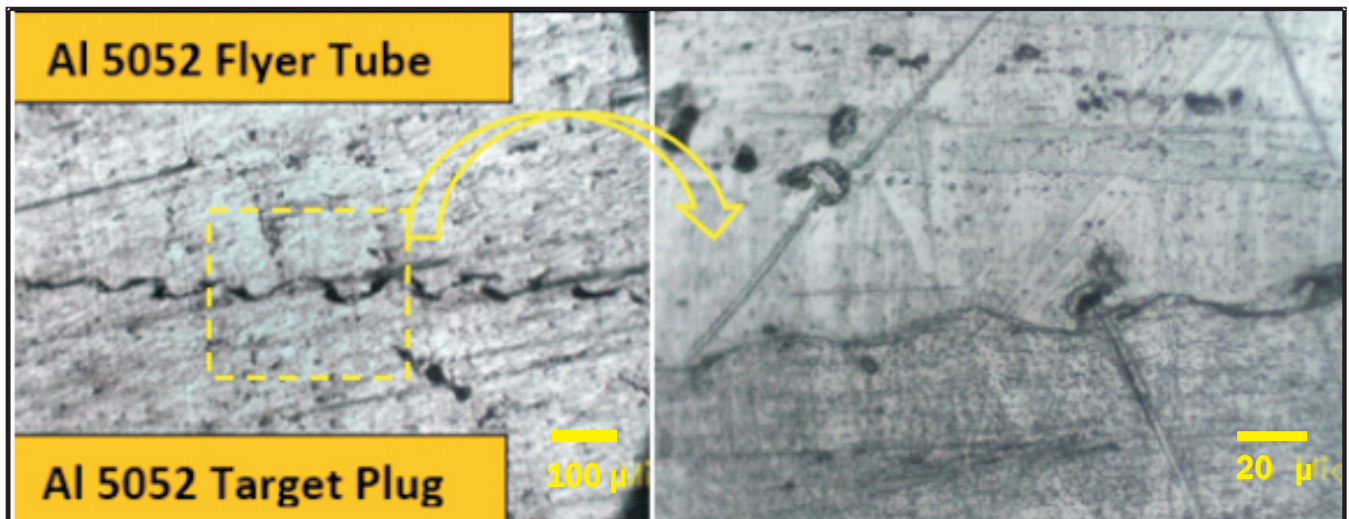

Fig.7: Discharge current waveform.

Fig.8: Optical microscopic image at 100x and 500x magnification.

sectionally cut along its length using a wire-cut EDM device. The sample specimen is moulded in Bakelite and polished for weld interface study using Optical Microscope. The metallographic images of specimen are as shown in Fig.8.

The image shows the wavy profile along the weld length which is a characteristic of high impact welding process. There are no signs of melting at the interface, which is an advantage of MPW technique. Out of 8mm overlap length, effective bonding is observed for a length of 2mm. This can be co-related to the simulated impact velocity of 280m/s to 330m/s in the previous section, which corresponds to 1.5mm away from the tip of the tube-target assembly.

Conclusion

The MPW of 21.3mm O.D., 1.5mm thick AA 5052 tube-plug has been demonstrated at 15kV/23kJ using a multi-turn coil. The following observations are noticed during experiments.

The Al 5052 material can be welded using MPW technique.

A typical signature of high impact welds i.e. wavy interface has been observed at estimated impact velocities of 280-330m/s.

An effective bonding is observed over a length of 2mm out of total weld length of 8mm.

References

[1] Psyk, Verena & D. Risch, & Kinsey, Brad & A. Tekkaya, & Kleiner, Matthias, Electromagnetic forming-A review. Journal of Materials Processing Technology, 2011, **211**, 787-829. 10.1016/j.jmatprotec.2010.12.012.

[2] Haiping Yu, Chunfeng Li, Zhiheng Zhao, Zhong Li, Effect of field shaper on magnetic pressure in electromagnetic forming, Journal of Material Processing Technology, 2005, **168**, 245-249.

[3] Shobhna Mishra, JMVVS Aravind, Renu Rani, Surender Kumar Sharma, Premanand Dey, Rohit Shukla, Ramanand Raman and Archana Sharma, Optimization of process parameters for Electromagnetic Expansion Welding of Aluminium Alloy Tube to block, Advances in Materials & Processing Technologies-AMPT, 2017.

Magnetic Pulse Welding

Titanium to SS-304 Dissimilar Metal Joints by Magnetic Pulse Welding

**Shobhna Mishra[1]*, JMVVS Aravind[1], Surender K. Sharma[1], G. Kiran Kumar[1], Rashmita Das[1],
Basanta K. Das[1], Rishi Verma[1], Renu Rani[1], N. Sathi Babu[1], Archana Sharma[2],
Gopa Chakraborty[3], Arun K. Bhaduri[4], Imran Khan[5] and Rajeev Kapoor[6]**

[1]Pulsed Power & Electromagnetics Division, Bhabha Atomic Research Centre, Visakhapatnam, Andhra Pradesh-531011, INDIA
[2]Beam Technology Development Group, Bhabha Atomic Research Centre, Visakhapatnam, Andhra Pradesh-531011, INDIA
[3]Metallurgy & Materials Group, Indira Gandhi Centre for Atomic Research, Kalpakkam, INDIA
[4]Homi Bhabha Chair, DAE, Indira Gandhi Centre for Atomic Research, Kalpakkam, INDIA
[5]Reactor Safety Division, Bhabha Atomic Research Centre, Mumbai-400085, INDIA
[6]Mechanical & Metallurgy Division, Bhabha Atomic Research Centre, Mumbai-400085, INDIA
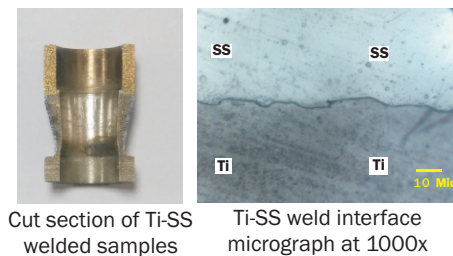
Cut section of Ti-SS welded samples

Ti-SS weld interface micrograph at 1000x

ABSTRACT

The fast reactor fuel reprocessing process flow includes the dissolution stage wherein the chopped fuel sub-assembly is dissolved in nitric acid in titanium-based dissolver units. These units needs to be further joined to the rest of the SS-304 based reprocessing plant along with ensuring the dissimilar metal joint integrity and corrosion resistant. The present work is to study the application of Magnetic Pulse Welding (MPW) for joining of Titanium to SS-304. This technique successfully established joints using a multi-turn and shaper tool coil at a peak magnetic field of 30T (350MPa), 17kHz frequency and impact velocity in the range of 250-350m/s. The welds attained helium leak rate of the order of 10^{-12}mbarl/s and a joining of ~1.2mm is observed with straight to wavy morphology. Microhardness profiling along the joint varied from ~166HV to ~230HV at Ti tube, ~290 to ~330 HV at the interface and ~156 to ~280HV at SS tube.

KEYWORDS: *Magnetic Pulse Welding(MPW), Dissimilar Metal Joining, Titanium, Stainless Steel.*

Introduction

Design of complex hybrid structures made up of dissimilar material combinations to meet the structural and functional requirements has increased the demand of dissimilar metal joining. Similarly, in fast reactor fuel reprocessing plant Titanium (Ti) to Stainless Steel (SS)-304 dissimilar metal joints with high reliability are quite significant. Ti to SS dissimilar metal joints established with fusion welding techniques has been challenging due to the difference in their thermal co-efficient, thermal conductivity and formation of brittle intermetallics. Magnetic pulse welding (MPW) is a solid-state impact welding process that utilizes magnetic pressure for joining of similar and dissimilar metals instead of heat source. This joining process is closely analogous to Explosive Welding (EXW) since both are having similar bonding mechanism i.e formation of jet action and a typical wavy morphology at the joint interface. MPW is a High Velocity Impact Welding (HVIW) technique that establishes lap joints between two colliding materials by utilizing the magnetic pressure generated with an electromagnetic tool coil, schematic as shown Fig.1.

This magnetic pressure is generated when capacitance energy is discharged into the tool coil through a switch and a time-varying magnetic field is established. When a conducting flyer material comes in contact with this magnetic field, eddy current is induced in the flyer that interacts with the magnetic field to produce Lorentz force that corresponds to the magnetic pressure. The flyer deforms under the pressure and accelerates over the stand-off distance available to impact on the target job at the critical velocity to establish a joint between them.

The interface morphology established in HVIW is known to be resulting from the jet effect and is classified into four types i.e. flat interface, wavy interface, vortex wave and continuous transition layer along the interface in the bond zone[3]. The worthiness associated with this technique is that there is no heating and melting of bulk material in this process, which eliminates formation of Heat Affected Zones (HAZ) and undesired oxides and nitrides at the joints, thereby avoiding
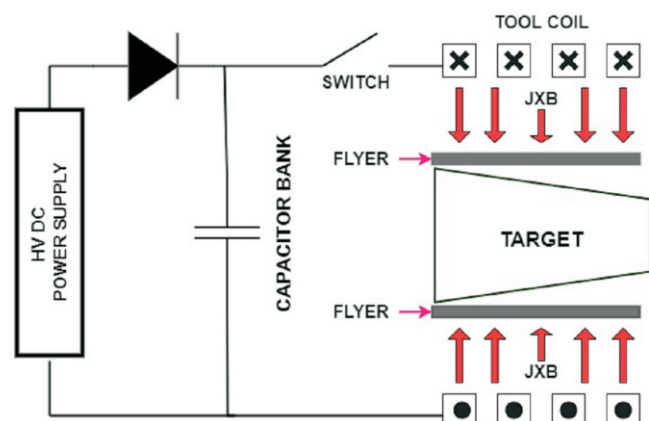

Fig.1: Schematic of MPW system.

*Author for Correspondence: Shobhna Mishra
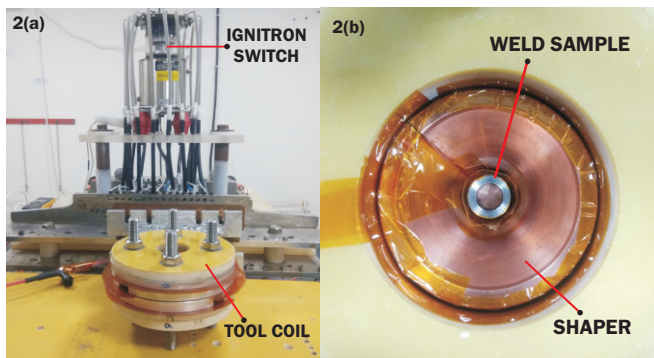E-mail: shobhnam@barc.gov.in*

Fig.2: Experimental setup.

Table 1: Material properties.

Material	Property	Value
Ti (Grade-2)	Yield strength, σ_y(MPa)	355
	Density, ρ(kg/m^3)	4520
	Electrical Conductivity, σ(S/m)	2.38×10^6
SS-304	Yield strength, σ_y(Mpa)	205
	Density, ρ(kg/m^3)	8000
	Electrical Conductivity, σ(S/m)	1.5×10^6
Copper	Yield strength, σ_y(MPa)	60
	Density, ρ(kg/m^3)	8960
	Electrical Conductivity, σ(S/m)	58×10^6

joint failures. This dissimilar joining technique is successfully employed to establish Ti tube to SS tube joints and the weld quality is examined with Helium leak rate, optical micrograph and micro hardness studies across the weld interface.

MPW Experimental Setup

A 200kJ/44kV capacitor bank system with total capacitance of 208µF is designed and developed for the MPW experiments. The experimental set up consists of a capacitor bank module comprising of four capacitors, having capacitance of 52µF each, charged through a High Voltage DC power supply with 25kV rated voltage and 800mA output current and the load i.e tool coil which is connected to the capacitor module through a high voltage and high current ignitron switch, as shown in Fig.2(a).

The magnetic field necessary to establish the required magnetic pressure is generated with a 4-disc aluminium alloy electromagnetic coil and is concentrated into the desired volume with a copper shaper, as shown in Fig.2(b).The job assembly comprises of a flyer, target, a copper mandrel to prevent target deformation and a copper driver over the flyer tube to eliminate magnetic field diffusion due to relatively low electrical conductivity of titanium, whose thickness has a direct co-relation with the system frequency. In the present setup, the flyer consists of Ti tube with copper driver and the target consists of SS tube supported with an inside copper mandrel, as shown in Figs.3&4. Table 1 shows material properties of Ti, SS-304 and Cu.

A critical impact angle between the colliding surfaces is necessary to ensure sufficient stand-off distance, i.e the initial gap between the impacting components, for accelerating the flyer to achieve the required impact velocity. In the present work, impact angle is provided on the SS target tube which

provides a gradually increasing stand-off distance for the Ti flyer, as seen in Fig.4 from point 1 to 2, so as to collide with the target at the critical impact velocity.

Analytical Details

In MPW, the required magnetic pressure is developed when the corresponding magnetic field is established in the annular space between the tool coil and the tubular conductive flyer. However, the magnetic field required to establish the joint varies based upon the flyer and target material, the standoff distance between them and can be produced by varying the capacitor charging voltage. The current induced in the copper driver tube, due to interaction with the time-varying magnetic field around, tends to penetrate along the tube thickness up to a depth known as skin depth. This skin depth depends upon the driver material's electrical conductivity σ (S/m), magnetic permeability µ and system frequency f(Hz). The driver tube thickness should be at least equal to the skin depth, δ given by(1) [4] so as to limit the magnetic field diffusion. Hence, the system frequency is chosen accordingly.
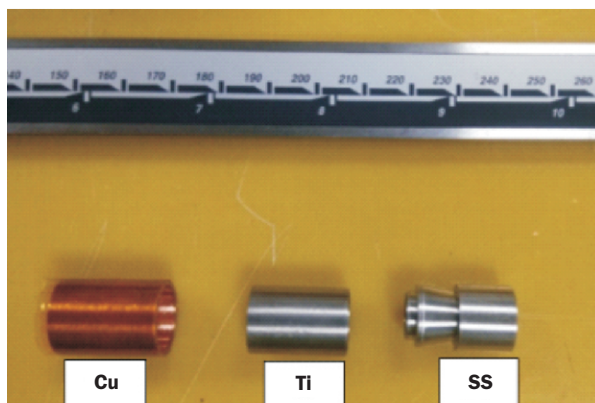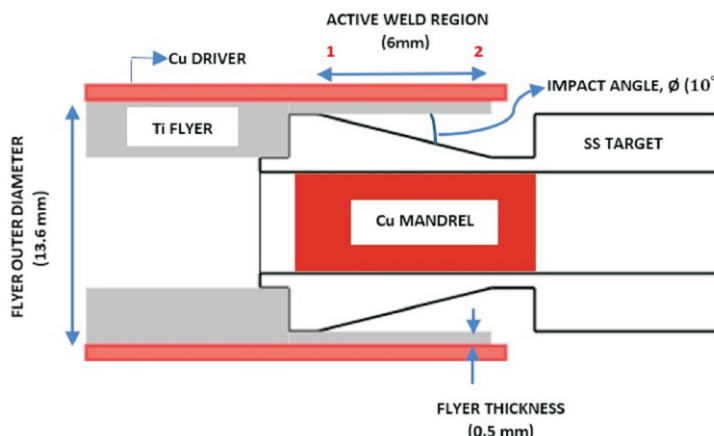

Fig.3: Copper driver & Ti-SS samples.

Fig.4: Copper driver & Ti-SS samples.

$$\delta = 1/\overline{\sqrt{\pi\sigma\mu f}} \qquad (1)$$

The interaction of the time-varying magnetic field with the induced eddy current in the flyer develops a Lorentz force. The total magnetic pressure, P (MPa) is obtained by integrating this Lorentz force over the tube and is also the summation of pressure required to deform, P_{def} and accelerate, P_{acc} the flyer tube and is as given in (2) [4, 5]

$$P = P_{def} + P_{acc}$$

$$P = t\,[2\sigma_y/R + \rho U_T^2/2s] \qquad (2)$$

Where, t(m) is flyer tube thickness, ρ(kg/m^3) is density of flyer tube material, s(m) is the initial stand-off, σ_y(MPa) is the yield strength of flyer tube material, U_T(m/s) is the flyer tube impact velocity, R(m) is the flyer tube initial radius. Based upon the flyer and target material the corresponding magnetic field, B(T) can be obtained from equation (3) [4,5].

$$P = B^2/2\mu(1- e^{-2t/\delta}) \qquad (3)$$

Where, μ is the permeability of the material, δ is the skin depth, t is flyer tube thickness, P is the magnetic pressure. The impact angle, impact pressure and impact velocity are the three critical parameters that decide the occurrence of weld and its quality. In order to obtain a successful weld through MPW a minimum threshold pressure value is to be exceeded. This pressure, P_{thres} is given by the relation (4)[6]

$$P_{thres} = 5\times\text{Hugoniot Elastic Limit }(HEL) \qquad (4)$$

Where, HEL is given by the relation (5)

$$HEL = \frac{1}{2}\left(\frac{K}{G} + \frac{4}{3}\right)\sigma_y \qquad (5)$$

Where, K is the bulk modulus (GPa) and G is the shear modulus (GPa).

The critical impact pressure, P_c required for jet formation that is related to impact velocity is as given in (6) [6]

$$P_c = \frac{1}{2}Zeq\,U_T\cos\varPhi \qquad (6)$$

Where, U_T is the critical impact velocity, $\varPhi$ is the critical impact angle for jet formation and Zeq is the equivalent acoustic impedance of the colliding tubes and is given by (7)[6]

$$Zeq = \frac{2}{\frac{1}{Z_1}+\frac{1}{Z_2}} \qquad (7)$$

Where, $Z_1 = \rho_1 S_1$ is the acoustic impedance of flyer tube, $Z_2 = \rho_2 S_2$ is the acoustic impedance of base tube, S_1 and S_2 are the speeds of sound in the flyer and target tube materials(m/s) respectively, and ρ_1, ρ_2 (Kg/m^3) are the material densities of the two tubes. The minimum velocity of impact U_T, also termed as critical impact velocity required for occurrence of weld in case of dissimilar metal combination can be determined by equating equation (4) and (6) and total magnetic pressure can be determined using equation (2) [6]. Also, the impact velocity, U_T and collision velocity, V_c (m/s)is related by (8), where β is the collision angle [7].

$$U_T = 2V_c\,sin\frac{\beta}{2} \qquad (8)$$

Experimental Results

A dissimilar metal joint between 13.6mm diameter, 0.5mm thick Ti to SS tube with impact angle 10^0 is successfully established using a 4-disc Al alloy coil with copper shaper at a peak magnetic field of 30T (350MPa) corresponding to peak current of 295kA, 17kHz frequency as shown in Fig.5.

I=295kA
f=17.39kHz
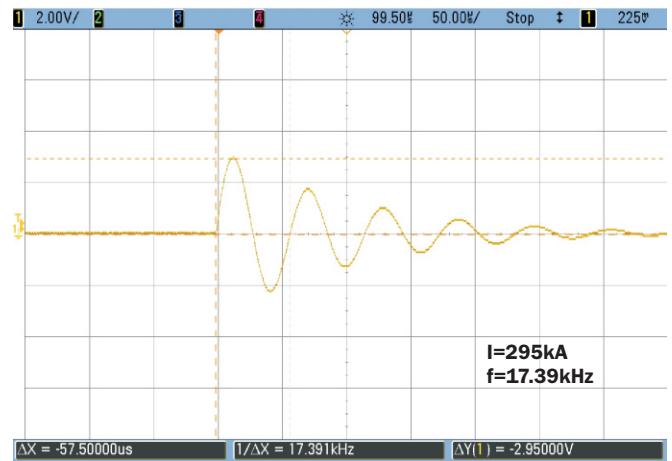
Fig.5: Discharge current waveform.

Before weld   **After weld**
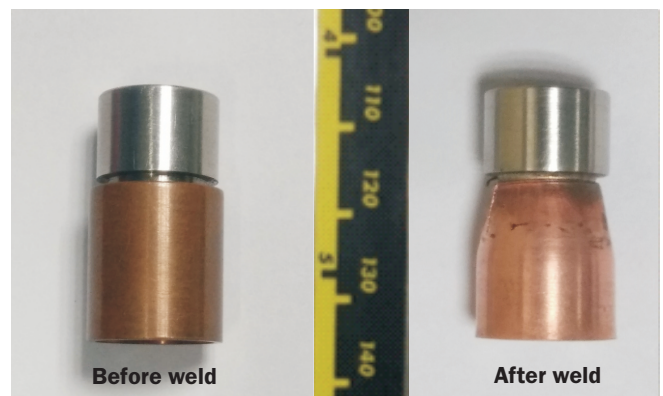
Fig.6: Copper driver & Ti-SS samples.

EDM cutting of welded sample   Cut section of welded sample
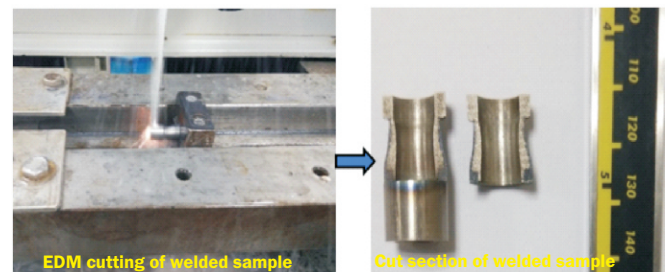
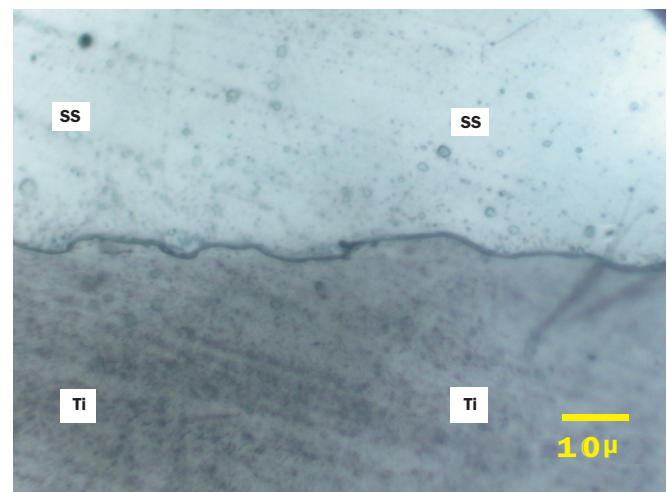*Fig.7: EDM wire cut of welded sample.*

SS   SS

Ti   Ti

10μ

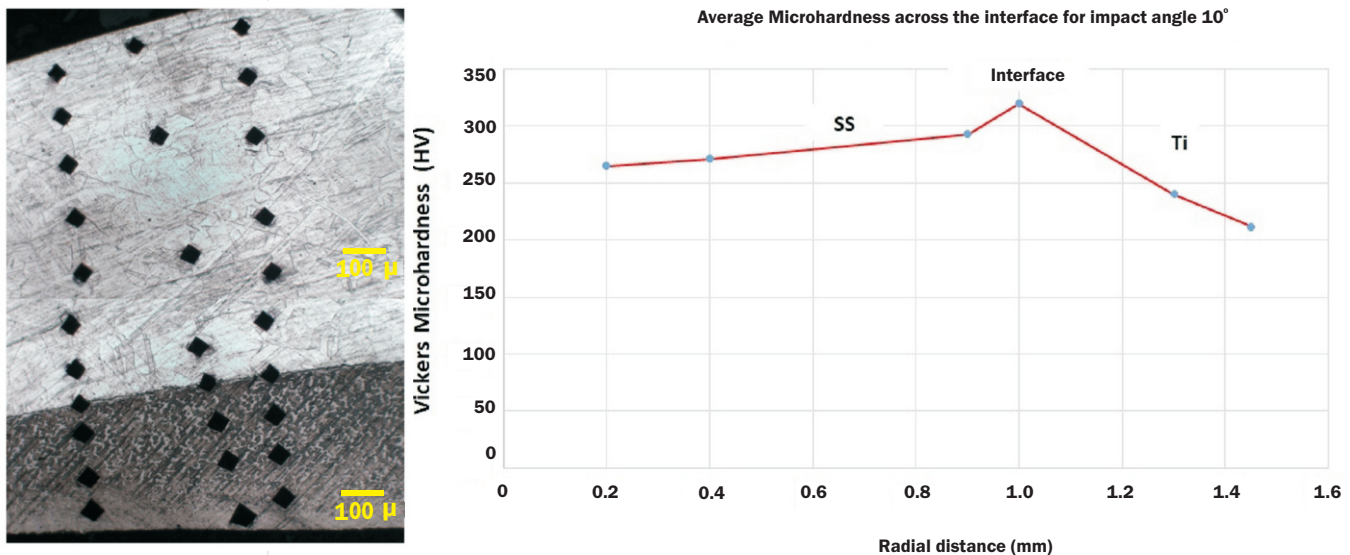*Fig.8: Ti-SS weld interface micrograph at 1000x for impact angle 10^0.*

Fig.9: Microhardness indentation and its graphical representation for weld sample with impact angle 10^0.

The copper driver from the welded sample, seen in Fig.6 is removed by dissolving in nitric acid. The sample is then checked for Helium leak rate to locate leaks if any using a Mass Spectrometer Leak Detector (MSLD) and a leak rate of the order of 10^{-12} mbarl/s is observed. For metallographic analysis the welded samples are cut along longitudinal section with Electric Discharge Machining (EDM) wire cut, as shown in Fig.7.

The sectionally cut samples are then moulded, polished and etched for studying the micrographs of the weld interface with an optical microscope at magnifications from 50x to 1000x, shown in Fig.8. It is observed that a joining of ~1.2 mm is established out of 6 mm active weld region available for impact, as shown in Fig.4, which corresponds to the numerically simulated impact velocity range of 250-350m/s. The joint established comprises of straight to wavy interface morphology as seen in Fig.8 comprising of few waves with maximum wavelength of ~20μm and amplitude of ~3μm. The reason behind the formation of waves along the interface is explained by the shock wave propagating through metals that generates periodic interferences along the interface giving rise to the Kelvin-Helmholtz instability creating interfacial waves.

Microhardness measurements are done over an array of points along and across the weld interface as shown in Fig.9. It is observed that the Vickers hardness varied from ~166HV to ~230HV at Ti tube, ~290 to ~330HV at the interface and ~156 to ~280HV at SS tube. The hardness values are observed to be relatively increasing towards the interface than Ti or SS side, being maximum at the interface. This represents the high strain rate plastic deformation introduced into the flyer and target tube during the welding process along the joint.

Conclusion

The application of MPW on 13.6mm diameter, 0.5mm thick Ti alloy tube to SS-304 tube has been successfully demonstrated with a tool coil comprising of 4-disc multi-turn coil and shaper assembly. From this study the following conclusions are drawn:

- The helium leak rate obtained in the order of 10^{-12} mbarl/s ensured that the joint established is leak proof.

- The straight to wavy pattern of interface observed is considered as an indication of a successful weld. Variation in interface morphology from straight to wavy

observed along the ~1.2mm joint length is correlated to the numerically simulated impact velocity i.e 250-350m/s.

- Variation of micro hardness across the weld interface, in the range of ~290 to ~330HV at the interface, indicates severe plastic deformation accompanying grain refinement on both sides of the joint.

Acknowledgments

References

[1] R. Natarajan and Baldev Raj, Fast Reactor Fuel Reprocessing Technology: Successes and Challenges, Energy Procedia, 2011, **7**, 414–420.

[2] Zhenzhen Yu, Sarah M Gilbert and Stephen Liu, Review of Ti to Steel Dissimilar Joining, Research & Development in Material Science, 2018, **5**(5), 507-509.

[3] J. S. Li , R.N. Raoelison , T. Sapanathan , Y. L. Hou , M. Rachik. Interface evolution during magnetic pulse welding under extremely high strain rate collision: mechanisms, thermomechanical kinetics and consequences, Acta Materialia, 2020, **195**, 404-415.

[4] S. Mishra, S. K. Sharma, S Kumar, K. Sagar and A. Shyam, 40 kJ Magnetic Pulse Welding System for Expansion Welding of Aluminum 6061 tube, Journal of Material Processing Technology, 2017, **240**, 168–175.

[5] Shanthala K, Sreenivasa T N, Choudhary Hitesh, Dond Shantharam, Sharma Archana. Analysical, numerical and experimental study on joining of aluminium tube to dissimilar steel rods by electromagnetic pulse force, 2018, **32**(4), 1725-1732.

[6] S. D. Kore, P. Dhanesh, S. V. Kulkarni, P. P. Date, Numerical Modeling of Electromagnetic Welding, 2010, **32**(1), 1-19.

[7] Makato Miyazaki, Kuniaki Sasaki and Masaki Okada, Influence of gap length on collision angle and collision point velocity of magnetic pressure seam welding, Mater. Sci. Forum, 2014, **767**, 166-170.
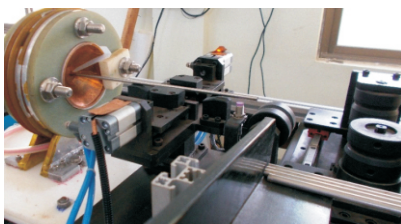
Special Purpose Machine

Automation of Magnetic Pulse Welding of PFBR Fuel and its End-Plug

Renu Rani[1]*, Surender Kumar Sharma[1], Nitin Waghmare[1], Shobhna Mishra[1], JMMVS Aravind[1], Rishi Verma[1] and Archana Sharma[1]
P. V. Suresh Verma[2], Nagendra Kumar[2], D. B. Sathe[2] and R. B. Bhatt[2]

[1]*Pulsed Power & Electromagnetics Division, Bhabha Atomic Research Centre, Visakhapatnam, Andhra Pradesh-531011, INDIA*
[2]*Advanced Fuel Fabrication Facility, Bhabha Atomic Research Centre, Tarapur, Maharashtra, INDIA*

Magnetic Pulse Welding Setup

ABSTRACT

Special Purpose Machine for Automation of Magnetic Pulse Welding (MPW) for top end- plug welding of Prototype Fast Breeder Reactor (PFBR) fuel pin inside glove-box is designed and developed. Simplification of the fuel fabrication operations and reduction of personal radiation exposure to a large amount of plutonium is one of the most important objective in the development pin welding automation system. As PFBR pin contain MOX Fuel (PuO$_2$ and UO$_2$), Biological half-life of plutonium is 200 years and specific activity of plutonium is 0.06 Ci/gm. Pin welding is one of the steps in fuel fabrication process which involves high radiation exposure to the setup operator. A remote-controlled automation system has been introduced for pin end plug welding. This system has been commissioned at BARC Tarapur.

KEYWORDS: *PFBR, Fuel Pin, End Plug, Electromagnetic Welding, Automation.*

Introduction

Fully automated and remote pin end plug welding system was conceptualized, designed and developed for magnetic pulse welding of fuel pin inside glove-box chamber to reduce personal radiation exposure during fabrication of mixed oxide (MOX) fuel containing about 20~30% of plutonium on the production scale of 3 tonnes of MOX fuel every year. The driver fuel of Prototype Fast Breeder Reactor (PFBR) is Uranium Plutonium Mixed Oxide ((U,Pu)O$_2$,MOX). MOX fuel pellets are loaded in SS-D9 clad tubes. Schematic diagram of the fuel pin are shown in Fig.1.

Fuel for the future core of Prototype fast breeder reactor will include plutonium re-processed from short cooled high burnup spent fuel. Fabrication of this fuel presently involves various activities resulting in high men-rem consumption by the operator owing to its high specific activity. The challenges are further compounded due to requirement of high production rate.

Fuel Fabrication Processes

The conventional powder metallurgy route, powder to pellet (POP), for fabrication of MOX fuel pellet involves mechanical milling, mixing of suitable binder and lubricant with UO$_2$ and PuO$_2$ powder, pre-compaction, granulation, final compaction, sintering and grinding as shown in the flow chart.

After pellet loading, fuel elements are welded. To automate this step, a special purpose machine is designed to weld fuel pin end plugs using magnetic pulse welding process.

Magnetic Pulse Welding

Magnetic Pulsed welding process is a solid-state welding process in which metallurgical bonding is affected by impacting metal or alloy parts against each other at high velocity by use of controlled high frequency and high intensity pulsed magnetic fields. This process is similar to the explosive welding process except that magnetic energy is used for impacting the parts together instead of explosive energy. Magnetic pulsed welding
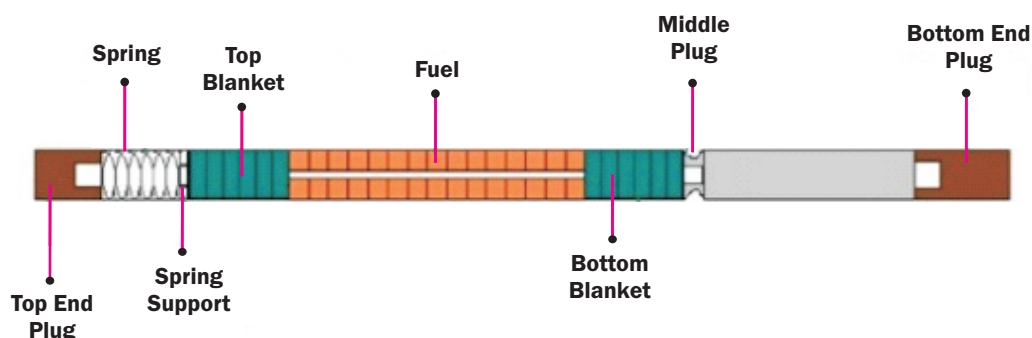

Fig.1: Schematic of PFBR fuel pin.

*Author for Correspondence: Renu Rani
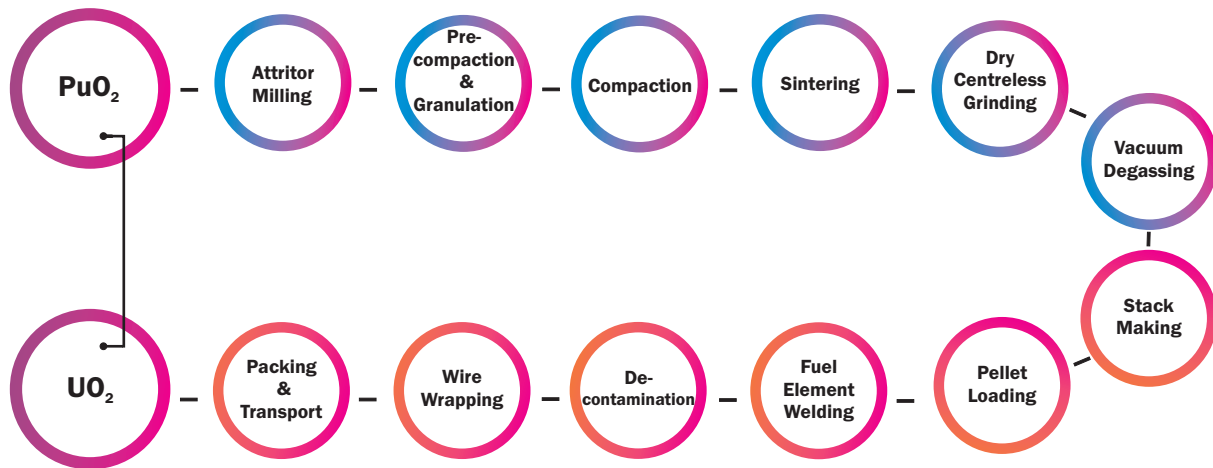E-mail: renusharma@barc.gov.in

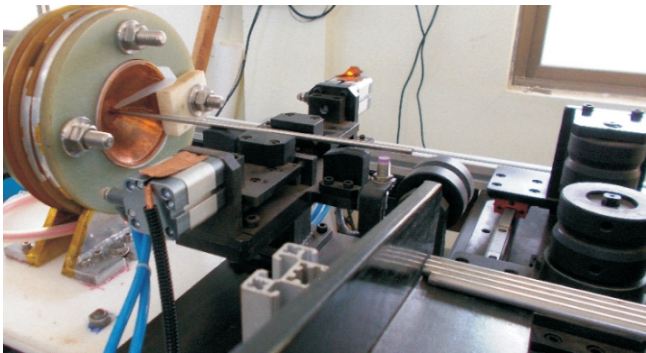Fig.2: Flow chart of PFBR fuel pin fabrication.

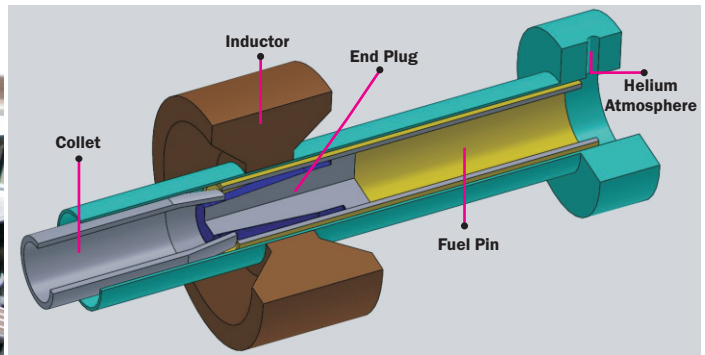Fig.3: Magnetic pulse welding setup.

Fig.4: Section view of PFBR pin inside EM coil in helium atmosphere.

process is readily applied to the welding of cylindrical plugs to small diameter tubes. Although breeder reactor fuel pin design may vary in size, the application described here consisted of cladding tubes approximately 6.6 mm in diameter and 2580 mm in length with a wall thickness of 0.45 mm. After the cladding tubes are filled with fuel pellets and associated metal hardware, tapered end plugs are inserted at the end of the tubes and welded. A typical setup for MPW is illustrated in Fig. 3 & Fig. 4.

The axial length of the welds depends upon the welding parameters selected. Usually, the parameters are adjusted to provide welds of 1.5 mm to 2.3 mm long. Since the welds are made at relatively low temperatures, there is no melting or heat affected zones.

Studies show an approximate 25% increase in the hardness of the weld zone over the original base material. Microscopic image of the weld interface between SS clad tube and end plug is shown in Fig. 5.

The advantages of the MPW process over conventional fusion welding process for end closure welds are listed below

More bond length

No melting or heat affected regions

No subsequent heat treatments required

Not sensitive to material history

Easier to weld dissimilar metals/alloys

Easier to weld crack susceptible metals/alloys

High production rate capability

Simple fixtures - no moving parts

Specialized operators not required

Automation System for Magnetic Pulse Welding Inside Glove-Box

The Automation System segregates of pins (press-fitted with end plug) from inclined tray, transfers them in the weld chamber, removes welded pins from the weld chamber and collects them in another glove-box.

During fuel fabrication process specified number of pins will be transferred by conveyor to inclined tray of automation system from pin loading glove-box. Pins will roll down by gravity on inclined tray. The automation system separates single pin from bunch of pins stacked on inclined tray, transfers pin to weld chamber, precisely holds the pin concentrically inside EM coil from both ends during the welding process, removes the welded pins from the chamber and finally collects them in collection tray of another Glove-Box for further processing.

Methodology

The developed automated end plug welding system can be divided in two parts, namely, the Mechanical part and Control part. The dimension of Mechanical system are fixed considering Glove-Box adaptability and application feasibility. Length of full automation system is 3500 mm to accommodate both PFBR pin (2580 mm long) and MPW coil. The width of the system is 1200 mm for enabling manual approach to system during maintenance as per Glove-Box design standards.
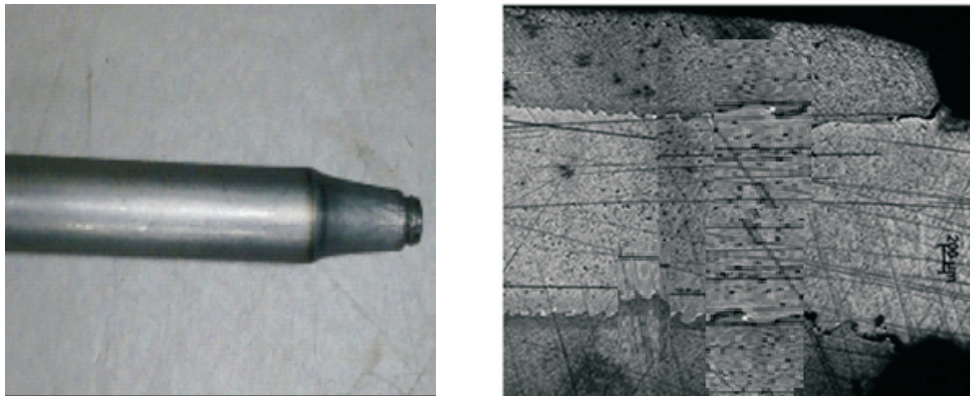
Fig.5: Welded fuel pin and microscopic image of weld interface.
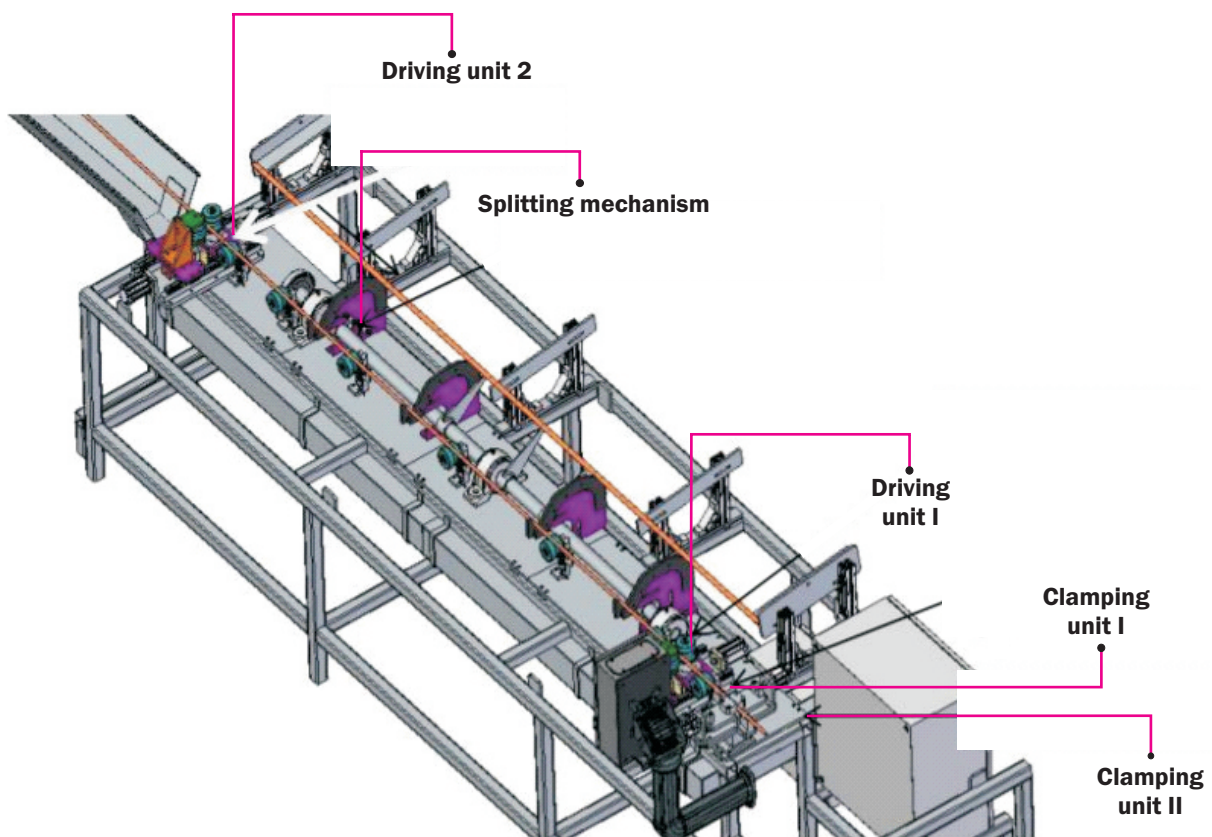
Fig.6: Pin welding automation system inside glove-box.

The mechanical part consists of six sub-assemblies

    Roller sub assembly

    Gripper sub assembly

    Splitting subassembly

    Pneumatic cylinders

    Servo system

    Guided ways and guided blocks

The control part consists of a motion controller, PC for operation control & monitoring, servo motors and sensor circuit. The end Plug welding system also has UPS system with battery backup for 30 minutes. The schematic of the system design is shown in the Fig.6

Sequence of Operation

The sequence of operation which gets repeated 50-60 times to weld one tray of pins, as tray contains 50-60 nos. of pins. Component runs over the sliding support plates by gravity.

Splitting mechanism separates the single pin from array of pins collecting on inclined tray. It carries one pin and place it over supporting rollers. Servo motor (RPM 20) provides the rotary motion to the shaft at which splitters are connected. Proximity sensors below Supporting rollers sense the position of pin.

When pin positioning is detected by proximity sensors, driving rollers grips the pin with pneumatic cylinders and starts carrying it towards the MP welding coil with servo motor. Proximity sensor is fitted next to driving rollers. This is referred

as zero and based on the distance given in the pre-program driving roller rotates continuously and pushes further forward towards the welding coil.

Gripper assembly before and after electromagnetic coil will hold the pin and end-plug during welding when pin is positioned inside the coil to ensure concentricity of pin and restrict movement during welding after taking shot on welding coil gripper assembly will open as time set in control unit.

Driving roller second assembly will rotate in reverse direction to remove pin from coil and carry it to exit bin that is in next in-line glove-box.

Conclusion

A fully automated fuel pin end-plug welding system with magnetic pulse welding has been developed for PFBR fuel pin. Developed system will significantly contribute to reduction in operator man-rem while harmonizing with high throughput rate and product quality required for PFBR fuel fabrication.

Salient Features of Operation

Pin will be rigidly fixed from both sides near welding Point because vibration can be generated during EMP welding as magnetic pulse welding is solid state impact welding.

Pin holder and its support is made up of completely insulated material as working is in high voltage environment.

Placement of job piece is carried out with high precision with tolerance of 0.1-0.2 mm in x-y-z direction inside the coil by servo motor and proximity centre.

Operational safety features incorporate for fail safe operation are UPS system with battery backup 20 min to ensure the safe completion of ongoing process in case of power failure.

In case of system idle condition sufficient space is provided near welding system for manual operation.
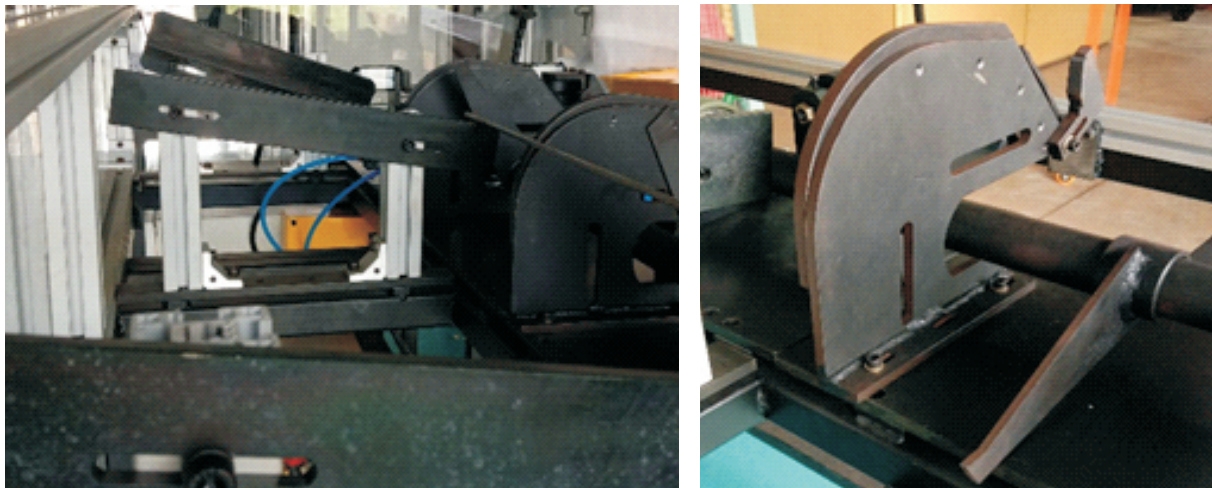

Fig.7: Inclined pin storage tray and pin splitting mechanism.

Fig.8: Driving rollers and supporting rollers.

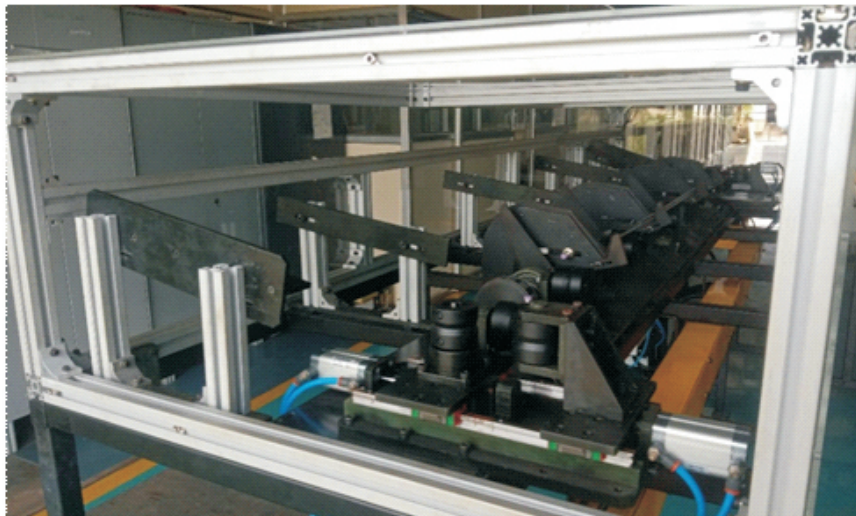*Fig.9: Gripper assembly and pin position during welding.*

Fig.10: Driving roller second assembly and system with glove-box with exit bin.

References

[1] H. S. Kamath, Recycle Fuel Fabrication for Closed Fuel Cycle in India, Energy Procedia, 2011, **7**, 110-119.

[2] The role of automation and humans in nuclear power plants, Report prepared within the framework of the International Working Group on Nuclear Power Plant Control and Instrumentation (IAEA-TECDOC-668).

[3] E. O. Adamov, P. A. Gavrilov, A. I. Gorelov, A. I. Efanov, M. N. MichaJlov, N. A. Sazonov, An automated data system for the monitoring of RBMK-1500 reactors: current status and potential (IAEA-CN-49/98), Vienna, 1988.

[4] Application of the pulsed magnetic welding process to nuclear breeder reactor fuel pin end closures, WILLIAM F. BROWN, IIEDL. HANFORD ENGINEERING DEVELOPMENT LABORATORY Operated by Westinghouse Hanford Company, a subsidiary of Westinghouse Electric Corporation, under the Department of Energy Contract No. DEACD5-76FF02170 P. O. Box 1970, Richland, Washington 99352.

[5] H. S. Kamath, Recycle Fuel Fabrication, Recycle fuel Fabrication in India, IAEA TM, Fukai, Japan (2008). Proceedings of a technical meeting (Characterization and Testing of Materials for Nuclear Reactors, May 29–2 June, 2006, Vienna), 2007.

[6] S. K. Sharma, Aravind JMMVS, S. Mishra, R. Rani, S. Mishra, N. Waghmare, Archana Sharma, Generation of 0.5 to 0.6 Mega Gauss Pulse Magnetic Field for Magnetic Pulse Welding of High Strength Alloys, 16th International Conference on Megagauss Magnetic Field Generation and Related Topics, 2018.

[7] P. S. Somyajulu, Rajashree Dixit. et al., Automated spacer wire wrapping system for PFBR Fuel element, BARC Newsletter, July- August 2018.
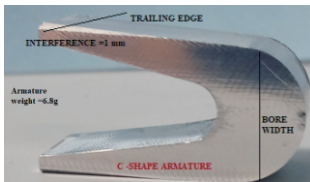
Ballistic Testing

Capacitor Driven Electromagnetic Railgun

Pankaj Deb[1]*, JMVVS Aravind[1], Rohit Shukla[1], Rishi Verma[1] and Archana Sharma[2]

[1]*Pulse Power & Electromagnetics Division, Bhabha Atomic Research Centre, Visakhapatnam-531011, INDIA*
[2]*Beam Technology Development Group, Bhabha Atomic Research Centre, Mumbai-400085, INDIA*

C-shaped armature

ABSTRACT

The article presents the experimental results of developed electromagnetic railgun including its design parameters. The 1.2 meter long rectangular bore railgun launches 6.8g aluminum armature at an exit velocity of 525ms^{-1}. The interference fit between rail and armature interface is selected 1mm. Further the impact of amor piercing shape projectile to defeat stainless steel plate is investigated by electromagnetic railgun system.

KEYWORDS: *PFBR, Fuel Pin, End Plug, Electromagnetic Welding, Automation.*

Introduction

Electromagnetic (EM) railgun is a device designed to launch a projectile with hypervelocity. Railgun is powered by some electrical energy source e.g. a capacitor bank. When the high current (100's kA) with a typical millisecond duration pulse is discharged into parallel conductor of rails, a magnetic field is established surrounding the rails. A conductive armature with a projectile allocated in front of it is placed between two rails. The projectile accelerates forward with JXB electromagnetic force acting on armature.

System Description

The capacitor bank consists of ten capacitors[1]. Each capacitor is rated for 178uF, 15kV DC are further connected in parallel configuration to increase the effective bank capacitance to 1.78mF. The 200kJ, 1.78mF capacitor bank is connected with high coulomb transfer Ignitron switch. The conventional railgun consists of two copper rails. The copper rails are inserted in the G-10/FR4 containment structure to provide the rail insulation. The spacing between the rails is defined as rail bore. Fig.1 represents the 14 x 13mm rectangular bore EM Railgun[2]. The muzzle velocity of

Table: 1

	Electromagnetic Railgun type	Conventional Railgun
1	Bore shape, Bore dimension	Rectangular bore, 14mm x 13mm
2	Railgun length, Inductance gradient (L')	1.2m, 0.3µH/m
3	Rail thickness, material	16 mm, Copper
4	Rail cross sectional area, insulator material	400 sq mm, Garolite (G-10) FR-4
5	Armature shape, material, weight	C-shape, Al 7075, 6.8 gm
6	Total weight of railgun	20 kg
7	Rail armature contact in rails	Metal armature contact

projectile depends upon the initial velocity, mass, inductance gradient, current, pulse duration[3,4]. The design parameter of the developed railgun is tabulated in Table 1.

The contact of the armature placed between rails play a significant role in rail lifetime and railgun efficiency[5]. Armature contacts with rail interface is improved by providing armature interference fit in the rail barrel[6,7]. The armature utilized in railgun experiment employing interference of 1mm from each side is shown in Fig.2.

Fig.3 shows the photographs of rails after shot utilizing 1mm interference fit armature. White aluminum deposit from the start point to muzzle end of rail signify that armature has moved in railbarrel with good contact. Erosion damage of rails is least when interference fit armatures are utilized. Fig.4 shows the oscilloscope trace of capacitor discharge current in rails.

Fig.1: Electromagnetic railgun.

*Author for Correspondence: Pankaj Deb
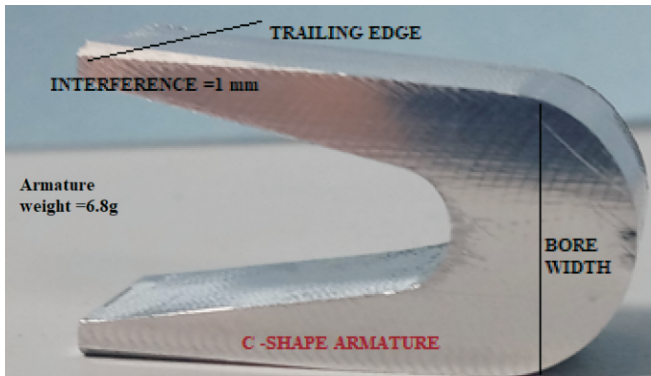*E-mail: pankajd@barc.gov.in*
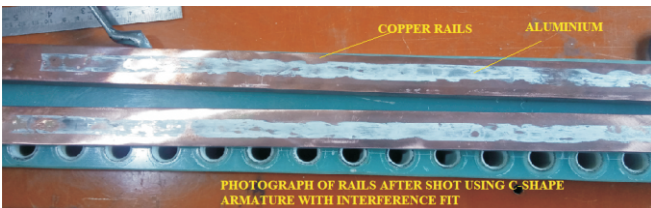
Fig.2:C-shaped armature.
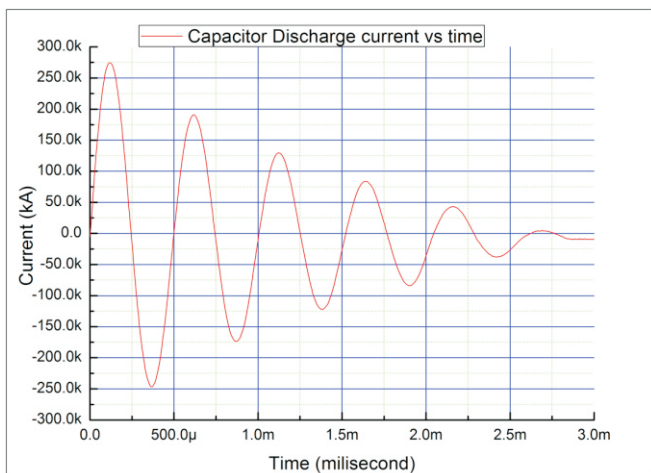

Fig.3: Copper rails after shot.

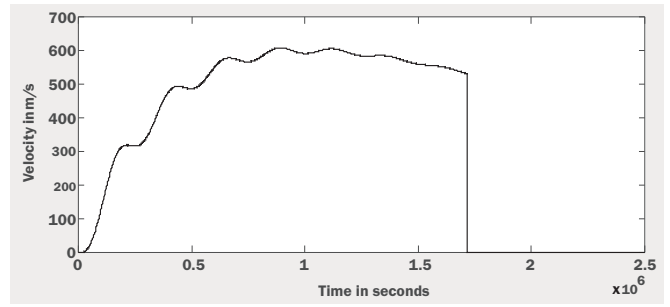Fig.4: Capacitor discharge current with time.

Fig.5:Profile of armature velocity.
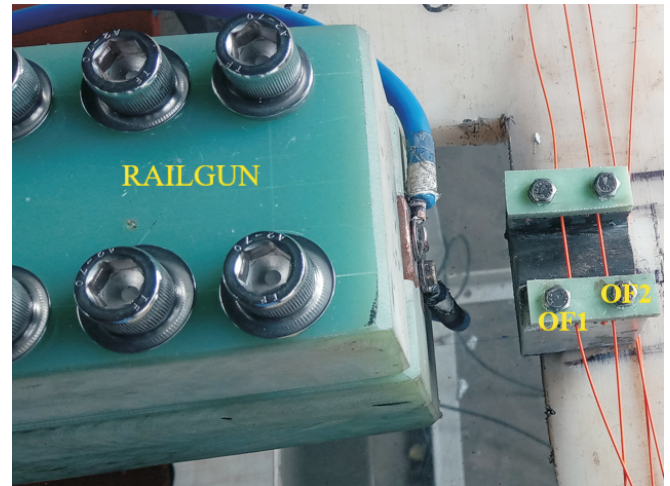
Fig.6: Muzzle velocity measurement setup.
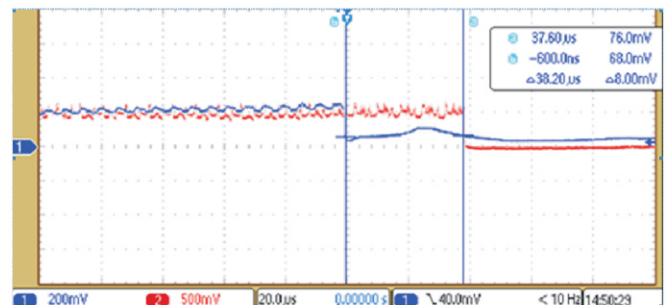
Fig.7: Optical fiber cut signal.

Simulation

The interpretation of armature velocity profile of mass 6.8g for discharge current illustrated in Fig.4 is analysed. The plot shows an estimated armature exit velocity 580m/s when it is placed at 850mm from muzzle end shown in Fig.5. The generalized equations for determining armature velocity is as follows.

$$Facc(t) = \frac{1}{2} * L^t * i(t)^2 \tag{1}$$

$$F(a_{fric}(t)) = \frac{2vA}{t} * vel(t) \tag{2}$$

$$Fnet(t) = F(acc)(t) - F(a_{fric}(t)) - F(ra_{fric}(t)) \tag{3}$$

$$Fnet = m * \frac{dVel}{dt} \tag{4}$$

$$Vel(t) = \frac{1}{m} * Fnet.dt \tag{5}$$

where $Facc$, $F(a_{fric})$, $F(ra_{friction})$, $Fnet$, Vel represents the electromagnetic force, friction force due to air coloumn inside rail bore, friction force due to rail armature interface, net force exerted on armature, armature velocity respectively. Friction drag due to rail armature contact, skin depth factors is not incorporated in this simulation. The oscillatory signature at each time interval of 0.25ms in the velocity profile implies that armature experiences pulsating acceleration. At such interval, the current remains zero. Decrement in armature velocity after 1ms, possibly due to larger frictional drag.

Experimental Results

Solid armature mass 6.8gm is accelerated at an velocity of 525m/s. The armature location prior shot is 850mm from muzzle end. The detailed experiment results is tabulated in Table 2. The muzzle velocity of armature during shot is measured by velocity measurement arrangement shown in Fig.6. Optical fiber F_o1 and F_o2 are positioned at 2cm apart at muzzle end of railgun. Laser light is transmitted through fiber F_o1 and F_o2. When armature hits the fiber, laser light is interrupted. The interruption timing of laser light results in information about exit velocity of projectile[8].

Table: 2

	Railgun detail	14x13 mm Rectangular bore, 1.2 m long
1	Capacitor bank detail	1.78mF, 200kJ
2	Peak Current, Energy, Total time period	275kA, 175kJ, 2.5ms
3	Armature weight, Muzzle Velocity	6.8gm, 525m/s
4	Diagnostic used for velocity measurement	Optical fiber cut

Fig.8: Projectile 316 SS with 7075 Al armature.

Fig.9: Impact on 304 SS plate.

The oscilloscope trace shows the time information of fiber cut and it is measured 38μs shown in Fig.7. In another shot, the impact of armor piercing shape projectile (Φ7.6mm-7.8mm) on 2mm thick 304 SS target is experimented. Projectile is made with 316 SS material weighing 5g. The combined weight of armature with projectile ~10g is used in this experiment, shown in Fig.8. The 2 mm thick 304 SS target is placed 0.5m away from the rail muzzle end to investigate the penetration information by projectile. The observed results of Fig.9 show that projectile is able to perforate the target by rail peak current 300kA, 2.5 millisecond duration, impact velocity 450-500m/s. This estimation is based on B-dot signals obtained inside the rail-barrel.

Conclusion

The results show that electromagnetic railgun could be used as a feasible driver to accelerate armour piercing shape projectile by non-explosive source in ballistic testing application.

Acknowledgements

References

[1] Jack S Bernardes, et al., Analysis of a capacitor based pulsed power system for driving Long Range Electromagnetic Guns, IEEE Transactions on Magnetics, 2003, **39**(1).

[2] T. C. Kaushik, et al., Performance of a 40 kJ, 60 cm long square bore railgun, High Pressure Research, doi 10.1080/08957959208225325.

[3] D Putley and C R Spikings, Power System Modelling for a Tactical Railgun demonstrator IEEE Transactions on Magnetics, 1991, **27**(1).

[4] Asghar Keshtkar, et al, Derivation of a formula for Inductance gradient using Intelligent Estimation method, doi 10.1109/ELT.2008.25, 14th symposium on Electromagnetic launch technology.

[5] John P. Barber and Charles L. McDonald A Comparison Of Armature Performance, IEEE Transactions on Magnetics, **22**(6), November 1986.

[6] Shengguo Xia, et al., Studies on Interference fit between Armature and rails in Railgun IEEE Transaction on Plasma Science, 2011, **39**(1).

[7] Deng Feng, et al., Investigations of the Armature–Rail Contact Pressure Distribution in a Railgun, IEEE transactions on plasma science, 2015, **43**(5).

Prototype Pulse Power Modulator

Development of Solid State Pulse Modulator for Biological Applications

Anil S. Nayak*, Rajasree Vijayan, Suvendu Mandal, V. S. Rawat and Jaya Mukherjee

Applied Spectroscopy and Diagnostics Section, Beam Technology Development Group
Bhabha Atomic Research Centre, Mumbai-400085, INDIA
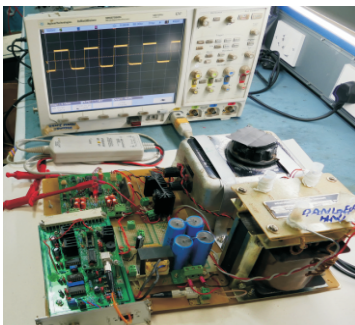
Pulse Modulator

ABSTRACT

Solid state pulse modulators have many industrial and scientific applications. The pulse modulator developed in our laboratory has flexibility in terms of the peak voltage (20V-2 kV), pulse repetition rates (DC-10 kHz) and duty cycle (0.1-100 %). The topology used enables reduced form factor of the system for low current drawing loads by modifying the solid state switch and capacitors. MOSFET and IGBT are used as the switches depending upon the application and load requirements. The fiber-optic cable integration ensures trigger source isolation. The driver circuit based on the M57962L operates as an isolation amplifier and provides required electrical isolation between input and output. The optical fiber integration ensures remote trigger control operation of the system. This pulse power supply developed has application in Electroporation and gene delivery of biological cells and tissues and food sterilization.

KEYWORDS: *MOSFET, Optical Fiber, HFBR, Transformer, Gate Driver.*

Introduction

Pulse modulator is an electronic circuit which provides high voltage pulsed power for many industrial and scientific applications. The advances in the device capabilities with respect to the switching speed and the power handling capacity has ensured the performance rivaling that of thyratron switched line-type modulators and hard tube modulators[1]. The new generation solid state switches have been developed with higher efficiencies and longer lifetime. The on-off timing sequence of solid state switches can be controlled by the low voltage and low power trigger circuit. There can be complete pulse width and duty cycle flexibility on a pulse-to-pulse basis. The MOSFETs and IGBTs have insulated gate thus requiring very low drive current thus eliminating the need for cascaded stages of bipolar junction transistors of low betas. Behrend *et al*[2] have described three pulse generator topologies namely a spark gap switched Blumlein, a spark gap switched coaxial cable and a solid state modulator, for developing electrical pulse less than 10ns rise time catering to the requirements of biological materials in culture. The transmission line based topologies have the advantage of higher voltages and faster rise times while the solid state modulators have the advantage of varying the pulse parameters namely the pulse width and the switching frequency. Kumar Gyanendra *et al*[3] have implemented the pulse generator based on the tesla transformer driven pulse forming line; in which the coaxial cable is used as the pulse compressor to generate the nanosecond duration pulse. The pulse generator providing the electric field of 18kV/cm, rise time of 25ns and repetition rate of 1.5Hz has been used to

expose the cancer cells in a 2mm electroporation cuvette. The different topologies of generating high voltage fast rise time pulses and the effects of nanosecond pulses in bioelectric experiments emphasize the importance of the electric field in the biomedical domain[4-6]. The rectangular high voltage pulses can also be generated using the flyback technique and the Bouncer modulator methods[7]. These methods are appropriate for low power levels. The topology used for development of pulse modulator provides flexibility in terms of peak voltage levels, repetition frequencies and duty cycle.

Schematic of Topology

Power circuit: The block diagram of the pulse modulator for delivering the rectangular flat top pulses to the load is shown below in the Fig.1. The Topology involves generation of high voltage DC and switching the energy stored in the filter capacitor (C) into the load through the solid state switch *viz.* MOSFET. The input voltage (V) is derived from the 230 V/50 Hz AC mains. In order to achieve voltage variation from 20V to 2kV, the AC main is fed to step up transformer T2 (230V/2.5kV) through autotransformer (T1). The auto transformer provides input voltage variation from 0-260V to the input of step up transformer.
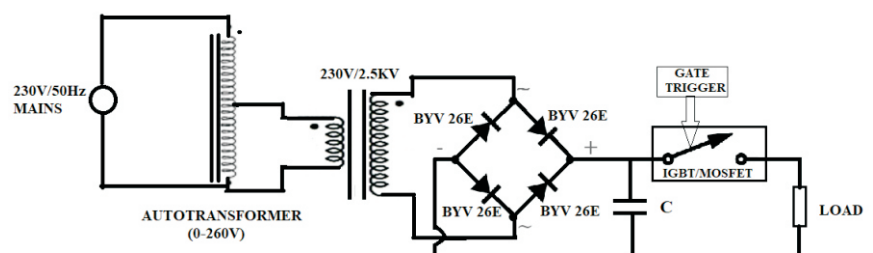

Fig.1: Schematic of the topology.

*Author for Correspondence: Anil S. Nayak
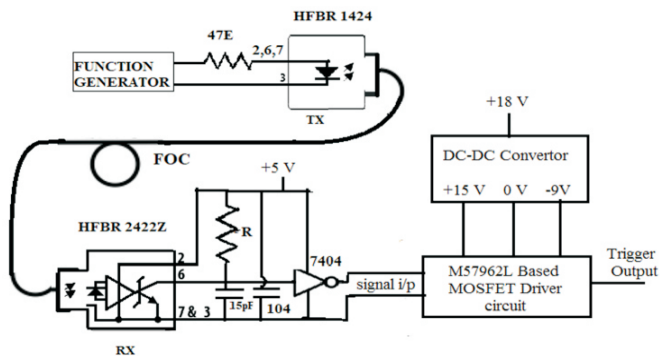*E-mail: anilsn@barc.gov.in*

Fig.2: Trigger circuit for solid state switch.

The core material used in the transformer (T2) is CRGO steel. The High voltage AC is converted to high voltage pulsating DC using a bridge rectifier with two BYV26E diodes (1kV PIV & 1A average current) in each arm of the bridge. The pulsating DC voltage is converted to smooth DC voltage by connecting a filter capacitor at the output of the bridge rectifier. This filter capacitor itself acts as the energy storage element. The capacitor was selected depending upon the current drawn by the load. Lower the capacitance value, higher will be the droop during the ON time of the pulse.

Trigger circuit for solid state switch: The trigger system has been designed in such a way that the system can be triggered using the external reference signal or can operate in the standalone mode. The standalone mode of operation is shown in Fig.2. The interconversion between the electrical and the optical signal takes place at the transmitter and the receiver end coupled by the Fiber optic cable. The signal generated at the receiver end is then used as the trigger signal to the driver circuit. The driver circuit is designed to provide the required drive current to turn on the MOSFET IXTH04N300P3HV. In the standalone mode, the timing signal is provided using the, Agilent make Function Generator AFG3052C. The 5V rectangular pulse signal at desired pulse repetition frequency and duty cycle is generated and fed to the HFBR transmitter circuit through a coaxial cable. In order to limit the current input to the HFBR, a 47Ω resistor is connected in series. The electrical pulses are converted to optical pulses and the output of HFBR is coupled with the fiber-opticlink. The optical fiber has FC connectorization at both ends. The 62.5/125µm fiber patch cord has a length of 2m. This optical isolation in between the two electrical circuits makes the system immune from the electromagnetic interference noise. The optical fiber integration ensures remote trigger control operation of the system in restricted areas. The optical signal received from the fiber is converted back to the electrical signal by HFBR 2422z. This IC has with inbuilt opto-transistor in open collector mode. A pull up resistance is connected to Vcc. The output TTL signal is obtained at the collector terminal is in the inverted form. This inverted signal is connected to the logic Inverter IC 7404. The input voltage to the driver circuit is +18 V.

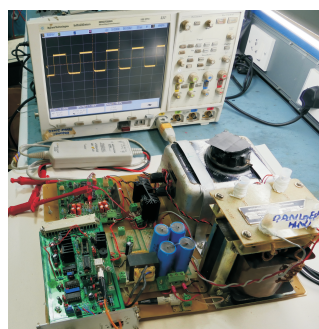Fig.3: Trigger circuit assembly.

Fig.4: Pulse Modulator.

The output of the optical to electrical receiver circuit is given to the Driver circuit. The driver IC M57962L is a hybrid integrated circuit designed for driving n-channel IGBTs and MOSFETs in any application. This device operates as an isolation amplifier for these modules and provides the required electrical isolation between the input and output with an opto-coupler. Short circuit protection is provided by a built-in desaturation detector. A fault signal is provided if the short circuit protection is activated. The drive current of 500mA is provided by the Driver IC at 50% duty cycle. This drive current capability of the driver IC is higher than the requirement of the IGBT and the MOSFET used. The driver PCB consists of the driver IC M57962L whose primary function is to drive the gate of the MOSFET. This IC requires a dual power supply. The input 18 V is converted to dual power supply of (+15 V) and (-9 V) using a dc-dc flyback convertor topology. The dc-dc converters provide isolated gate drive power. The gate drive power supplies are decoupled using the low impedance electrolytic capacitors. It is very important that these capacitors have low enough impedance and sufficient ripple current capability to provide the required high current gate drive pulses. The switching action provided by the MOSFET IRF530 enables the energy storage in the primary winding (when MOSFET is ON) and energy transfer in the secondary circuit (when MOSFET is OFF). The dot notation of the two secondary winding indicates complementary actions w.r.t ON and OFF times. IC 3844 drives IRF530 ON and OFF at frequency of 172kHz. The output from the Inverter IC 7404 of the receiver circuit is connected to input of the driver IC through a current limiting resistor. The hybrid gate driver amplifies the control input signal and produces high current gate drive at the output terminal. The gate drive current is adjusted by selecting the appropriate series gate resistance. The gate resistance will and normally be adjusted to provide suitable drive for the module being used considering dynamic performance, losses and switching noise. The photograph of the trigger circuit assembly is shown in Fig.3. The entire prototype is depicted in the Fig.4. The experiment was done by powering the trigger circuit and slowly varying the DC input to the energy storage capacitor. This variation was done using the auto-transformer connected to the input of the 230 V/ 2.5 kV transformer.

The final output voltage was measured across the load using the Differential probe: Agilent Technologies (N2790A) which can measure maximum of 1.4kV peak voltage in 500:1 attenuation setting. For measurement of higher voltages i.e. up to 2kV, the HV probe: Tektronix P6015A was used having 1000:1 attenuation setting. Fig.5 and Fig.6 depict the output voltage across the load obtained with variable voltages and duty cycles measured across 47kΩ resistive load.

Selection of Solid State Switch: The IGBTs and MOSFETs are the two solid state switches considered based upon their power handling capacities, switching frequencies, on state voltage drop and the miller capacitance between input and output. The IGBT has higher power handling capacity, lower switching frequency, slower rise and fall times, higher miller capacitance and lower on state voltage drop as compared to the MOSFET. In the switch used in the series configuration as in this topology, the entire load current flows through the switch, hence under higher load condition the voltage drop across the MOSFET becomes significant and impacts the output load voltage. When the resistive load was kept at 200Ω, the current drawn was high enough to reduce the voltage across the load to half of what could be achieved with IGBT as the switching element. The property of lower on state voltage drop makes IGBT the better option during the electroporation experiments in the cuvette where the equivalent load resistance in the
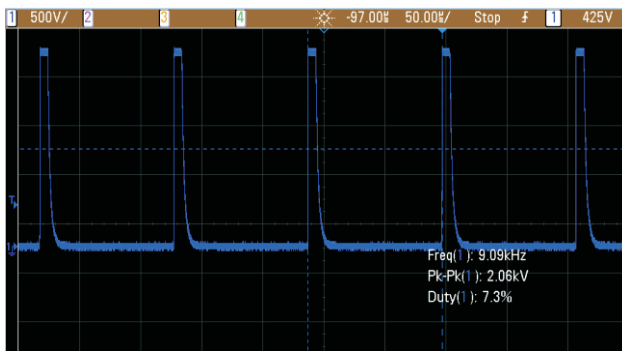
Fig.5: Output voltage of 2kV @ 7.3% duty cycle & 9kHz pulse repetition frequency.
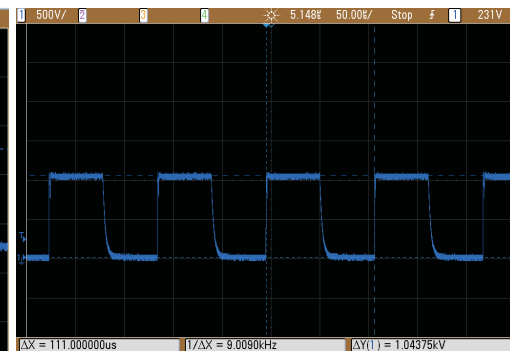

Fig.6: Output voltage of 1kV @ 50% duty cycle & 9kHz pulse repetition frequency.
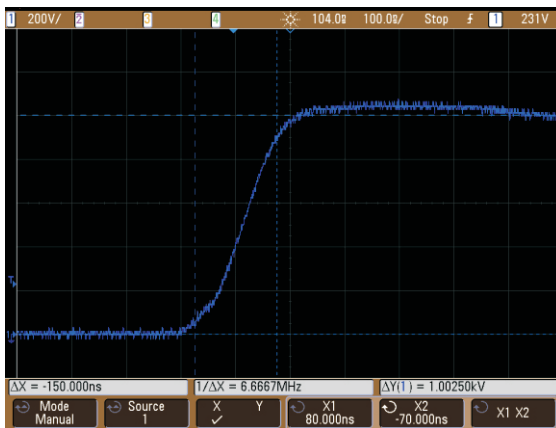

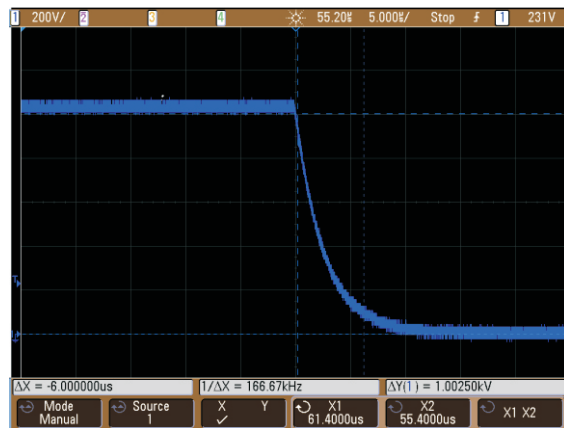Fig.7: Rise time of pulse with MOSFET.

Fig.8: Fall time of pulse with MOSFET.

range of 20-100Ω. On the other hand, when the current drawn by the load is in the mA range, the drop across the device is negligible; in that case the MOSFET provides the advantage of faster switching and faster rise and fall time due to lower miller capacitance compared to the IGBT. This feature of faster switching makes MOSFET a preferable device in the pulsed ion extraction from plasma. Fig.7 and Fig.8 show rise time and fall times of the pulse under 47kΩ load.

Since the current requirement is less, the switching device used to switch the capacitor voltage in to the load is MOSFET. IXTH04N300P3HV having voltage rating of 3kV, continuous current of 400mA and miller capacitance of 23 pF between drain and source. The rise time of the pulse across the load is 150nsecs as shown in the Fig.7. The fall time of the pulse is 6μsecs as shown in the Fig.8. The value is in close approximation of the calculated value; i.e. (5 x load resistance x miller capacitance value)   (5 x 23pF x 47kΩ)   5.4μsecs.

Conclusion

The working prototype of the pulse power supply has been developed with peak voltage of 1kV, pulse repetition rate of 9kHz and 50% duty cycle. The supply developed has the flexibility in terms of voltage variation up to 1kV, Duty cycle up to 50 percent and pulse repletion rate DC- 9kHz. The prototype can be used as a standalone system and also can be synchronized from the external trigger pulse. The external trigger pulse can be fed to the system through the optical fiber enabling remote operation. The incorporation of the optical fiber based trigger system ensures isolation between the incoming trigger system and the pulse power supply. This also ensures proper synchronization in the electromagnetic noisy environment. This pulse power supply developed, has application in effective Ion extraction of the isotopes in separation process, Electroporation and gene delivery of biological cells and tissues and food sterilization.

References

[1]   Cook, Edward, Review of Solid-State Modulators, 2000.

[2]   Matthew Behrend, Andras Kuthi, Xianyue Gu, P. Thomas Vernier, Laura Marcu, Cheryl M. Craft, Martin A. Gundersen, Pulse Generators for Pulsed Electric Field Exposure of Biological Cells and Tissues, IEEE Transactions on Dielectrics and Electrical Insulation, 2003, **10**(5), 820-825.

[3]   G. Kumar, S. Shelar, A. Patel, A. Roy, R. Sarathi, R. Singh, A. Sharma, Investigation of Effect of Nanosecond Pulsed Electric Field on MCF-7 Breast Cancer Cells, Journal of Drug Delivery and Therapeutics, 2021, **11**(3), 43-49.

[4]   M. Kenaan, El Amari S, A. Silve, C. Merla, L. M. Mir , V. Couderc, P. Leveque, Characterization of a 50-Ω exposure setup for high-voltage nanosecond pulsed electric field bioexperiments. IEEE transactions on biomedical engineering, 2010, **58**(1), 207-214.

[5]   Kolb, F. Juergen, Susumu Kono, Karl H. Schoenbach, Nanosecond pulsed electric field generators for the study of subcellular effects, Bioelectromagnetics, 2006, **27**(3), 172-187.

[6]   K. H. Schoenbach, R. P. Joshi, J. F. Kolb, N. Chen, M. Stacey, P. F. Blackmore, S. J. Beebe, Ultrashort electrical pulses open a new gateway into biological cells, Proceedings of the IEEE, 2004, **92**(7), 1122-1137.

[7]   Shrivastava, Purushottam & Mulchandani, J. & Sahni, Vinod, Development of all solid state bouncer compensated long pulse modulators for LEP 1MW Klystrons to be used for LINAC4 project at CERN, 2008.

FEATURE ARTICLES

10 kW Electron Beam Melter

Electron Beam
Thermal Applications

M. N. Jha, E. Kandaswamy, P. Malik, S. Gupta and B. Prakash

Electron Beam (EB) Welding and Melting has become an indispensable tool for processing of nuclear and accelerator grade materials. Over the years, it has gained leverage in aerospace and automobile industries too. Processing of materials through EB route is usually done in high vacuum conditions, which makes it ideal for welding and melting of various refractory and reactive materials, including Tantalum, Tungsten, Molybdenum, Zirconium, Titanium, Niobium and Uranium.

In EB thermal processing, high intensity electron beams (beam power density in the range of 10^4-10^6 W/cm^2) are employed as heat source. BARC has been developing high power EB Welding and EB Melting Machines in-house for nuclear applications.

The authors are from Electron Beam & Pulse Power Machine Section, APPD, Beam Technology Development Group, BARC.

Technology Innovations

EB Welding
EB Melting
Vacuum Melting
and
Refinement

Besides, the Indian industry is embracing this highly sophisticated and user-friendly technology in diversified areas.
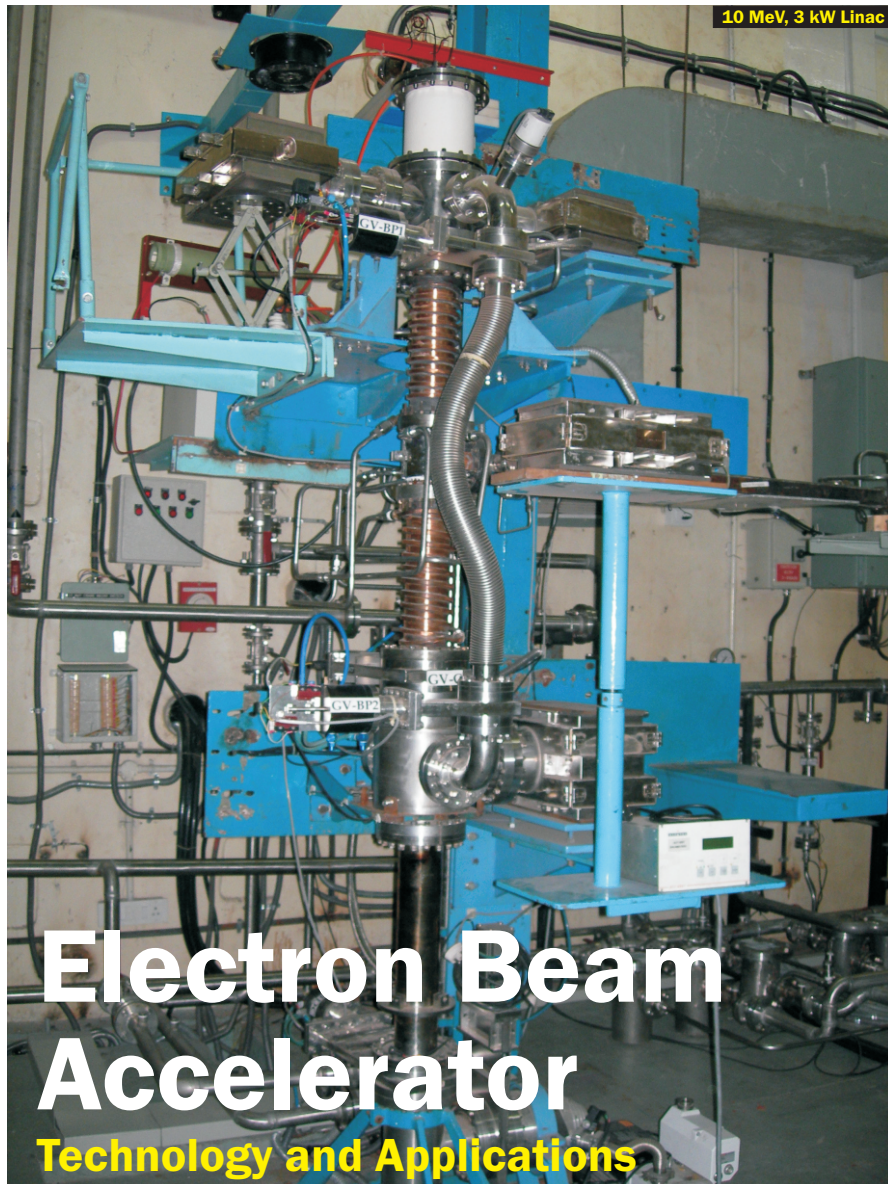
EB Welding machines of power rating ranging 2 kW-12 kW are being developed in-house for deployment in various operations of BARC, Mumbai. A 12 kW EB Welding Machine has been installed at the Old Training School Building here for promoting the use of this technology within the constituent units of the Department of Atomic Energy (DAE). A 12 kW EB Welding machine had been installed at Steel Technology Centre, Department of Metallurgical and Materials Engineering, IIT Kharagpur, for EB Welding of materials. BARC is currently working on the development of a 20 kW EB Welding machine, which would cater to the potential needs of Indian industry.

EB Melting Machines of power rating ranging from 6 kW to 15 kW have also been developed in BARC for metallurgical studies on metals and alloys. A 10 kW, 15 kV EB Melting machine has been commissioned for preparation of new refractory alloys by Materials Science Division. Buttons (metal-based) of 25 mm diameter x 12 mm thickness and fingers of 40 mm x 25 mm x 12 mm dimensions can be easily prepared using this machine, which is equipped with a unique facility of online charge feeder system for vacuum drip melting and production of 40 mm diameter x 250 mm long ingots. A 40 kW, 25 kV EB Melting machine is also being developed for obtaining larger ingots (65 mm diameter x 500 mm long).

A 120 kW, 40 kV high power EB Melting gun column has been developed in BARC for Melting Furnace. Two electron guns were deployed in 300 kW EB Melting Furnace jointly with Nuclear Fuel Complex, which has deployed the system for development of new alloys and consolidation of metal scrap. Thus, the Beam Technology Development Group of BARC has acquired significant capabilities in this niche area .We welcome DAE fraternity to support and also embrace this high-end technology in their field of specialization.

10 MeV, 3 kW Linac

Gemstone Coloration using 10 MeV Linac

Dual Energy Linac Assembly

Electron Beam Treatment of Onion

Electron Beam Accelerator
Technology and Applications

Electron Beam Centre (EBC) Kharghar, Navi Mumbai

The program for development of industrial electron accelerators in-house had been initiated in BARC in the early 1990s. The prime motivation for this initiative was to provide impetus to the R&D activities with an aim to widen the scope of basic research program in BARC. The maiden in-house developed Cockroft-Walton accelerator of 500 keV capacity was commissioned by BARC at BRIT, Vashi, Navi Mumbai, in 1998.

Subsequently, BARC has established a dedicated facility - Electron Beam Centre (EBC) at Kharghar, Navi Mumbai, to pursue the development of high energy electron accelerators more vigorously and to broaden their industrial applications. Over the years since its establishment, EBC has developed several accelerators to fuel multi-sectoral applications.

10 MeV, 3 kW LINAC

The LINAC has a vertical configuration and has applications in multiple domains, including semiconductors, gemstone coloration, polymers and bio-stimulators .

1 MeV DC Accelerator

The 1 MeV DC accelerator functions on symmetric Cockroft Walton principle. It was qualified for ruggedness by running the system continuously for 24 hours. The system is operated at 50 kW beam power and experiments on utilizing it for waste water treatment is currently in progress.

6 MeV Single Energy and 6/4 MeV Dual Energy Accelerators for Security

The Electron Beam Centre has expanded the scope of electron accelerator program to meet the requirements of national security, especially in the area of cargo scanning applications to address the movement of contraband objects. For this purpose, a compact 6 MeV RF electron Linac has been designed, which has successfully demonstrated its utility by generating high resolution images of large cargoes. The unit has been validated for radiography of bulk metallic structures, and it meets the ANSI standards of imaging and IEC 62523 norms for material contrast.

Electron Beam Treatment of Wastewater

In pursuit of objectives of National "Clean Ganga Mission" initiative

P. C. Saroj and DC Accelerator Team of EBC Kharghar

Electron Beam Accelerator Technology has potential applications in the treatment of effluents discharged from textile and tanning industry, municipal sewage and wastewater from hospitals among others. These industries are increasingly finding it difficult to limit the level of impurities in the effluent water to the permissible levels notified by the Central Pollution Control Board (CPCB), Govt. of India. However, in the long term, this issue could be addressed through adoption of EB accelerator technology.

When electron beam is incident on effluent water, it leads to radiolysis coupled with copious production of aqueous electrons, hydrogen and hydroxyl radicals.

$$H_2O \xrightarrow{EB} e_{aq}^-, H\star, OH\star, HO_2\star, H_2O_2, H_2$$
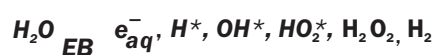
These species react vigorously with the constituents of dye in the effluent water to break the complex molecules. As a result, they become more amenable to decomposition by the bacteria. In comparison to conventional microbial and chemical treatments methods, complete oxidation of non-biodegradable matter can be achieved through Electron Beam (EB) within milliseconds.

More importantly, the technology is considered to be user-friendly as well as safe to the environment. The technology was successfully demonstrated (ready for technology transfer and industrial incubation) by treating wastewater using simulated dye effluent wherein a significant reduction of chromaticity, COD and BOD levels have been achieved by applying radiation dose in the range of 5-16 kGy. The basic components of the system include a wastewater feeding system comprising a pump, through which effluent water from the aeration tank of the Effluent treatment Plant (ETP) is supplied to the front side of the beam exit port where the high energy electrons are bombarded from the EB machine. The effluent is circulated through a piping system to the aeration tank till the requisite

1 MeV DC Accelerator

Chemical Oxygen Demand [COD] (250ppm) and Biochemical Oxygen Demand [BOD] (30ppm) values are obtained. Finally, the treated water is discharged through the nozzle in the form of a water film of 4 mm thickness and 1500 mm width.

The authors are from APPD and Electron Beam Centre, Kharghar, which are part of Beam Technology Development Group, BARC.

Air Plasma Incinerator
===

In Pursuit of 'Clean India Mission'

S. Ghorui, S. Bhandari, N. Tiwari, V.C. Misra and Y. Chakravarthy

Thermal plasma torches have important applications in the management of municipal solid wastes (MSWs) and hazardous wastes, liquid, electronic and nuclear wastes. Energy intensiveness, which is considered to be a lagging aspect of the technology, has been addressed through development of a medium power (30 kW) hafnium electrode air plasma torch in BARC. With the help of the newly developed technology, a unique Air Plasma Gasifier/Incinerator technology has been developed by BARC (ready for technology transfer to industry), which adopts a combination of high temperature gasification and a controlled burning of syn-gas for carrying out incineration. The technology significantly minimizes the requirement of energy supply from external sources. Further, it can process waste in the order of 1-3 ton per day, which is dependent on the type of waste fed into the system.

At low operating temperatures, incineration may become a potential source for highly carcinogenic compounds, including dioxin, furan, other pollutants in this category and also ash. By virtue of extremely high operating temperature, the incinerator system of BARC leaves little or no scope for release of such harmful compounds as well as their residues into the environment.

The basic components of the unit comprises a waste feeder unit, primary chamber, torch system, secondary chamber, venturi scrubber, a packed bed column, ID fan unit and a stack.

The authors are from Thermal Plasma Technologies Section, Laser & Plasma Technology Division, BTDG, BARC

The waste identified for incineration is fed from the side portion located near the head of the primary chamber. The ID fan unit maintains a negative pressure throughout the process zone and does not permit any synthesized gas to escape from the process chamber.

The three air plasma torches of the incinerator system, which are azimuthally oriented 120° apart, discharge inside a coke bed located at the bottom of the primary chamber to create a uniform high temperature (>1500°C) process bed. The fed waste drops from the hopper on the top and eventually reaches the bottom hot bed of the primary chamber via mechanically interlocked compartments. During this process, the waste gets gasified, processed and is finally released into the environment as a benign gas. Nearly 1.5 ton waste was mitigated during the 'Swachhata Week 2022' organized in BARC. The system can be operated in both incineration as well as in gasification mode. Under incineration mode, emitted gases such as CO, SO_x, NO_x were found to be well within the permissible limit prescribed by the Central Pollution Control Board, Govt. of India. The syn-gas generation mode in the system gets activated soon after the entire external air inlet ports are closed. The obtained syn-gas (total of CH_4, CO and H_2) quality meets the energy content of more than 6.3 MJ/Nm^3. Two such systems have been installed in BARC.

6 MeV X-Band Linac

6 MeV X-Band Linac
NDT & Medical Applications

J. Mondal, L. Mishra, S. G. Sarkar, V. Sharma, V. Kaushik, R. Kalra,
N. Chaudhary, E. Kandaswamy, R. I. Bakhtsingh and Archana Sharma

Xband low energy accelerators are compact in size, light weight, which make them highly superior over S and C band Linacs, with applications in medical radiation therapy/non destructive testing. BARC has developed a 9300 MHz, 6 MeV, 0.48 kW standing wave type X-Band Linac (XBL) cavity based x-ray source. The X-Band Linac based x-ray source has been assembled with primary collimator and dose measurement setup at a distance of 1 m from the source. The 6 MeV XBL comprises an on-axis coupled cavity configuration with 49 cells to it(25 accelerating and 24 coupling cells). The Linac is operated in the pulsed mode with a pulse width of 3-4 µs at 200 Hz repetition rate. An indirectly heated thermionic dispenser cathode based electron gun produces pulsed electron beam, which is then injected into the Linac cavity at 20-25 keV energy. The XBL is fed with RF power from a magnetron based power source at 9300±10 MHz to generate an accelerating electric field gradient of approximately 18.5 MV/m in vacuum of 1×10^{-6} mbar or higher. Post acceleration, the 6 MeV electron beam is focused to less than 2 mm diameter with the help of a permanent focusing magnet. The focused beam falls on a water-cooled Tungsten target to produce x-rays of 600 cGy/min at a distance of 0.8 m from the target at 200 Hz. This x-ray beam is then collimated with a 12.7° conical collimator to obtain a circular x-ray beam of diameter of

around 97 mm at the exit of the collimator. PLC-based control and interlock (Control & Instrumentation) system of the Linac based x-ray source has been implemented for fail-safe operation. In the event of any interlock failure, both the primary electron beam and RF source power are switched OFF to maintain the integrity of the system.

The authors are from Accelerator & Pulse Power Division,
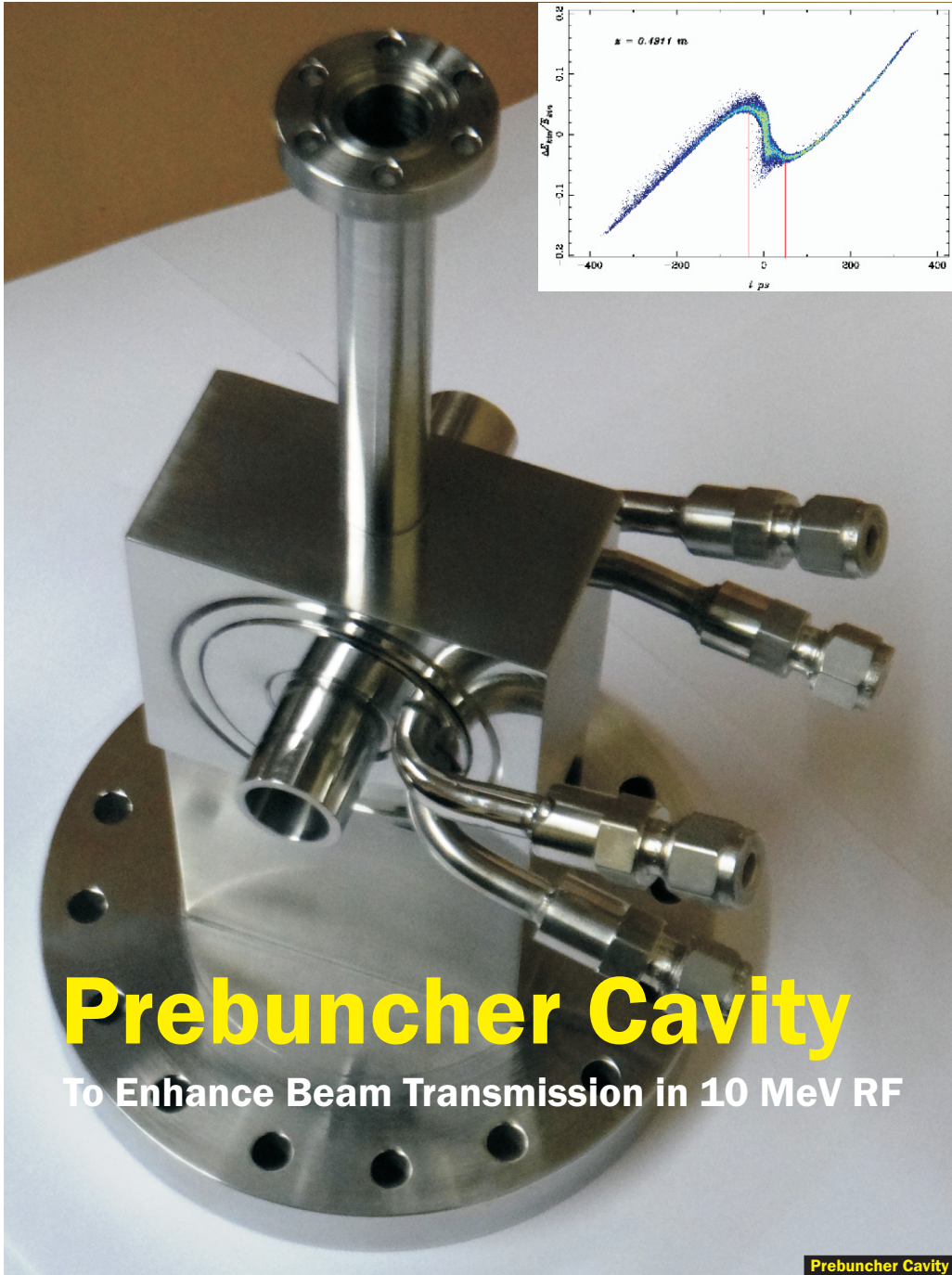Laser & Plasma Technology Division and Electron Beam Centre of Beam Technology Development Group, BARC.

Applications

Inter-Operative Radiation Therapy

Stereotactic Radiosurgery

Non Destructive Testing of materials and industrial components

Prebuncher Cavity
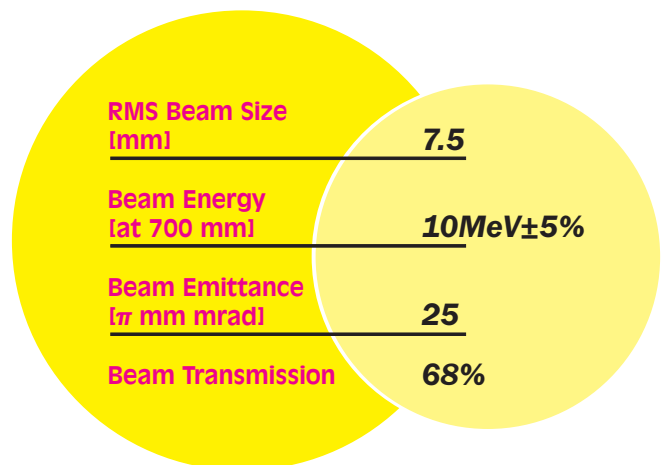To Enhance Beam Transmission in 10 MeV RF

Prebuncher Cavity

machine in horizontal configuration at EBC, Kharghar. In the existing configuration of 10 MeV, 3 kW Linac, the electron beam from a LaB_6 cathode based thermionic electron gun (40–50 KeV) is directly injected into the 0.9 m long Linac cavity structure to achieve the final energy. A maximum beam transmission efficiency in the range of 20%–25% has been achieved.

In order to improve the beam transmission efficiency to 60% in the new horizontal Linac (10 MeV, 5 kW), a pre-buncher (PB) cavity along with low energy beam transport (LEBT) line has been introduced. Introduction of small energy modulation of the injected DC electron beam in PB cavity will ensure longitudinal bunching in the DC beam after traveling a certain drift distance from the PB cavity. This bunched electron beam, when injected into the main Linac will be able to capture electrons more efficiently, which will essentially result in higher beam transmission. The fabricated Prebuncher cavity is displayed predominantly in this article. The simulated output beam parameters of the 10 MeV Linac beam line with Prebuncher are presented in the infographic given below.

J. Mondal, L. Mishra, S. G. Sarkar, Shiv Chandan,
R. I. Bakhtsingh and Archana Sharma

Electron Beam accelerators of up to 10 MeV energy have several industrial applications, including food irradiation, medical sterilization, cross linking of polymers for agriculture, cable and tyre based industries, semiconductor characteristics modifications, electronic waste management, radiation hardening studies etc. In EBC, Kharghar, a 10 MeV, 3 kW RF electron Linac is in operation, which works in both electron beam and X-ray modes. To enhance the throughput of industrial applications, a higher beam power machine in the range of 5–10 kW is desirable. In view of this, it is being planned to develop a 10 MeV, 5 kW

RMS Beam Size [mm]	7.5
Beam Energy [at 700 mm]	10MeV±5%
Beam Emittance [π mm mrad]	25
Beam Transmission	68%

S band relativistic backward wave oscillator with COBRA Lens

Four Pin FXR Tube

Four Channel Marx Generator with FXR Tubes

Microwave and X-Rays

Amitava Roy

X-band IEMI system with Compact Marx generator

Intentional Electromagnetic Interference (IEMI) Generator

A pulsed 1 Gigawatt peak power microwave source in S band, based on a relativistic backward wave oscillator (RBWO) has been designed and operated in BARC. The microwave source has been operated using KALI 30 GW pulsed power system at 600 kV beam voltage and 6.5 kA beam current to produce 1.2 GW peak microwave power at 3.28 GHz at a guiding magnetic field of 0.6 T. As part of IEMI studies, APPD, BARC has developed a RBWO based compact Marx generator driven microwave system, which is capable of producing 1000 MW peak microwave power at 9.22 GHz (X-band) frequency. The system consists of a Coaxial 20 Stage Marx Generator capable of producing a 600 kV, 7 kA pulsed electron beam for 60 ns (FWHM) duration. A pulsed magnetic field of 3 Tesla has been used to guide the electron beam inside the RBWO cavity. A serpentine mode converter transforms the mode of operation from TM01 to TE11 to provide maximum electron field in the

The author is from Accelerator & Pulse Power Division, Beam Technology Development Group, BARC.

direction of the bore site. The electron beam diode is evacuated with a TMP which is backed by a rotary pump to 1×10^{-5} mbar vacuum level. The IEMI is radiated through a Conical Horn antenna of 21 dB gain. Presently, work is underway to make the system more robust by using a 0.74 T permanent magnet system.

Four Channel Flash X-ray System for Dynamic Radiography

A four channel Flash X-ray (FXR) system has been designed and developed for dynamic radiography. The system is capable of generating 4 FXR pulses within a time interval that can be varied between 1 microsecond and 1 ms, and synchronized to capture dynamic events of microsecond time scale. By virtue of its portable design, the FXR tube head can be carried to the test site with a greater ease. The cumulative dose measured at 1 m distance from the X-ray tube window was 25 mR. A penetration depth of 18 mm in stainless steel at 2.5 m distance was achieved. The system has been installed at VSSC, Trivandrum and dynamic radiography of detonator firing event was radiographed with good resolution.
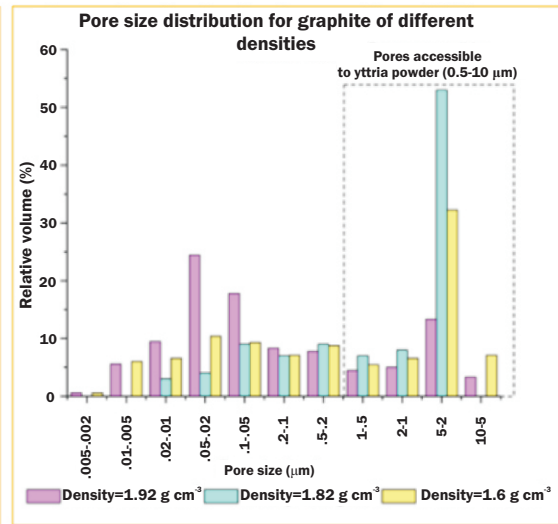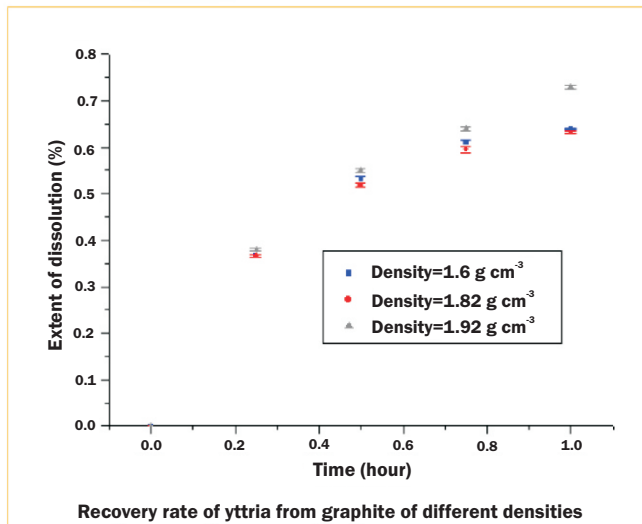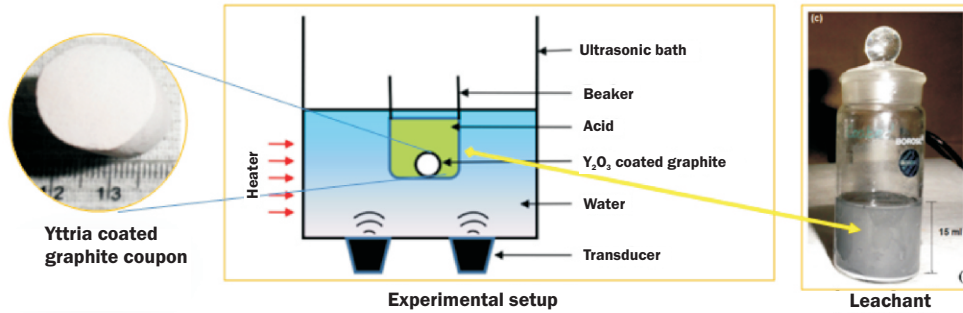
RESEARCH
SYNOPSES

Cavitation-assisted Decontamination of Yttria from Graphite of Different Densities

Yttria coated graphite coupon

Experimental setup

Leachant

Recovery rate of yttria from graphite of different densities

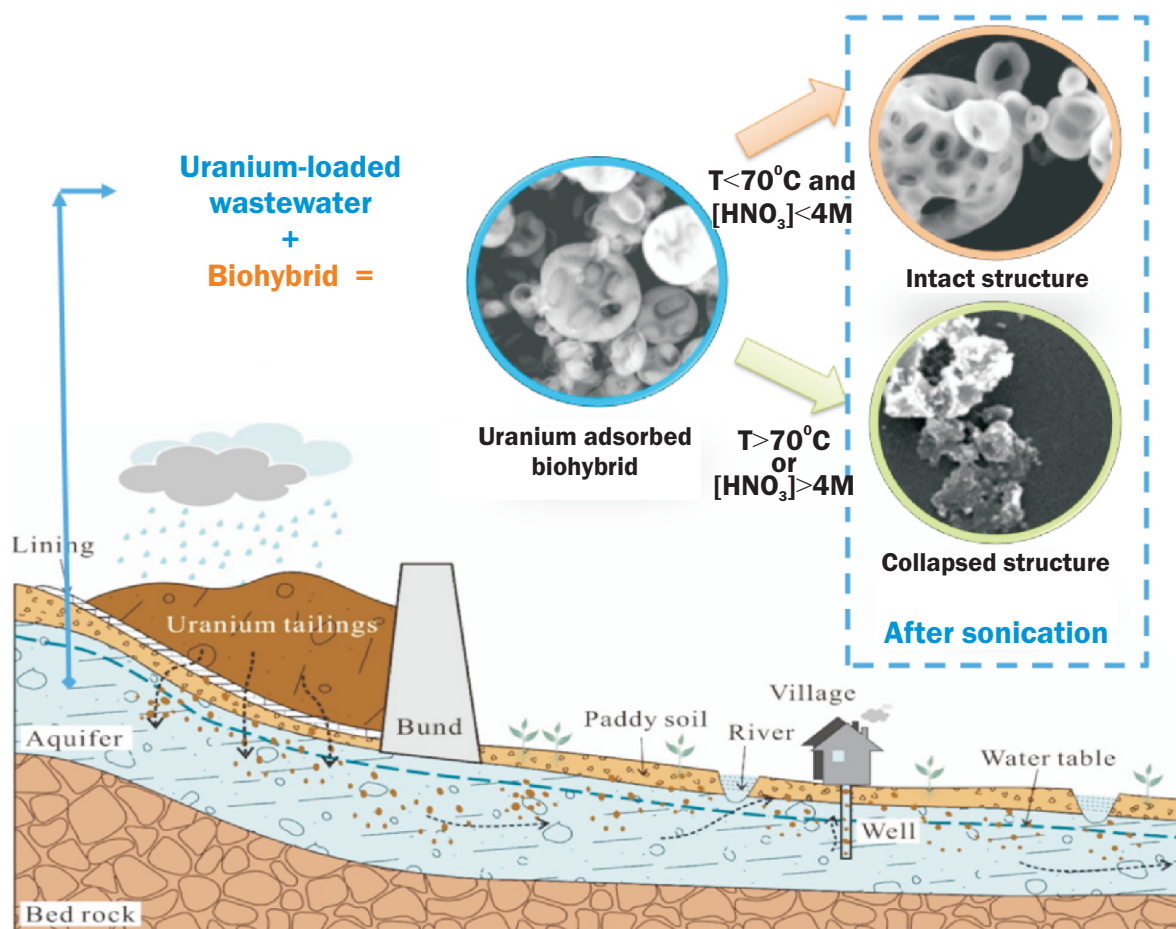Pore size distribution for graphite of different densities

*S. Lahiri, D. Mandal, P. R. Gogate, A. Ghosh, and R. L. Bhardwaj

Process intensification using ultrasound for yttria coated graphite substrates is established.

High-density graphite (HDG) is widely used as crucibles and substrates to handle molten refractory nuclear materials viz., uranium and plutonium. It is susceptible to oxidation in atmosphere at temperatures above 500^0C, but stable at temperatures around 3000^0C in high vacuum. A protective coating on graphite prevents the unwanted chemical interaction between molten metal and carbon, and thus ensures high corrosion resistance and longer service life at the desired operating temperature. The coating also prevents deposition of molten metal on the porous surface. Yttria (Y_2O_3) is widely used as a high temperature coating material on the graphite for nuclear applications. A recent article (Lahiri *et al.*, *'Cavitation-assisted decontamination of yttria from graphite of different densities'*, Ultrasonic Sonochemistry, 2021, **75**, 105520) investigated intensified dissolution of yttria from the coated graphite samples using ultrasound as a non-destructive decontamination technique to recycle the graphite substrate. The parametric study and kinetics of the process was established. Effect of adding oxidant on the kinetics was also studied along with the influence of pore size distribution for graphite of different densities. The outcome of the work is important as this will not only bring down the volume of graphite wastes generated by the nuclear installations, but also to bring down the radiological exposures and environmental pollution caused by its burning.

**Laser & Plasma Technology Division
Beam Technology Development Group
Bhabha Atomic Research Centre
Mumbai- 400085, India*

Sonochemical Recovery of Uranium from Nanosilica-based Sorbent and its Biohybrid

Uranium-loaded
wastewater
+
Biohybrid =

Uranium adsorbed
biohybrid

$T<70^{0}C$ and
$[HNO_3]<4M$

Intact structure

$T>70^{0}C$
or
$[HNO_3]>4M$

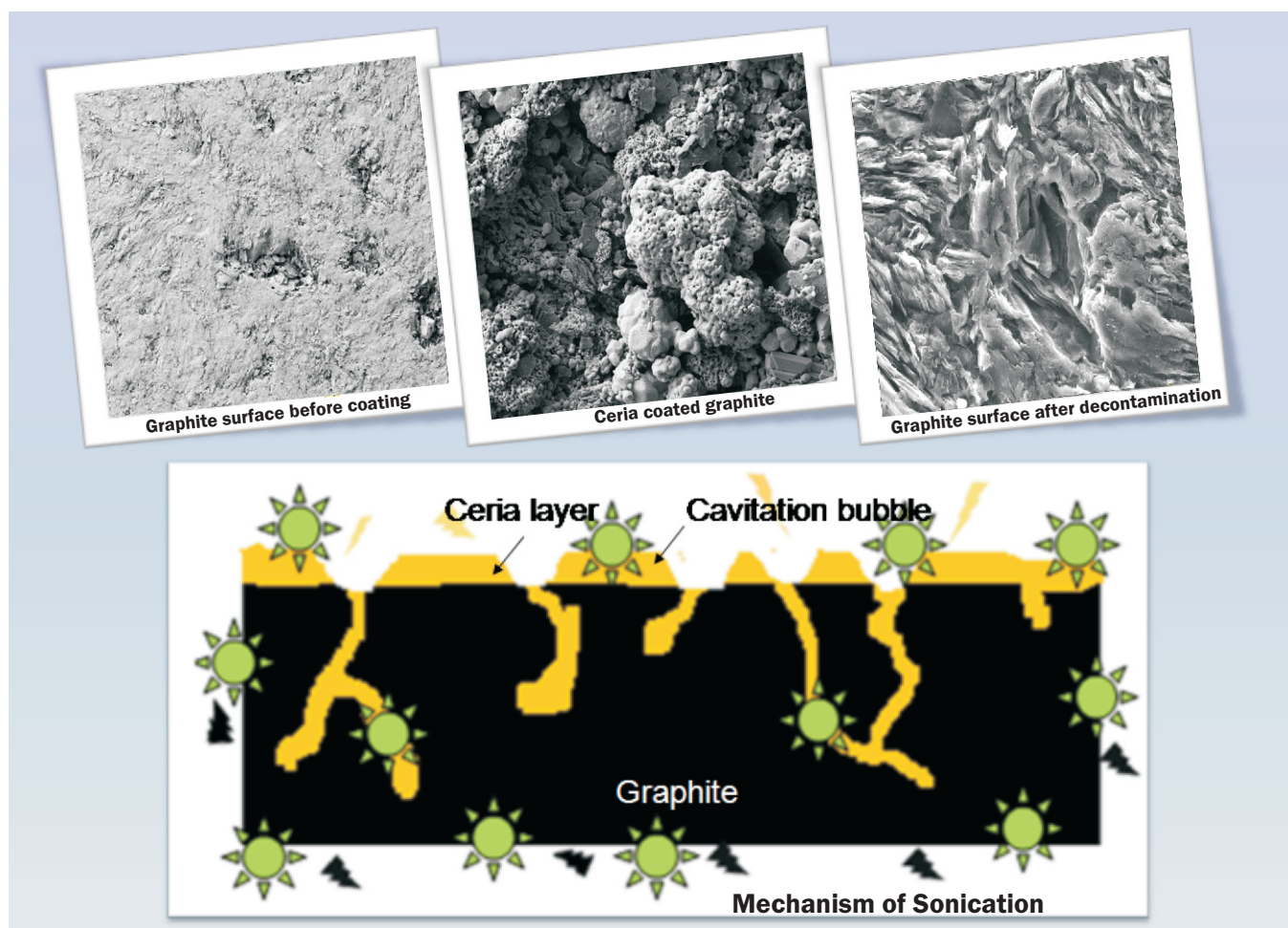Collapsed structure

After sonication

*S. Lahiri, A. Mishra, D. Mandal, R. L. Bhardwaj and P. R. Gogate

Release of adsorbed uranium from biohybrid adsorbents using ultrasound is established.

Adsorption is widely used as a wastewater remediation technique. Use of nanomaterials to remove uranium by adsorption from nuclear wastewater is widely applied. However, not much work is focused on the recovery of uranium from the sorbents. Our recent article (Lahiri *et al.*, *'Sonochemical recovery of uranium from nanosilica-based sorbent and its biohybrid'*, Ultrasonic Sonochemistry, 2021, **76**, 105667) reports the intensified recovery of adsorbed uranium from the microstructures of silica nanoparticles (SiO_2M) and its functionalized biohybrid (fBHM), synthesized with Streptococcus lactis cells and SiO_2M) using ultrasound. Effects of temperature, concentration of leachant (nitric acid), sonic intensity, operating frequency on the recovery as well as kinetics of recovery were thoroughly studied. A comparison with the silent operation demonstrated five and two fold increase due to the use of ultrasound under optimum conditions in the dissolution from SiO_2M and fBHM respectively. Results of the next cycle of adsorption studies on both the sorbents after sonochemical desorption have also been presented with an aim of reusing the adsorbent back in wastewater treatment.

*Laser & Plasma Technology Division
Beam Technology Development Group
Bhabha Atomic Research Centre
Mumbai- 400085, India

Intensified Ceria Recovery from Graphite Substrate and Cleanup of Leachant using Sonication

Graphite surface before coating

Ceria coated graphite

Graphite surface after decontamination

Ceria layer   Cavitation bubble

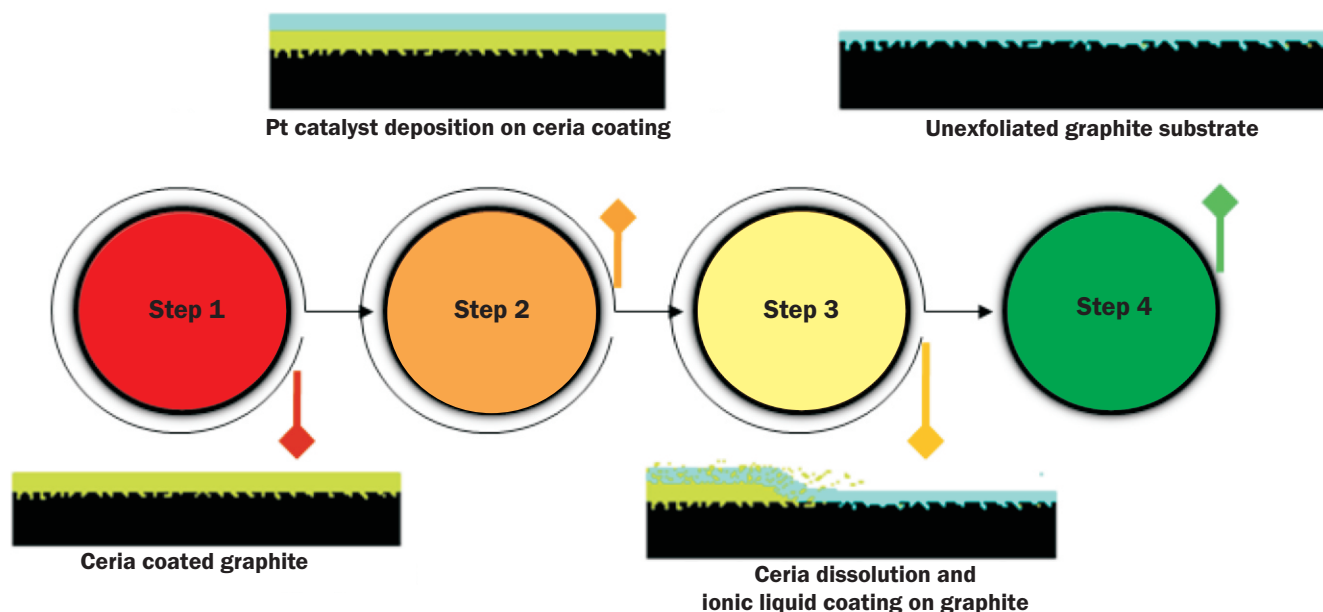Graphite

Mechanism of Sonication

*S. Lahiri, D. Mandal, P. R. Gogate and R. L. Bhardwaj

Graphite erosion and ceria recovery from pores during sonochemical decontamination has been evaluated.

There is a huge environmental concern for disposal of nuclear graphite. Our current work (Lahiri *et. al.*, *'Intensified ceria recovery from graphite substrate and cleanup of leachant using sonication'*, Chemical Engineering and Processing: Process Intensification, 2022, **174**, 108858) demonstrates sonochemical decontamination of graphite using ceria coating as the simulated contamination. The ceria recovery in the leachant solution, demonstrated to drastically reduce due to sonication, was attributed to the adsorption of cerium ions by the generated carbon residue due to exfoliation of graphite. The study of the carbon residue enabled to understand the anomaly in the observed kinetics and the role of the carbon residue in the removal of Ce^{3+} from the leach liquor. The recyclability of the graphite substrate has been studied by measuring its compressive strength and electrical conductivity. The decontamination and the recyclability of graphite demonstrated here will facilitate circular economy and serve as an important remediation technique.

*Laser & Plasma Technology Division
Beam Technology Development Group
Bhabha Atomic Research Centre
Mumbai- 400085, India

Sonocatalytic Recovery of Ceria from Graphite and Inhibition of Graphite Erosion by Ionic Liquid Based Platinum Nanocatalyst

Pt catalyst deposition on ceria coating

Unexfoliated graphite substrate

Step 1 → Step 2 → Step 3 → Step 4

Ceria coated graphite

Ceria dissolution and ionic liquid coating on graphite

*S. Lahiri, D. Mandal, S. Biswas, P. R. Gogate and R. L Bhardwaj

Inhibition of graphite erosion was intensified using ultrasound for yttria coated graphite substrates.

Use of ultrasound as an intensified non-destructive decontamination technique for processing graphite limits its reusability beyond a few number of decontamination cycles due to the exfoliation of graphite due to cavitation effects. A recent article (Lahiri *et. al.*, *'Sonocatalytic recovery of ceria from graphite and inhibition of graphite erosion by ionic liquid based platinum nanocatalyst'*, Ultrasonics Sonochemistry, 2022, **82**, 105863) established that the use of platinum nanoparticles in the leachant reduces the erosion of graphite substrate due to cavitation. It presents an improved way of sonochemical recovery of ceria using a mixture of nitric acid, formic acid and hydrazinium nitrate in the presence of platinum nanoparticles and ionic liquid. The platinum nanoparticles catalyst in ionic liquid prevented the generation of the carbon residue due to the combined effect of denitration and reduced sonication. The presence of the catalyst showed a fivefold increase in dissolution kinetics of ceria as well as absence of graphite erosion, facilitating better chances of graphite recycling than the decontamination without the catalyst. The catalytic approach offers a better recycle strategy for graphite with reduced exfoliation and NO_x generation due to denitration, making it a more sustainable decontamination process. Since ceria is used as a surrogate for plutonium oxide, the results can be extended to decontaminate such deposits clearly establishing the utility of the presented results in the nuclear industry.

*Laser & Plasma Technology Division
Beam Technology Development Group
Bhabha Atomic Research Centre
Mumbai- 400085, India

An Exceptionally Intense Turn-on Fluorescence Sensor in the Far-red Region for Common Milk Allergen β-lactoglobulin
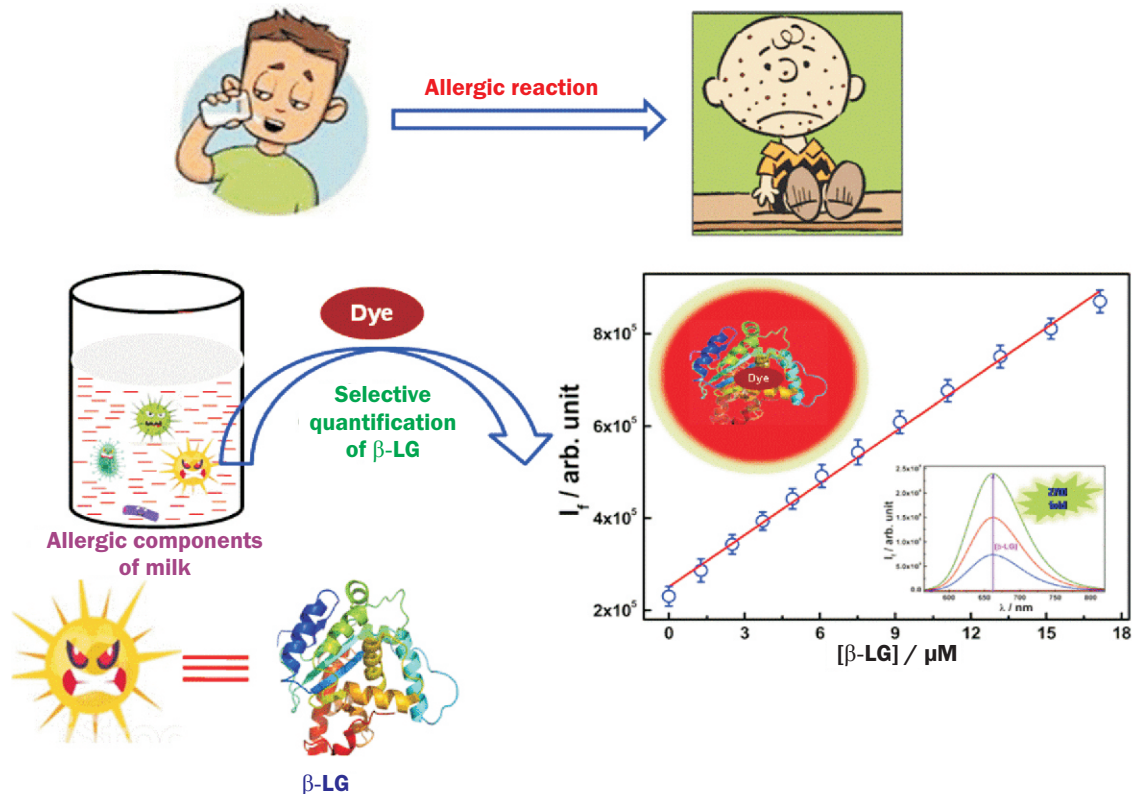

*Goutam Chakraborty, Alok K. Ray, Prabhat K. Singh and Haridas Pal

The applicability of fluorogenic probe for quantification of β-LG in real milk samples has been validated.

Common milk allergens such as, β-lactoglobulin (β-LG), pose a major health concern for public, particularly in children. Thus, sensitive and selective methods for detection of common milk allergens are highly warranted. To the best of our knowledge, detection and quantification of β-lactoglobulin, a common milk allergen, by fluorescence based technique has not been reported till date. Herein, we present the first ever fluorescence based report for the selective detection and quantification of milk allergen, β-LG, using LDS-798 as a fluorogenic probe, which registers an exceptionally large fluorescence enhancement of ~2900 fold in the far-red region upon binding with β-LG with LOD of ~6.3 (±0.3) nM for β-LG in aqueous buffer solution and 0.67 (±0.04) μM in 5% bovine milk matrix respectively (Goutam Chakraborty *et. al.*, '*An exceptionally intense turn-on fluorescence sensor in the far-red region for common milk allergen β-lactoglobulin*', Sens. Actuators, 2020,B **327**, 128864). High sensitivity and selectivity, fast response, high repeatability and reproducibility, easy operation, along with emission in the technologically advantageous far-red region make the fluorometric quantification of β-LG, using LDS-798 as a fluorogenic probe, far more advantageous than the other techniques, generally used for β-LG quantification. Importantly, we have demonstrated the applicability of this probe for quantification of β-LG in real milk samples which has been validated by an established method.

*Laser & Plasma Technology Division
Beam Technology Development Group
Bhabha Atomic Research Centre
Mumbai- 400085, India*

Development of a Phase Change Solver and its Application to Concentrated Energy Beam

Validation for copper melting

Physical phenomena of phase change under CEB
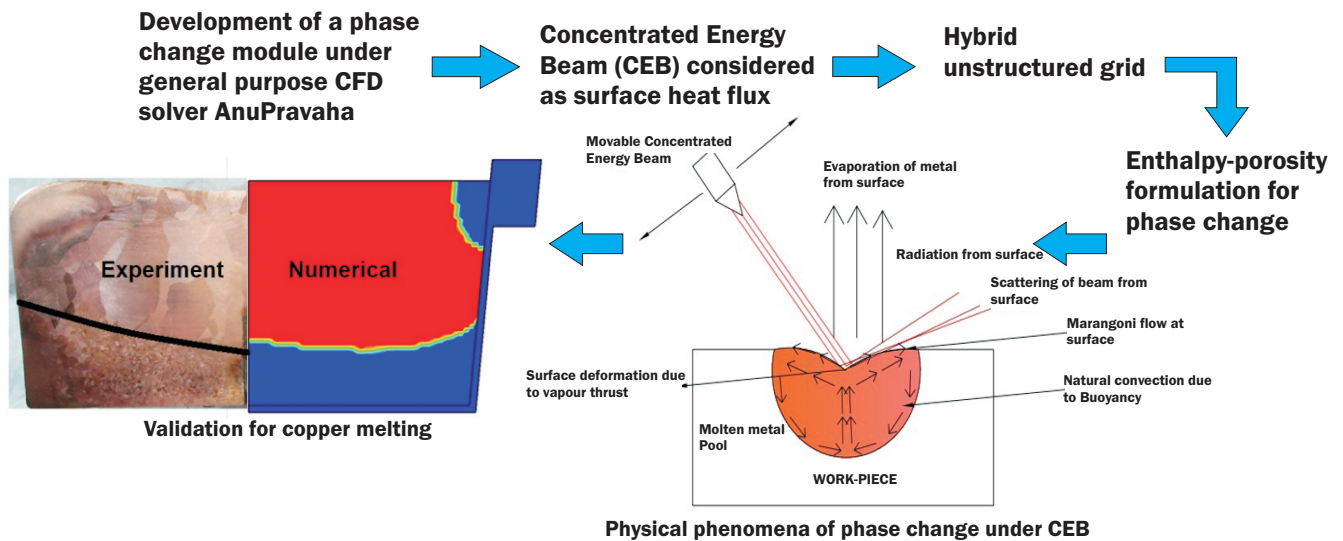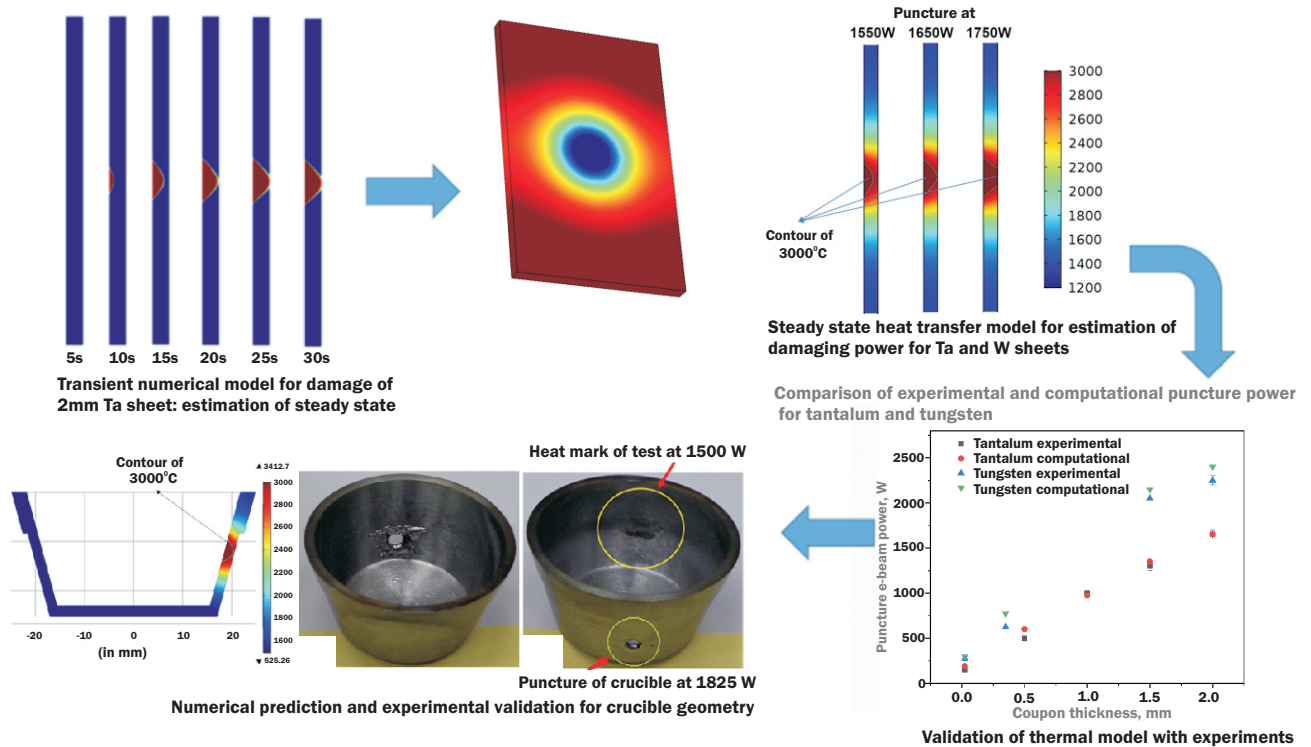
*Anik Mazumder, Tarang Garg, Amaresh Dalal and Sanjay Sethi

A phase-change computational fluid dynamics solver module was developed for the numerical solution of melting, solidification and evaporation of any substrate under a concentrated energy beam.

A phase-change computational fluid dynamics (CFD) solver module was developed for the numerical solution of melting, solidification and evaporation of any substrate under a concentrated energy beam (CEB). A fixed grid enthalpy-porosity technique was used to capture the phase change phenomena. CEB was implemented as a surface heat flux boundary conditions. Various associated phenomena like Marangoni flow and natural convection was studied for laminar flow regime. The numerical solver was validated for melting of copper and melting and evaporation of tin under a $270°$ bend pencil Electron Beam Gun (EBG) evaporator. The numerical solutions from the solver were found to be in very good agreement with experimental results with less than 5% deviation. The results were reported in a recent publication (Mazumder *et al.*, *Int. Commun. Heat Mass Transf..*, 2021, **126,** 105469). A case study was carried out using the validated solver for maximizing the molten pool fraction in the evaporator system for laser based purification processes. It was observed that for the particular geometry of the evaporator, the variation in the aspect ratio improves the molten pool fraction significantly.

*Isotopic Process Development Section
ATLA-F, Beam Technology Development Group
Bhabha Atomic Research Centre
Mumbai- 400085, India

# Evaluation of Crucible for Cold Hearth Transverse Electron Beam Vapour Generator

Transient numerical model for damage of 2mm Ta sheet: estimation of steady state

Steady state heat transfer model for estimation of damaging power for Ta and W sheets

Comparison of experimental and computational puncture power for tantalum and tungsten

Numerical prediction and experimental validation for crucible geometry

Validation of thermal model with experiments

*Dileep Kumar V., Anik Mazumder, Nagraj Alangi, Jaya Mukherjee and Sanjay Sethi

A 270° bend e-beam evaporator is generally used as a vapour generator for laser-based isotope separation process. In such an evaporator a condition is imminent where direct impingement of the beam on crucible wall happens when charge level is less than a critical level during continuous operation. Hence, electron guns are susceptible to safety issues related to direct impingement of electron beam. The objective of this study was to identify a crucible material of desired wall thickness to produce vapour of a metal which requires 1500W to achieve desired vapour for laser-based isotope separation process. The study was reported in a recently published journal paper (Kumar, D et al., Case Stud. Therm. Eng., 2021, **27**, 101318). In this study, tantalum and tungsten were investigated as candidate crucible materials experimentally. Experiments were carried out on Tantalum and Tungsten discs of different thickness to obtain the damaging power in case of direct impingement. Puncture power was numerically estimated. The simulation results are in good agreement with the experimental results.

For e-beam evaporation in laser-based isotope separation process, the wall thickness and material of the crucible for safe operation has been assessed in this study.

*Isotopic Process Development Section
ATLA-F, Beam Technology Development Group
Bhabha Atomic Research Centre
Mumbai- 400085, India

$^{98/100}$Mo Enrichment by Infrared Multi-photon Dissociation of MoF$_6$
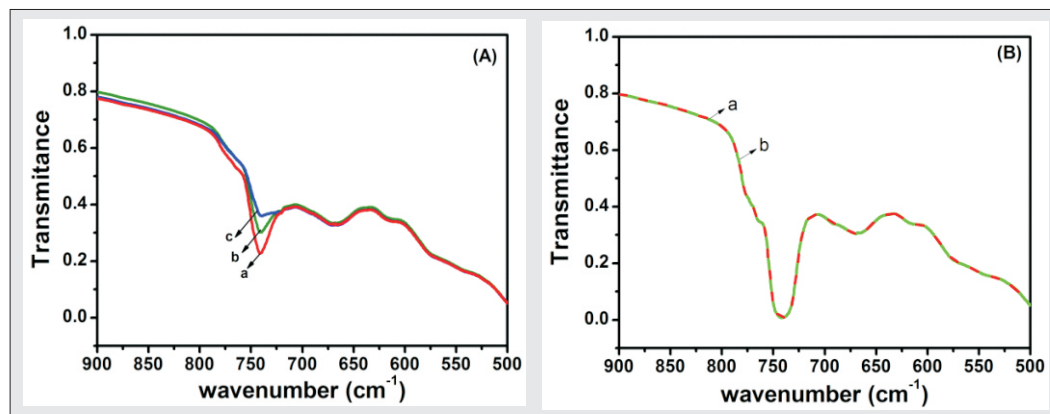
FTIR spectra depicting the absorption feature corresponding to $v3$ IR active vibrational mode of MoF$_6$. A: when the MPD cell was partially passivated. The increasing transmission with passage of time (spectra a, b, c recorded with a 15 minute gap) indicates the undesired loss of MoF$_6$. B. MPD cell satisfactorily passivated. Spectra a & b recorded with a gap of ~18 hours.

*M. B. Sai Prasad, A. Ghosh, T. Dwivedi, G. Chakraborty, R. C. Das, D. J. Biswas and J. P. Nilaya

A methodology was successfully worked out to address the handling problem of the working molecule MoF$_6$ during IRMPD experiments.

In spite of the large and ever-increasing demand for Tc[99], and, in turn, the isotopes of Mo worldwide, the literature on IRMPD of MoF$_6$ is rather scanty owing to the difficulties faced in handling this working molecule. Presence of moisture, even in slightest quantity, can result in the formation of the highly corrosive HF gas that etches away the container material, the sealants, the windows, and every other surface that it comes in contact with. Thus, although IRMPD is an established technique, the lack of research activity with MoF$_6$ is due to the paucity of knowledge in handling this gas for such experimental procedures. A methodology was successfully worked out to address the handling problem of the working molecule towards realizing enrichment of the desired isotope (M. B. Sai Prasad et al., $^{98/100}$Mo Enrichment by Infrared Multi-photon Dissociation of MoF$_6$, Chemical Physics Letters, 2022, **787**, 139262). Firstly, the experimental cell and the associated tubings, constructed of Monel and sealed with corrosion resistant gaskets (perfluoroelastomers) were evacuated to yield a leak rate better than 10^{-9} mbar-lit/sec. The trapped moisture was removed from the chamber by its repeated evacuation and baking. The surfaces were passivated by repeated exposure to fluoride environment followed by evacuation using the heat and thaw cycle approach. Care was taken to break the vacuum only in extremely pure Nitrogen atmosphere to protect this surface passivation. Our experience has shown that the acquired surface resistance to the corrosive MoF$_6$ is short lived and fragile necessitating the affirmation of gas content in the cell from time to time and repeating the passivation procedure when required. The ability of the chamber to contain MoF$_6$ was ascertained from the FTIR spectra recorded as a function of time as shown in the figure below. Experiments of IRMPD of MoF$_6$ have been carried out both at room temperature and under cooled condition (-58°C), by targeting its combination mode (v_3+v_5) utilizing a 100Hz pulsed CO$_2$ laser (Impact 300, Light Machinery make). A maximum enrichment factor of ~1.12 for the case of ^{100}Mo was achieved upon irradiation with the laser operating on 9P(10) line that is near-resonant to ^{92}MoF$_6$. Although the laser was capable of emitting ~2J/ pulse, the coupled energy into the cell was restricted to ~800 mJ due to the optical damage of the dielectric coated windows of the cell. It is a well known fact that IRMPD is an intensity driven process requiring a single isotopic species to absorb several tens of photons. Usage of uncoated optics should allow coupling of higher energy and in turn improved enrichment.

*Laser & Plasma Technology Division
Beam Technology Development Group
Bhabha Atomic Research Centre
Mumbai- 400085, India

CONNECT
SYMPOSIA
WORKSHOPS
CONFERENCES

This page is intentionally left blank

Reports from symposia, workshops and conferences

Lasers and Applications

Bhabha Atomic Research Centre and BRNS have jointly organized a 4-day national level symposium on lasers (NLS-30) during 19-22 January at Anushaktinagar, Mumbai. The symposium had 26 invited talks on diversified themes, including Physics and Technology of Lasers, Laser Spectroscopy, Ultrafast Lasers and Lasers in Nuclear Industry. More than 160 contributory papers were presented in the symposium. In addition, 15 young researchers presented their dissertation work, which was reviewed by a panel of judges drawn from various institutes of national repute. The inaugural event, which was held in hybrid mode, was attended by a host of dignitaries, which included Dr. A. K. Mohanty, Director, BARC (Guest of honour), Prof. S. Ramakrishnan, Director, TIFR (Chief Guest) amongst others. The keynote address was delivered by Prof. G. Ravindra Kumar, Distinguished Professor, TIFR.

Book of Abstracts released by the Chief Guest.

Pulsed Power Applications

Proceedings of the workshop released during the inaugural event.

A 3-day workshop on Pulsed Power Technology and Applications (WSPPTA-2021) was organized by Bhabha Atomic Research Centre during 25–27 November 2021 at its Visakhapatnam campus. Around 100 participants attended the workshop, which was held under a public outreach program, as part of Azadi ka Amrit Mahotsav activities in the Department of Atomic Energy to mark 75th year of Indian Independence. The workshop organized 15 curriculum lectures by BARC scientists, two plenary talks, five invited talks and a visit to twelve laboratories of BARC Visakhapatnam. Proceedings of the workshop was released in the form of a handbook during the inaugural event.

Trends in Vacuum Science

The Indian Vacuum Society, BARC and BRNS have jointly organized a scientific program on recent trends in Vacuum Science and Technologies (VSTAA-2022). Applications of Vacuum Science in particle accelerators, electron beam generation for thermal and non-thermal applications were covered in extensively in the program. The event was attended by 200 participants. A book of abstracts consisting of invited talks of the program was released. Book chapters based on Beam Technology development in BARC was published in 3 volumes on topics such as Laser, Electron Beams and Pulsed Power Technology was released during the inaugural session. The symposium was inaugurated by Dr. A. K. Mohanty, Director, BARC (Chief Guest) and Dr. Shashank Chaturvedi, Director, IPR (Guest of Honour). Dr. S. Krishnagopal, Head, IADD, BARC, delivered the key note address on "High Intensity Proton Accelerators in India". Speakers from globally acclaimed scientific research institutes such as CERN, ITER, ESRF, KEK, Nagasaki Univ., Singapore Univ., Pfeiffer, as well as the constituent units of DAE and non-DAE bodies have made presentations on latest developments in vacuum science and its applications.

Dr. R. B. Grover, Member Atomic Energy Commission, delivering a talk at VSTAA-2022.
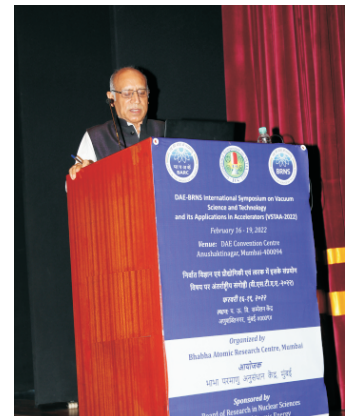
This page is intentionally left blank

LAB TO INDUSTRY
TRANSFER OF TECHNOLOGY

Update on beam technologies developed in BARC & transferred to industry for commercialization

RF Linac

The 10 MeV, 5kW RF Linac is deployed for food irradiation, medical sterilization, cross linking of polymers, semiconductor modifications, exotic coloration of gem stones and in many other research-based applications. The RF Linac technology has been transferred to a Surat-based firm for commercialization in 2021.

Senior officials of BARC and the industry partner pose for a photograph at an event for the official transfer of technology.

Electron Beam Welding

The 12kW Electron Beam Welding Machine has been deployed for Electron Beam welding of reactive, refractory and dissimilar metals in vacuum environment. It is most suitable for processing advanced materials used in aerospace and nuclear industry. Further, EB Welding is also suitable for large scale processing of materials. The technology was transferred to a Pune-based firm in 2021.

Senior officials of BARC and the industry partner pose for a photograph at an event for the official transfer of technology.

Flame Retardant Cotton Cloth

A phosphorous functionalized graphene quantum dot based solution has been synthesized in BARC that can impart fire resistance capability to cotton cloth. Upon coating the surface of the cloth with this solution, a protective polymer layer is formed, which effectively limits the ingress of oxygen thereby making it fire resistant. The technology was transferred to a Navi Mumbai-based firm in 2021.

Senior officials of BARC and the industry partner pose for a photograph at an event for the official transfer of technology.